

RALT-115

**Simultaneous Track Reconstruction And Electron  
Identification In A Gaseous Drift Chamber**

**Thesis submitted in accordance with the requirements  
of the University of Liverpool for the degree of  
Doctor in Philosophy**

**by**

**David Patrick Charles Sankey**

**January 1990**

**Oliver Lodge Laboratory  
University of Liverpool**



# Simultaneous Track Reconstruction And Electron Identification In A Gaseous Drift Chamber

David Patrick Charles Sankey

## Abstract:

The HERA accelerator currently under construction at the Deutsches Elektronen Synchrotron (DESY), Hamburg, West Germany, will produce electron-quark and electron-gluon collisions in previously unobtainable kinematic regions. The identification of leptons in the dense track environment expected in the forward tracking region will greatly enhance the understanding of the underlying physical processes. The solution to this problem adopted in the H1 detector is to install unique tracking devices in the forward region, the forward radial wire drift chambers, which simultaneously measure track momenta and  $\frac{dE}{dx}$  losses and detect transition radiation produced in polypropylene foil radiators immediately preceding the drift chambers.

This thesis describes the design, construction and testing of a series of prototype drift chambers which investigated the principles governing such devices and formed the basis for the design of the detectors to be installed in H1. The behaviour of the prototypes was investigated both with cosmic rays and also in two periods of test beam work in the electron beam Teststrahl 22 at DESY, in June/July 1987 and November 1988.

The analysis techniques evolved in order to best exploit the information made available with 100 MHz FADC digitisation of the drift chamber signals are also described. These result in a point precision of  $\sim 150 \mu\text{m}$  in the drift coordinate when using a gas mixture of Ar/C<sub>2</sub>H<sub>6</sub> 50/50 at a drift field of  $1.2 \text{ kV cm}^{-1}$  at atmospheric pressure and of 0.6% of the total wire resistance in the orthogonal coordinate along the sense wire. Analysis of data taken with a gas mixture of Xe/He/C<sub>2</sub>H<sub>6</sub> 30/30/40 at a drift field of  $1.0 \text{ kV cm}^{-1}$  at atmospheric pressure indicates that an electron pion discrimination of 90% electron acceptance with less than 10% pion contamination should be possible over the momentum range between 5 GeV and 60 GeV.



<b>Acknowledgements</b>	<b>iv</b>
<b>List of figures</b>	<b>v</b>
<b>List of tables</b>	<b>ix</b>
<b>Chapter 1: The HERA Experiment And The H1 Detector</b>	<b>1</b>
1.1 Introduction	1
1.2 The HERA Accelerator	2
1.2.1 The Standard Model	3
1.2.2 The Role Of HERA	4
1.3 The H1 Detector	10
1.4 Lepton Identification	13
1.4.1 Reasons For Requiring Good Lepton Identification	13
1.4.2 Lepton Identification In H1	17
1.5 Conclusion	20
<b>Chapter 2: The H1 Forward Track Detector</b>	<b>22</b>
2.1 Overview Of Forward Track Detector	22
2.2 Overview Of Radial Chamber	24
2.3 Radial Chamber Construction	28
2.4 Summary	34
<b>Chapter 3: Electrostatics Of The Radial Chamber</b>	<b>36</b>
3.1 Introduction	36
3.2 Electrostatics Of A Conventional Drift Cell	38
3.2.1 The Effect Of Introducing Field Wires	40
3.3 Consequences Of The Wedge Shape	44
3.4 Consequences Of The Requirement For Total Ionisation Collection	49
3.5 Conclusions	53
<b>Chapter 4: Description Of The Prototype Chambers</b>	<b>56</b>
4.1 Prototype 1: Initial Cosmic Ray Tests At Liverpool	56
4.2 Prototype 2	57
4.3 Prototype 3	63

<b>Chapter 5:</b>	<b>FADC Analysis And Hit Detection</b>	<b>66</b>
5.1	Introduction	66
5.2	FADC Systems Used In The Radial Chamber Tests.	68
5.2.1	Properties Of The Preamplifiers Used	70
5.3	Zero Suppression And Base Line Determination	71
5.4	Overflows, Re-linearisation And Cross-talk Compensation	73
5.5	Hit Finding	75
5.5.1	Chamber Efficiency	77
5.5.2	Two Track Resolution	78
<b>Chapter 6:</b>	<b>Timing Algorithms</b>	<b>82</b>
6.1	Introduction And Integer Drift Time Evaluation	82
6.2	Constant Fraction Discrimination Method	84
6.3	First Electron Method	87
6.4	Fraction Of Charge Method	89
6.5	Weighted Average Of DOS Method	92
6.6	Newton Raphson Method	94
6.7	Further Refinements	96
6.8	Track Fitting	99
6.9	Conclusions	105
<b>Chapter 7:</b>	<b>Charge Integration</b>	<b>107</b>
7.1	Introduction	107
7.2	Hub Connection	109
7.3	Preamplifier Input Resistance	111
7.4	Preamplifier De-coupling Capacitors	117
7.5	Region Of Pulse Used To Evaluate The Pulse Integral	120
7.6	Methods Used To Evaluate The Pulse Integral	126
7.6.1	Bin By Bin Summation	127
7.6.2	Trapezium Rule Integration	127
7.6.3	Simpson's Rule Integration	128
7.6.4	Pulse Shape Fitting	129
7.7	Conclusions	130

<b>Chapter 8:</b>	<b>Energy Loss Measurements And Particle Identification</b>	<b>132</b>
8.1	Introduction	132
8.2	$\frac{dE}{dx}$ Measurements	132
8.2.1	Introduction	132
8.2.2	Overview Of Energy Loss Measurements	133
8.2.3	Factors Influencing The $\frac{dE}{dx}$ Measurements	136
8.2.4	Calibration	140
8.2.5	Analysis Technique Adopted: The Truncated Mean Boot Strap	141
8.2.6	Results	144
8.3	TR Measurements	147
8.3.1	Introduction	147
8.3.2	Overview Of Transition Radiation Production	147
8.3.3	Overview Of Transition Radiation Absorption	150
8.3.4	Total Charge Method	152
8.3.6	Ordered $\frac{dE}{dx}$ Distributions	157
8.4	Conclusions	160
<b>Chapter 9:</b>	<b>Summary</b>	<b>163</b>
9.1	Introduction	163
9.2	Drift Precision Over The Entire Active Volume	164
9.3	Drift Precision Of The Chamber In A Magnetic Field	166
9.4	Drift Precision With A Xenon Based Gas	169
9.5	Conclusions And Outlook For H1	171

## **Acknowledgements:**

Firstly I would like to thank those institutions which have enabled me to pursue the research documented in this thesis:

- The Science and Engineering Research Council for financial support during the three years of my research,
- The University of Liverpool Department of Physics,
- The DESY Directorate for use of the test beam and computing facilities.

Secondly I would like to thank Dr R J Cashmore for convincing me that this was what I wanted to do and Prof. E Gabathuler and Dr J B Dainton for offering me the opportunity of doing it...

The rest of the H1 Group at Liverpool for multitudinous consultations and advice, namely Drs G A Beck, S J Maxfield, J M Morton and G D Patel.

Our collaborators at III Physikalisches Institut, RWTH Aachen, Drs H Gräßler and W Struczinski and numerous Diplomants, for their help and the gas system.

The H1 groups at Manchester and RAL, especially Dr D Clarke.

Drs D M Dainton, A Moreton, B Merry and L E Sacks for extensive help with all matters computing or otherwise.

Thanks to Dr S E Wheeler for showing that it could be done within three years, even in humanities, and finally thanks to my girl friend Kathryn R Davis for her constant support, 'encouragement' and patience in reading various drafts of this thesis.



## List of figures:

Figure 1.2.1	The HERA accelerator.	2
Figure 1.2.2	First order Feynman diagram in the standard model for electron proton scattering, showing the space-like vector boson exchange.	4
Figure 1.2.3	Standard model event rates for $e^-p \rightarrow e^- + X$ , for 30 GeV $e$ and 820 GeV $p$ , using Duke and Owens set 1 parton distributions, for $100 \text{ pb}^{-1}$ , "one year", of data.	6
Figure 1.2.4	Standard model event rates for $e^-p \rightarrow \nu + X$ , under the same conditions.	6
Figure 1.2.5	Lepton and jet momentum vectors over the same $(x, Q^2)$ range for 30 GeV $e$ and 820 GeV $p$ . At both high $x$ and low $Q^2$ jets lie close to the beam.	7
Figure 1.2.6	Feynman diagram for scalar leptoquark or leptogluon production.	9
Figure 1.3.1	The H1 detector.	11
Figure 1.4.1	Feynman diagram for boson-gluon fusion.	14
Figure 1.4.2	A 'typical' simulated event.	16
Figure 2.1.1	Layout of H1 Forward Track Detector.	22
Figure 2.2.1	Photograph depicting the mounting of the front field formers to the first production chamber.	24
Figure 2.2.2	Schematic of a Planar Supermodule element showing the three wire plane orientations.	27
Figure 2.3.1	Exploded diagram of radial chamber.	29
Figure 2.3.2	Plot of residuals versus hole number for one of the production chambers.	31
Figure 2.4.1	Material distribution of the FTD measured in terms of radiation lengths traversed by particles coming from the interaction point.	34
Figure 3.1.1	Perspective view of drift cell.	37
Figure 3.1.2	Cut through the plane A A'.	37
Figure 3.2.1	Sketch of 'ideal' drift cell.	38
Figure 3.2.2	Chamber Operating Conditions	43
Figure 3.3.1	Sketch of rectangular drift chamber.	45
Figure 3.3.2	Sketch of electrostatic potential in neighbourhood of segmented cathodes.	46
Figure 3.3.3	Field distortion due to cathodes with 6 mm strips and 2 mm gaps.	48
Figure 3.4.1	Simulation of electrostatic field in neighbourhood of front window.	50
Figure 3.4.2	Sketch of cathode plane and field former arrangement	51
Figure 3.5.1	Comparison between the $\frac{dE}{dx}$ distributions for wire 1 and wire 7.	54
Figure 4.1.1	Side view of first prototype showing cathode structure.	57
Figure 4.1.2	End view of first prototype.	57

Figure 4.2.1	Photograph of chamber with front field formers <i>in situ</i> .	60
Figure 4.2.2	Photograph of chamber with front field formers removed.	60
Figure 4.2.3	Electrical connections to the sense wires.	61
Figure 4.2.4	Electrical connections to the chamber.	62
Figure 5.1.1	A typical pulse after re-linearisation.	66
Figure 5.2.1	Schematic of chamber read-out for first prototype.	69
Figure 5.2.2	Non-linear response function.	70
Figure 5.4.1	Example of pulse that has overflowed the FADC.	73
Figure 5.4.2	Comparison between raw and re-linearised data.	74
Figure 5.4.3	Comparison between cross-talk compensated and uncompensated data.	75
Figure 5.5.1	Comparison of the DOS and weighted DOS data.	76
Figure 5.5.2	Hit distribution versus drift time.	77
Figure 5.5.3	A two track event.	78
Figure 5.5.4	Zoomed-in view of wires 5 and 6. Wire 5 is above, wire 6 is below.	79
Figure 5.5.5	Zoomed-in view of the weighted DOS for wires 5 and 6.	80
Figure 5.5.6	Zoomed-in view of the DOS data for wires 5 and 6.	80
Figure 6.1.1	Drift precision as a function of drift time for 'integer' timing, 8 bit 100 MHz FADCs and Ar/C <sub>2</sub> H <sub>6</sub> 50/50.	83
Figure 6.2.1	Illustration of CFD method.	85
Figure 6.2.2	Drift precision as a function of drift time for CFD timing with the threshold set at 10%, 8 bit 100 MHz FADCs and Ar/C <sub>2</sub> H <sub>6</sub> 50/50.	87
Figure 6.3.1	Distribution of leading edge intercept with the base line relative to the bin of maximum DOS.	88
Figure 6.3.2	Drift precision as a function of drift time for "first electron" timing, using 8 bit 100 MHz FADCs and Ar/C <sub>2</sub> H <sub>6</sub> 50/50.	89
Figure 6.4.1	Illustration of fraction of charge method.	90
Figure 6.5.1	Distribution of weighted average of DOS correction relative to the bin of maximum DOS.	93
Figure 6.5.2	Drift precision as a function of drift time for weighted average of DOS timing, using 8 bit 100 MHz FADCs and Ar/C <sub>2</sub> H <sub>6</sub> 50/50.	93
Figure 6.6.1	Drift precision as a function of drift time for Newton Raphson method, using 8 bit 100 MHz FADCs and Ar/C <sub>2</sub> H <sub>6</sub> 50/50.	95
Figure 6.7.1	Histogram of drift time residuals for 'integer' timing, using 8 bit 100 MHz FADCs and Ar/C <sub>2</sub> H <sub>6</sub> 50/50.	96
Figure 6.7.2	Distribution of leading edge intercept with the base line relative to the bin of maximum DOS.	97
Figure 6.7.3	Cumulative probability distributions for the first electron timing algorithm and the desired 'top hat' function.	98
Figure 6.7.4	Timing correction distribution after calibration for the first electron method.	99
Figure 6.8.1	Fitted drift velocity distributions.	101
Figure 6.8.2	Fitted drift time centroid versus chamber location (U/D).	102

Figure 6.8.3	Fitted $t_0$ distribution from sample of tilted tracks.	103
Figure 6.8.4	Event display of one of the tilted tracks. The track crosses the wire plane between wires 6 and 7.	104
Figure 6.8.5	Fitted drift time centroid versus position for the sample of tilted tracks.	104
Figure 6.9.1	Point precision using “first electron” timing with 6 bit FADC and 8 bit FADC data.	106
Figure 7.1.1	Example of pulse where the beam spot is at wide end of the chamber.	108
Figure 7.1.2	Example of pulse where the beam spot is near the narrow end of the chamber.	108
Figure 7.2.1	Layout of the cell inter-connection around hub. The pair of wedges 12 and 13 are connected to wedges 46 and 47. Wedges 2 and 3 are connected to wedges 16 and 17.	110
Figure 7.3.1	Diagram of the resistive wire circuit.	111
Figure 7.3.2	$\frac{dl_k}{dq}$ versus $l$ for various preamplifier input resistances.	113
Figure 7.3.3	Mean pulse shapes for the “near” pulse obtained using 200 $\Omega$ and 390 $\Omega$ preamplifiers on the first production chamber.	114
Figure 7.3.4	Mean pulse shapes for the “far” pulse obtained using 200 $\Omega$ and 390 $\Omega$ preamplifiers on the first production chamber.	115
Figure 7.3.5	Average DOS pulse shape for data taken 22.7 cm from inner radius of prototype 3.	117
Figure 7.4.1	Mean pulse shape for test pulses injected at one end of the sense wire of the first prototype, when the de-coupling capacitors were 330 pF.	118
Figure 7.4.2	Mean pulse shape for test pulses injected at one end of the sense wire of the first prototype, when the de-coupling capacitors were 10 nF.	119
Figure 7.5.1	Radial residuals for various radii.	125
Figure 7.6.1	Illustration of bin by bin summation.	127
Figure 7.6.2	Description of trapezium rule integration	128
Figure 8.2.1	Measured total charge distribution on a single wire for Xe/He/C <sub>2</sub> H <sub>6</sub> 30/40/30.	134
Figure 8.2.2	Mean $\frac{dE}{dx}$ as a function of $\beta\gamma$ for argon. The solid curve was calculated using the PAI model described in the reference, the dashed and dot-dashed curves using earlier models.	135
Figure 8.2.3	Mean $\frac{dE}{dx}$ as a function of $\beta\gamma$ for xenon.	136
Figure 8.2.4	Plot of mean truncated pulse integral versus wire number, with 200 $\mu\text{m}$ wire stagger.	137
Figure 8.2.5	Plot of mean truncated pulse integral versus wire number for data on either side of the wire plane, with 300 $\mu\text{m}$ wire stagger.	138
Figure 8.2.6	Xe/He/C <sub>2</sub> H <sub>6</sub> wire to wire gain variation.	139
Figure 8.2.7	Gain variation with pressure.	140
Figure 8.2.8	Truncated pulse integral spectrum for an individual wire and truncated mean spectrum of all wires.	143

Figure 8.2.9	Distribution of wires contributing to truncated mean.	143
Figure 8.2.10	Observed pulse spectra for the 5th and 6th largest pulses in an event for data with and without a carbon fibre radiator in front.	144
Figure 8.3.1	X-ray absorption coefficients versus photon energy for several gases.	151
Figure 8.3.2	Observed mean pulse height spectra for the front 6 wires of 3 consecutive events for data with and without a polypropylene radiator in front of the chamber. The mean pulse height spectrum for the back 6 wires without radiator is also shown.	153
Figure 8.3.3	The resultant radiating/non-radiating particle acceptance / contamination.	153
Figure 8.3.4	Total $\frac{dE}{dx}$ distributions for wires 2 and 12, no radiator, after calibration.	155
Figure 8.3.5	Radiating/non-radiating particle discrimination by threshold cut in observed pulse height spectra.	159
Figure 9.2.1	Point precision versus drift time using first electron method for all the radial positions at which data were taken with the third prototype.	165
Figure 9.2.2	Point precision versus drift time using first electron method for various radial positions at which data were taken with the second prototype. The inner radius corresponds to $X = 1000.0$ cm.	166
Figure 9.3.1	Point precision versus drift time using first electron method for data taken with the third prototype and various values of the magnetic field.	168
Figure 9.3.2	Perpendicular drift velocity versus magnetic field for data taken with the third prototype.	168
Figure 9.4.1	Point precision versus drift time using first electron method for some of the xenon data taken with the second prototype. The gas used is Xe/He/C <sub>2</sub> H <sub>6</sub> 30/30/40 except where stated.	170

## List of tables:

Table 3.3.1	Fraction of cell with distorted electric field for various strip widths.	47
Table 3.3.2	Fraction of cell with distorted electric field for various strip:gap ratios.	47
Table 6.2.1	Drift precision for various threshold levels using CFD timing, 8 bit 100 MHz FADCs and Ar/C <sub>2</sub> H <sub>6</sub> 50/50.	86
Table 6.4.1	Drift precision for various threshold levels using fraction of total charge timing, 8 bit 100 MHz FADCs and Ar/C <sub>2</sub> H <sub>6</sub> 50/50.	91
Table 7.5.1	Charge division precision for various integration ranges for data between 22.7 and 19.4 cm from the inner radius.	122
Table 7.5.2	Charge division precision for various integration ranges for data 12.1 cm from the inner radius.	122
Table 7.5.3	Charge division precision for various integration ranges for data 4.6 cm from the inner radius.	123
Table 7.5.4	Variation of charge division precision on varying the start of the integration range for data between 22.7 and 19.4 cm from the inner radius.	124
Table 7.5.5	Variation of charge division precision on varying the start of the integration range for data 12.1 cm from the inner radius.	124
Table 7.5.6	Variation of charge division precision on varying the start of the integration range for data 4.6 cm from the inner radius.	125
Table 7.6.1	Charge division precision for various integration ranges using trapezium rule integration.	128
Table 7.6.2	Charge division precision for various integration ranges using Simpson's rule integration.	129
Table 7.6.3	Charge division precision for various integration ranges fitting to summed pulse.	130
Table 7.6.3	Charge division precision for various integration ranges fitting to standard pulse.	130
Table 8.2.1	Truncated mean distributions for various data.	145
Table 8.2.2	Calculated variation in mean $\frac{dE}{dx}$ for Ar/C <sub>2</sub> H <sub>6</sub> 50/50.	146
Table 8.3.1	Results for 90% electron acceptance from comparing mean of front 6 wires over 3 events with radiator to back 6 wires without radiator.	156
Table 8.3.2	Results for 90% electron acceptance from comparing mean of front 6 wires over 3 events with radiator to front 6 wires without radiator.	157
Table 8.3.3	Results for 90% electron acceptance from comparing the second largest pulse over 3 events with radiator to the same without radiator.	160



# Chapter 1: The HERA Experiment And The H1 Detector

## 1.1 Introduction

The HERA accelerator currently under construction at the Deutsches Elektronen Synchrotron (DESY), Hamburg, West Germany, will produce electron-quark and electron-gluon collisions in previously unobtainable kinematic regions. Understanding of the underlying physical processes will be greatly enhanced by the ability to identify the resultant charged particles as well as measure their momenta. The identification of leptons in the dense track environment expected in the forward tracking region is especially desirable. The solution to this problem adopted in the H1 detector is to install unique tracking devices in the forward region, the forward radial wire drift chambers, which simultaneously measure track momenta and  $\frac{dE}{dx}$  losses and detect transition radiation.

This thesis describes the design, construction and testing of a series of prototype chambers which investigated the principles governing such devices and formed the basis for the design of the detectors to be installed in H1. The remainder of chapter 1 constitutes an overview of the physics potential at HERA and how this will be realised with the H1 detector. Chapter 2 describes the design and construction of the radial wire chambers that will be installed in H1. Chapter 3 outlines the electrostatic considerations for such a device and chapter 4 describes the prototype chambers.

The remaining chapters detail the analysis procedures adopted in interpreting the data taken in test beam and the resultant point precision and particle discrimination achieved.

## 1.2 The HERA Accelerator

The HERA accelerator is being constructed in order to investigate lepton-quark interactions at very high energy. It will provide electron proton collisions with beam energies of up to 30 GeV for the electrons and 820 GeV for the protons.

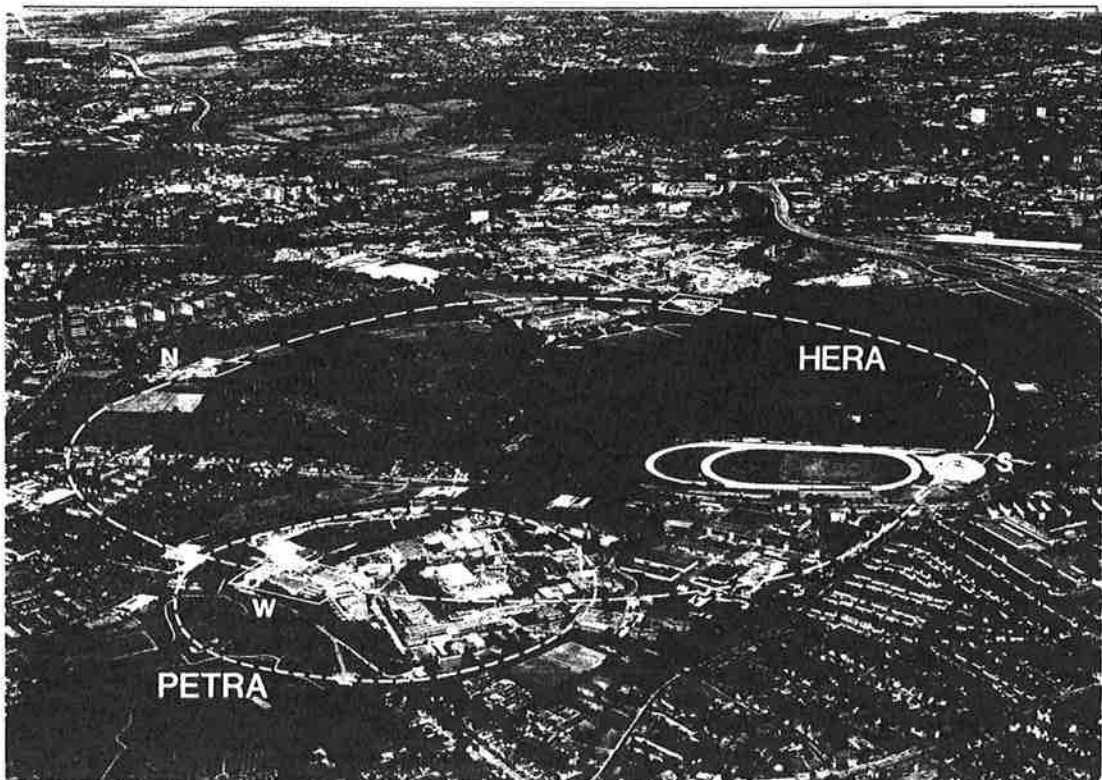


Figure 1.2.1 The HERA accelerator.

The experimental programme at HERA will include searches for new physics, comprising such exotica as massive new bosons, super-symmetric particles, lepton and quark substructure, heavy leptons and quarks associated with right-handed currents. It will permit measurement of the proton structure functions up to values of  $Q^2$  two orders of



magnitude greater than previous experiments; most importantly, both the neutral current and charged current proton structure functions will be measured in the same detectors under the same conditions.

### 1.2.1 The Standard Model

The standard picture of high energy physics provides a coherent description of the observed particles and interactions between them, up to the highest energies presently accessible<sup>1</sup>. However it only offers clues as to the underlying structure. Aside from the large number of free parameters in the model, it still leaves much unresolved<sup>2</sup>:

- Leptons:
  - Are they point-like, or do they have substructure?
  - Why are there the three families of  $e, \nu_e, \mu, \nu_\mu, \tau, \nu_\tau$ ?
- Quarks:
  - Do these have substructure?
  - Are they ever visible as free particles?
  - Are there more than the six quarks,  $u, d, c, s, t, b$ ? More immediately, does the top quark exist?
- Interactions:
  - Is the chiral structure of the electro-weak interaction as predicted by the standard model?
  - How are the masses of the weak vector bosons, the  $W^\pm$  and the  $Z^0$ , generated?
  - Does QCD form the basis of the strong interactions?
  - Are there any lepton-quark interactions which change leptons into quarks, as predicted in most grand unified theories?

## 1.2.2 The Role Of HERA

HERA will provide polarised  $e^\pm$  beams and a massively increased energy range compared to previous lepton-hadron scattering experiments. For the maximum 30 GeV electrons and 820 GeV protons the centre of mass energy will be 314 GeV. Not only will events be seen with  $Q^2 > 30000 \text{ GeV}^2$ , but the Bjorken- $x$  range down to  $x = 10^{-4}$  will also be accessible; this will enable measurement of the “soft” parton distributions, dominated by the contribution from gluons. With the Standard Model cross-sections, the expected neutral current event rates, as a function of  $x$  and  $Q^2$ , are shown in figure 1.2.3 and the charged current event rates in figure 1.2.4. The distribution of the momentum vectors over the same  $(x, Q^2)$  range is shown in figure 1.2.5. The basic first order diagram involved is shown in figure 1.2.2.

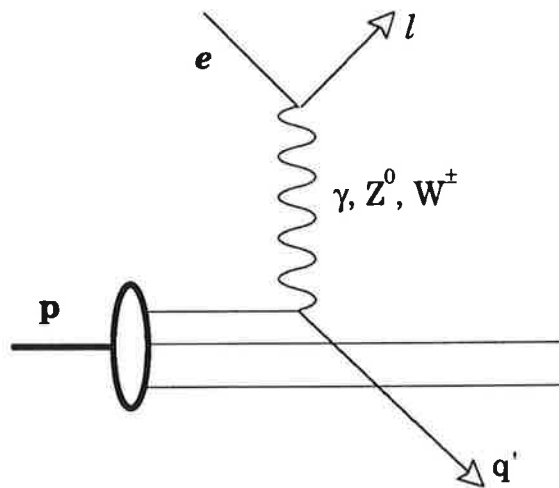


Figure 1.2.2 First order Feynman diagram in the standard model for electron proton scattering, showing the space-like vector boson exchange.

The neutral current total cross-section is given by:

$$\frac{d^2\sigma}{dx dy} = \frac{4\pi\alpha^2 s}{Q^4} \left[ 2x \frac{y^2}{2} F_1^{e p}(x, Q^2) + F_2^{e p}(x, Q^2)(1-y) + x F_3^{e p}(x, Q^2)y \left(1 - \frac{y}{2}\right) \right] \quad [1.2.1]$$

where the  $Z^0$  propagator and electro-weak mixing are implicitly included in the  $F_i^{e p}$ . The charged current total cross-section is given by:

$$\frac{d^2\sigma}{dx dy} = \frac{\pi\alpha^2}{4 \sin^4 \theta_W} \frac{s}{(Q^2 + M_W^2)^2} \left[ 2x \frac{y^2}{2} F_1^{v p}(x, Q^2) + F_2^{v p}(x, Q^2)(1-y) + x F_3^{v p}(x, Q^2)y \left(1 - \frac{y}{2}\right) \right] \quad [1.2.2]$$

where  $s$  is the square of the centre of mass energy,  $F_i^{l p}$  are the relevant proton structure functions,  $\theta_W$  is the Weinberg mixing angle,  $M_W$  is the mass of the  $W$  boson,  $Q^2$  is the square of the 4-momentum transferred and  $\nu$  is the energy transferred in the proton rest frame;

$$\begin{aligned} s &= 4E_e E_p \\ Q^2 &= 4E_e E_l \sin^2 \frac{\theta}{2} \\ \nu &= \frac{2E_p (E_e - E_l \cos^2 \frac{\theta}{2})}{M} \\ x &= \frac{Q^2}{2M\nu} \\ y &= \frac{M\nu}{2E_e E_p} \end{aligned}$$

In the above  $E_e$  and  $E_p$  are the electron and proton beam energies,  $M$  is the proton mass and  $E_l$  is the energy of the scattered lepton, with  $\theta$  as the scattering angle in the lab.  $x$  is to good approximation (negligible parton transverse momentum,  $p_T$ , within the target proton) the fraction of the proton momentum carried by the ‘‘struck’’ parton. The importance of the forward region is immediately apparent from comparison of the momentum vector and event rate distributions.

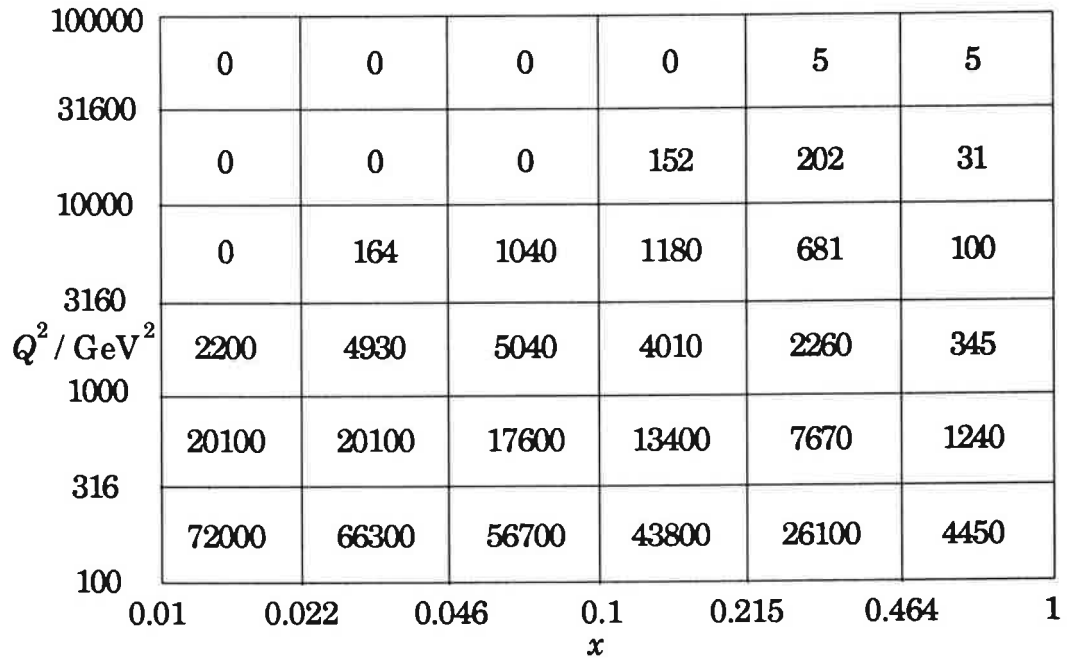


Figure 1.2.3 Standard model event rates for  $e^-p \rightarrow e^- + X$ , for 30 GeV  $e$  and 820 GeV  $p$ , using Duke and Owens set 1 parton distributions<sup>3</sup>, for  $100 \text{ pb}^{-1}$ , “one year”, of data.

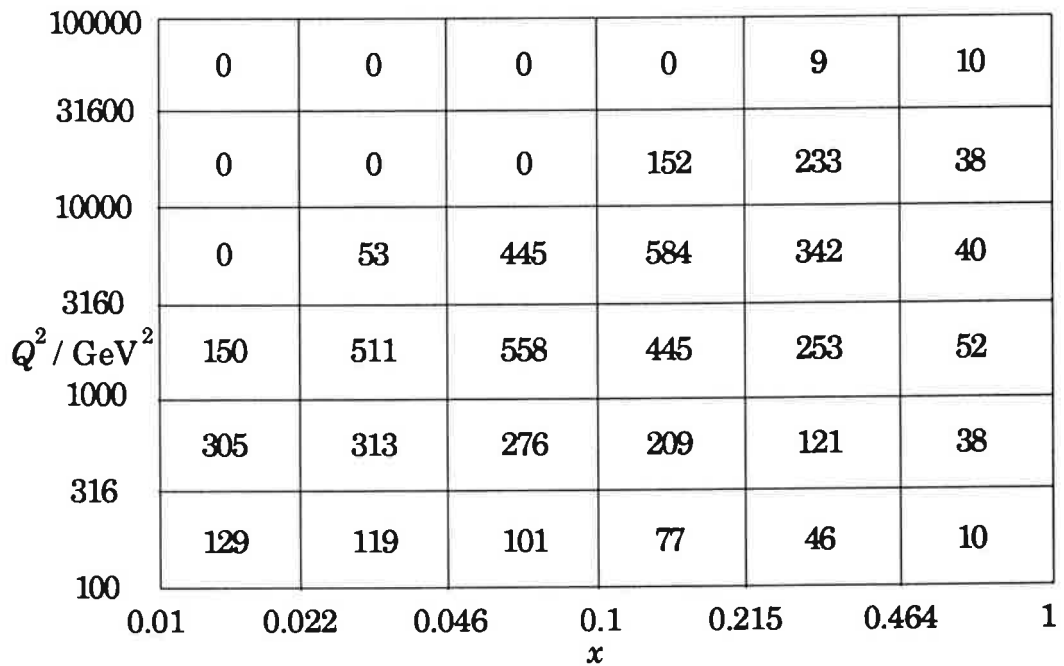


Figure 1.2.4 Standard model event rates for  $e^-p \rightarrow \nu + X$ , under the same conditions.

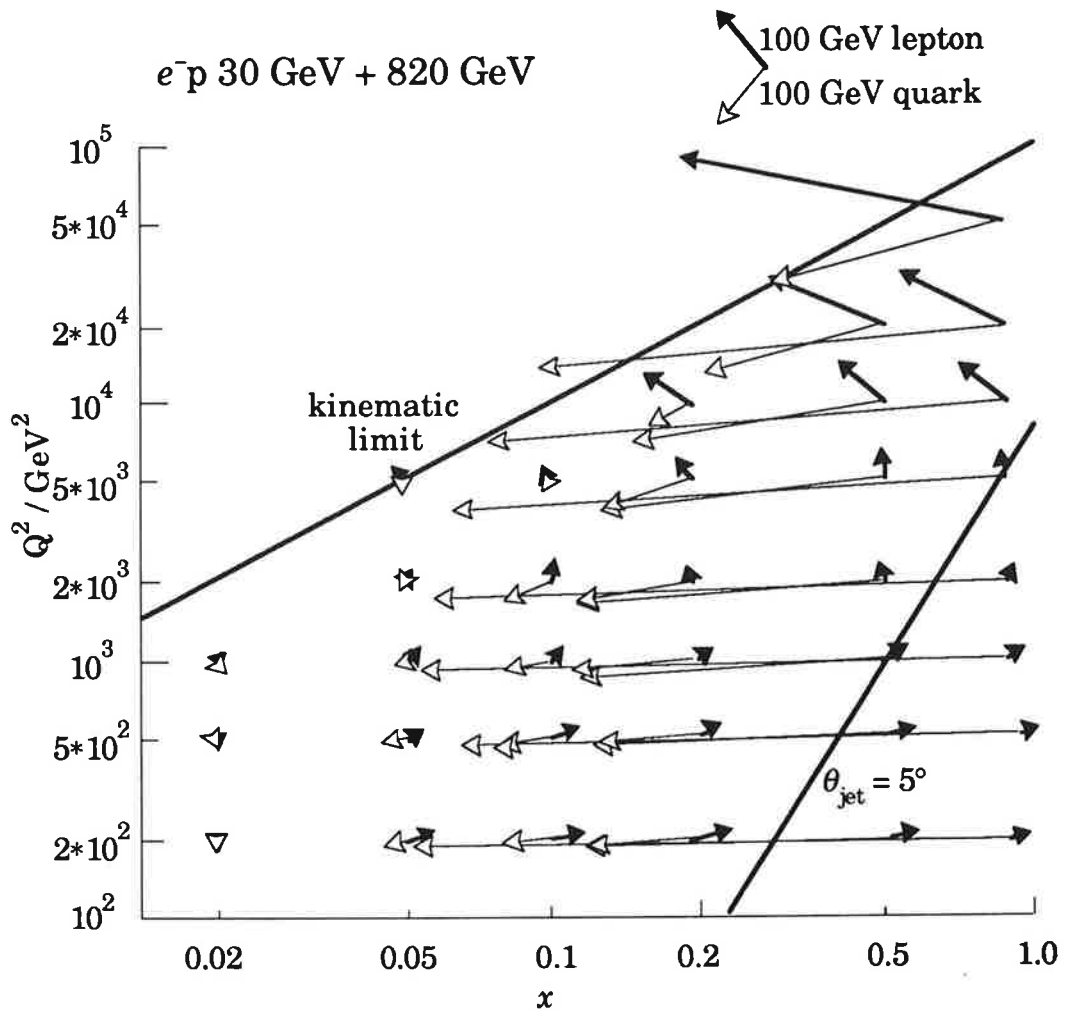


Figure 1.2.5 Lepton and jet momentum vectors over the same  $(x, Q^2)$  range for 30 GeV  $e$  and 820 GeV  $p$ . At both high  $x$  and low  $Q^2$  jets lie close to the beam.

HERA will extend the search for lepton substructure, as revealed by excited lepton states, to a distance scale an order of magnitude smaller than previously possible, namely to around  $3 \times 10^{-20}$  m. The  $e^+e^-$  machine LEP at CERN will eventually reach a similar energy scale, but in annihilation processes (time-like) rather than scattering experiments (space-like), thus providing complementary information. Annihilation experiments analyse the vacuum and the virtual particles therein, whereas scattering experiments analyse the contents of the projectile and the target. HERA will also provide unique opportunities for looking

for leptons coupled to the electron, with masses up to 150 GeV, whose signatures might be masked by competing processes in  $e^+e^-$  annihilation<sup>4</sup>.

The measurement of the proton structure functions will be particularly important; the high  $Q^2$  available at HERA means that the effect of final state parton interactions such as mass terms and non-perturbative or “higher twist” effects, which are in general proportional to  $\frac{1}{Q^2}$ , should be much reduced compared to previous experiments<sup>5</sup>. Although determination of the normalisation of the structure functions will not be easy, a clean separation of the  $Q^2$  evolution should be possible. As an example, in the very low  $x$  region, the lower  $Q^2$  means that the  $Z^0$  contribution to the neutral current cross-section will be small, enabling accurate measurement of  $F_2^{em}$ , the proton structure function most readily related to its quark constituents:

$$F_2^{em}(x, Q^2) = \sum_{f=u,d,s,c} e_f^2 [x Q_f(x, Q^2) + x \bar{Q}_f(x, Q^2)] \quad [1.2.3]$$

where  $e_f$  is the quark charge, and  $Q_f(x, Q^2)$  is the quark momentum distribution. This will enable more quantitative tests of QCD, allowing comparison with existing lower energy data to observe directly the QCD evolution<sup>6</sup>. Finally, come the advent of the next generation of accelerators, the structure functions measured will provide an important basis for understanding the physics at the new energy scale of the pp and  $p\bar{p}$  colliders.

Looking beyond the Standard Model, the availability of polarised beams will permit searches for right-handed weak currents, testing the predicted helicity structure of the standard model. One method of accommodating the observed left-right asymmetry in the Standard Model is to

assume it to have a “spontaneously broken” symmetry, with the right-handed currents mediated by heavier vector bosons than the left-handed  $W^\pm$  and  $Z^0$ .

HERA is the ideal tool for searching for new lepton-quark interactions. In particular  $s$ -channel exotica such as leptoquark production (figure 1.2.6) should be readily observable, if they exist with a low enough mass. These are predicted not only in SU(5) and technicolour unified theories, but also in superstring based theories<sup>7</sup>.

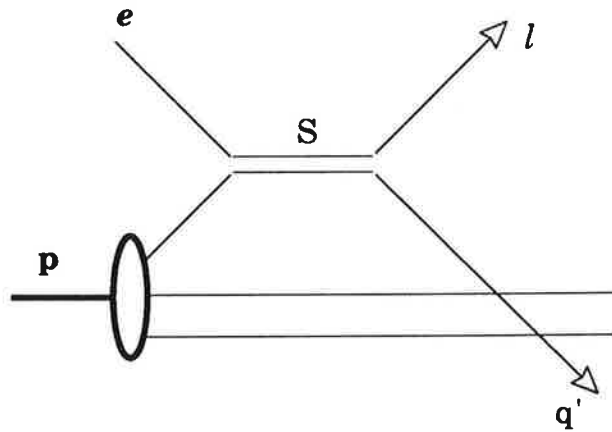


Figure 1.2.6 Feynman diagram for scalar leptoquark or leptogluon production.

The main background to leptoquark detection at HERA will be NC and CC deep inelastic scattering (DIS). The decay of scalar leptoquarks will have a flat  $y$  dependence, as they have zero spin, compared to  $\frac{1}{y^2}$  for DIS, thereby making a very clean separation possible<sup>8</sup> and enabling detection almost up to the HERA kinematic limit.

## 1.3 The H1 Detector

To exploit the potential offered by HERA, any detector has to meet the following general requirements<sup>9</sup>:

- It must have a high degree of hermeticity in order to investigate phenomena involving energetic neutrinos or other non-interacting secondary particles.
- It must permit excellent measurements of energy flow for the inclusive measurements of neutral current (NC) and charged current (CC) interactions, based on good energy resolution, fine granularity and absolute energy calibration for both electromagnetic (EM) and hadronic contributions.
- It must have efficient muon identification and accurate energy measurement. These are essential for the new physics searches, and also for heavy flavour physics.
- It must have optimum electron identification and energy resolution, as electrons will play a key role in HERA physics.

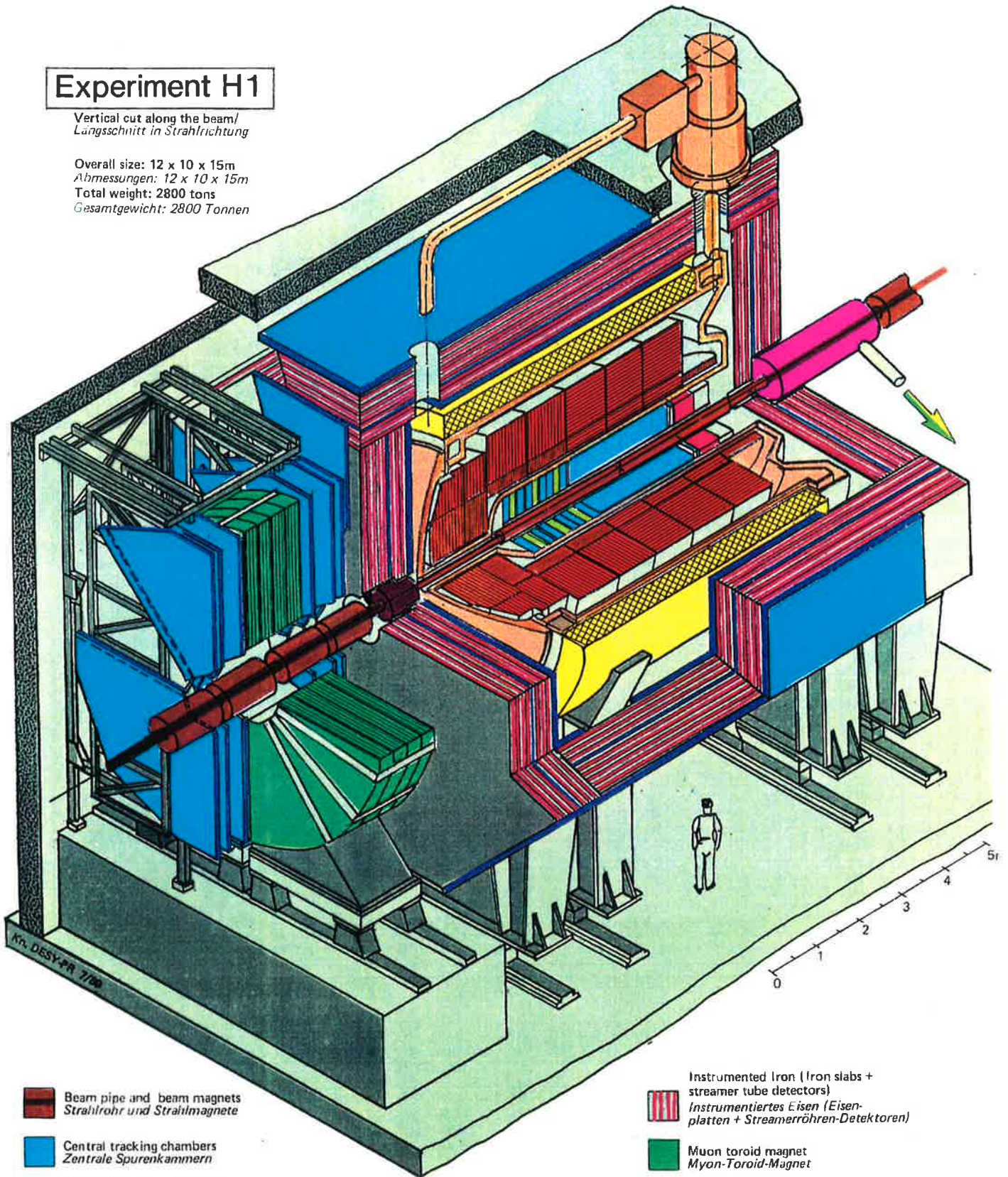
The event topology of HERA collisions necessarily leads to an asymmetric detector design; the centre of mass of the collision moves fast along the proton direction, and the quark fragments and especially the decay products of any heavy particles produced in the collision are boosted along this direction. For example, about 50% of all leptons and of the hadron fragments due to the decay of new heavy particles are typically emitted into polar angles less than  $25^\circ$ . The H1 detector reflects this asymmetry and is designed to provide a smooth and homogeneous response from small forward angles through to backward angles.





# Experiment H1


Vertical cut along the beam/  
Längsschnitt in Strahlrichtung

Overall size: 12 x 10 x 15m  
Abmessungen: 12 x 10 x 15m  
Total weight: 2800 tons  
Gesamtgewicht: 2800 Tonnen



 Beam pipe and beam magnets  
Strahlrohr und Strahlmagnete

 Central tracking chambers  
Zentrale Spurenkammern

 Forward tracking chambers  
and transition radiators  
Vorwärtsspurenkammern und  
Übergangsstrahlungsmodul

 Electromagnetic Calorimeter (lead)  
Elektromagnetisches Kalorimeter (Blei)

 Hadronic Calorimeter (stainless steel)  
Hadronisches Kalorimeter (Edelstahl)


 Superconducting coil (1.2 Tesla)  
Supraleitende Spule (1,2 Tesla)

Liquid Argon:  
Flüssiges Argon:

 Compensating magnet  
Kompensationsmagnet

 Helium cryogenics  
Helium Kälteanlage

 Muon chambers  
Myon-Kammern

 Instrumented Iron (Iron slabs +  
streamer tube detectors)  
Instrumentiertes Eisen (Eisen-  
platten + Streamerröhren-Detektoren)

 Muon toroid magnet  
Myon-Toroid-Magnet

 Warm electromagnetic calorimeter  
Warmes elektromagnetisches  
Kalorimeter

 Plug calorimeter (Cu,Si)  
Vorwärts-Kalorimeter

 Concrete shielding  
Betonabschirmung

 Liquid Argon cryostat  
Flüssig Argon Kryostat

The detector layout is illustrated in figure 1.3.1. It consists of:

- Central and forward tracking provided by a central jet chamber (CJC), interleaved with two z-chambers and multi-wire proportional chambers (MWPCs), and the forward track detector (FTD) consisting of three layers of radial and planar geometry drift chambers with MWPCs and transition radiators. The FTD is described in greater detail in the following chapter.
- The EM calorimeter, with lead plates as the showering material and liquid argon (lAr) as the detector medium in the forward and barrel region, and a lead scintillator “sandwich” in the backward region.
- The hadronic calorimeter using lAr with stainless steel absorber plates. Here an optimised weighting procedure is used to improve the energy resolution, compensating for the differing EM and hadronic responses by taking advantage of the fine granularity<sup>10</sup>. Basing the calorimetry on lAr results in a stable and readily calibrated detector. The use of one cryostat moreover avoids inhomogeneities and dead material in the region between the forward and barrel calorimeters, where the energy resolution and calibration are of prime importance.
- A superconducting solenoid and its cryostat outside the hadronic calorimeter. This provides a large homogeneous magnetic field in the region of the central and forward tracking detectors; the design tracker momentum resolution is  $\sigma(p)/p^2 < 0.003 \text{ GeV}^{-1}$  for isolated tracks in the angular range  $7^\circ \leq \theta \leq 150^\circ$ . The large coil also minimises the dead material in front of the EM calorimeter.

- An outer shell of iron plates to contain the return magnetic flux. This is interleaved with plastic streamer tubes, in order to act as a “tail-catcher” for the hadronic calorimeter and as a muon filter and tracker.
- Additional muon detection, provided by three layers of muon chambers in the barrel and forward region, along with a forward muon spectrometer, which consists of a magnetised iron toroid and four layers of drift chambers.
- A plug calorimeter to detect hadronic energy at small angles, ( $\theta \geq 0.7^\circ$ ), built as a copper silicon sandwich.
- A magnet which compensates for the axial magnetic field of the large solenoid.

## 1.4 Lepton Identification

### 1.4.1 Reasons For Requiring Good Lepton Identification

Charged lepton production is expected to provide an important signature for new heavy particles. Although one might expect heavy quarks to be produced via leading order diagrams such as figure 1.2.2, it turns out that the next-to-leading-order boson-gluon fusion (figure 1.4.1) dominates, the former being heavily suppressed by the very low mixing between heavy and light quark eigenstates.

For instance, when undertaking a search for the top quark, it is possible to tag the electron or muon from the semileptonic decay of the top quark as an isolated, unbalanced high  $p_T$  lepton. In comparison the light quark and charm decays result in a less well isolated lepton, and NC DIS in a lepton more balanced in  $p_T$ , leaving the remaining background

dominated by production of  $b\bar{b}$  pairs<sup>11</sup>. Similarly, a cut on the transverse momentum, together with isolation from the accompanying hadronic energy, of the ‘hardest’ unmatched lepton candidate should provide good separation of charm and bottom events produced by boson-gluon fusion at low  $x$  and  $Q^2$ . In this kinematic region the scattered lepton will tend to be lost in the beam pipe<sup>12</sup> as indicated in figure 1.2.5.

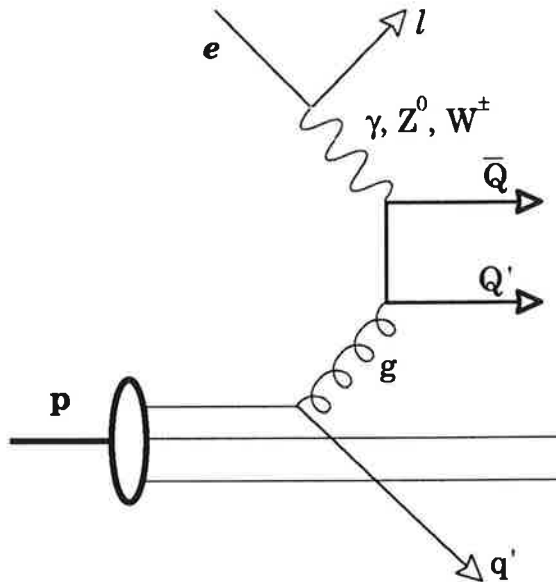


Figure 1.4.1 Feynman diagram for boson-gluon fusion.

Less exotic physics will also require effective lepton identification. For example, most of the CC and NC DIS processes can be isolated by comparing the kinematic variables deduced from the highest  $p_T$  particle (i.e. assumed to be an electron) with the ones obtained for the rest of the particles of the event<sup>13</sup>. Alternatively, a separation to a level of fractions of percent can be achieved by using loose cuts on the measured minimum opening angle between the candidate scattered electron and any charged particle, if the “scattered electron” is tagged as being the most isolated object among the four highest  $p_T$  particles in the event. This requires the detection of the charged tracks by the forward or central tracking de-

tectors, along with global transverse momentum and energy flow measurements.

When studying the gluon structure function, boson-gluon fusion events through the muon channel of the heavy flavour's semileptonic decays can be selected with relatively large background reduction, by a simple momentum cut on the muon candidate.

For most of the above processes, the forward region plays an essential role, and the high track densities and high momenta present by far the most stringent requirements on lepton identification. Some idea of the event complexity in the forward region may be surmised from figure 1.4.2.

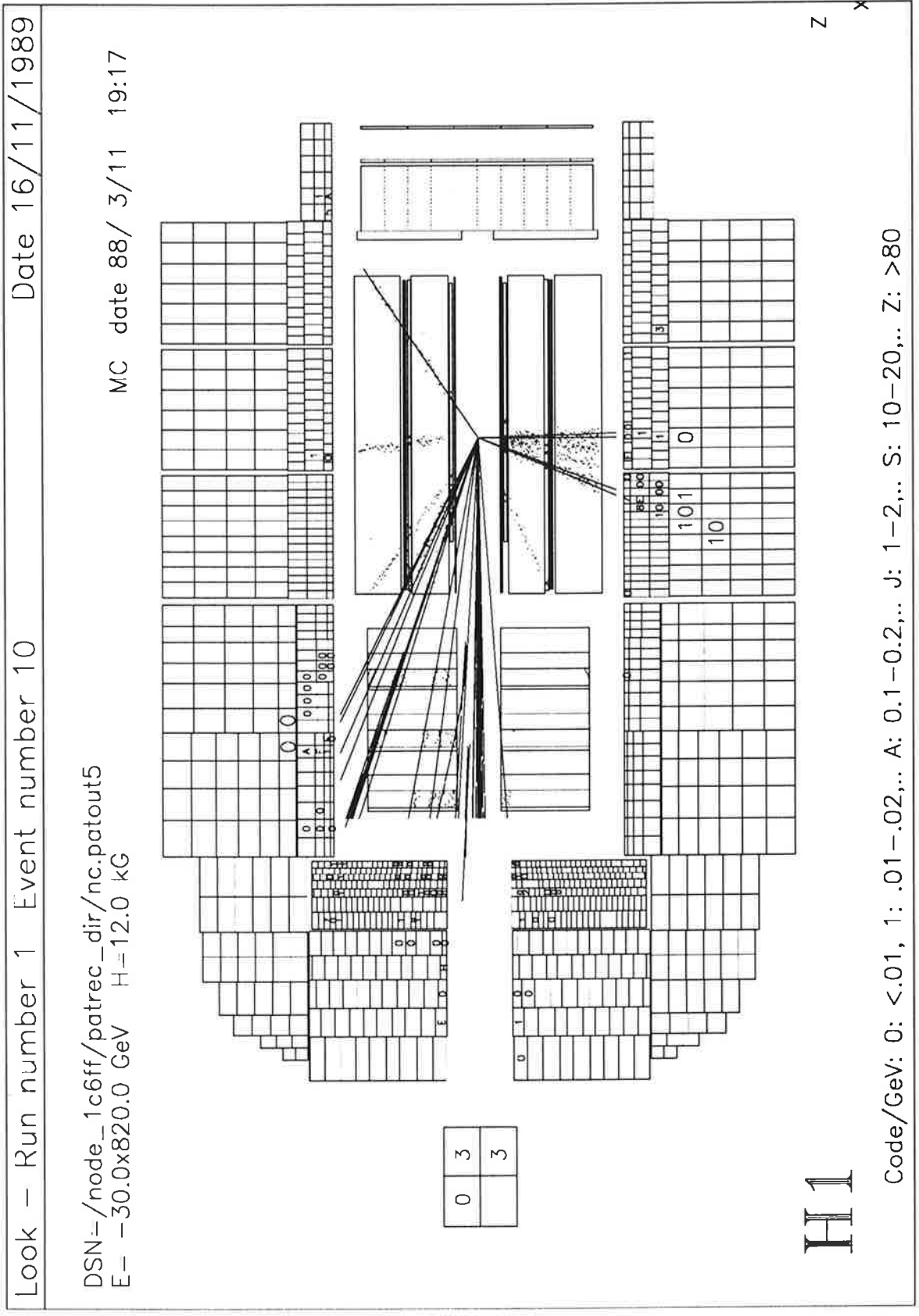


Figure 1.4.2 A 'typical' simulated event.

## 1.4.2 Lepton Identification In H1

An electron detection efficiency of 95% should be achieved with a pion rejection ranging from better than 1:10<sup>2</sup> at 10 GeV to better than 1:10<sup>3</sup> at 100 GeV, solely on the basis of calorimetry<sup>14</sup>. A substantial fraction of this rejection is obtained from the global characteristics which best distinguish electromagnetic and hadronic showers; in contrast with hadronic showers, electromagnetic showers have an early start followed by an energetically dense and compact shower maximum leading to fast exhaustion, with containment in the electromagnetic section typically above 95%. The ratio between the radiation length ( $X_0$ ) and nuclear interaction length ( $\lambda_I$ ) of the Pb/Ar stacks is  $1 X_0 = 0.043 \times \lambda_I$ . The measurement of the lateral 'compactness' at the expected electromagnetic shower maxima additionally improves the rejection by up to a factor 5. Finally, exploitation of the full EM section granularity allows the first and second moment of the longitudinal and lateral distributions to be evaluated and then compared with the expected average shape and fluctuations of the full shower profile.

The main physics limitation to the rejection of charged hadrons originates from charge-exchange reactions (e.g.  $\pi^- p \rightarrow \pi^0 n$ ) occurring in the first electromagnetic layer (about 10% of the hadrons) in which most of the energy is carried away by the  $\pi^0$ . This represents from 1% of the inelastic cross section at a few GeV to 0.2% at 10 GeV and below 0.02% at 100 GeV. Ordinary inelastic interactions can also lead to large fractional energy transfer to  $\pi^0$ s, and the identification will then mainly rely on the detection of the 'late' smaller hadronic components. False  $e^\pm$  signal due to  $\pi^\pm \gamma$  overlap can be dealt with by combining information from the calorimeter and tracking detectors.

Using the CJC, separation between  $e$  and  $\pi$ ,  $p$  and  $K$  can be derived from the measurement of the  $\frac{dE}{dx}$  ionisation losses. This ionisation loss is a function of the  $\beta\gamma$  ratio ( $p/m$ ) of the particle, where  $p$  is the measured momentum,  $m$  the hypothesized mass and  $\beta$  the velocity. In practice, the  $\frac{dE}{dx}$  sampling of an individual wire is parametrised by a Landau distribution. The long tail in the distribution is essentially insensitive to the particle velocity, so the relevant information comes mainly from the most probable value. Hence the lowest 70%, for example, of the measured contributions to the total  $\frac{dE}{dx}$  can be used to build a simple estimator which is nearly Gaussian (by central limit). Such an estimator can provide  $e/\pi$  separation of up to  $3\sigma$  from  $20^\circ$  to  $160^\circ$  in  $\theta$ . The separation is degraded above  $143^\circ$  and below  $37^\circ$  by the track exiting the end wall of the CJC, thereby reducing the number of wires contributing to the measurement. Alternatively, it is possible to employ a maximum likelihood technique, either by computing the ratio of the product likelihood for any two particles to give a particular set of (truncated)  $\frac{dE}{dx}$  measurements, or, assuming a simple scaling of the  $\frac{dE}{dx}$  distributions, by maximising the likelihood for a given particle relative to the scaling parameter<sup>15</sup>.

In the forward tracker, the  $e/\pi$  discrimination is based on the signals measured in the three radial chambers and the planar chambers. The radial chambers detect the primary particle's  $\frac{dE}{dx}$  along with the transition radiation (TR) emitted in passing through the stacks of TR foils. The TR photon rate on crossing between media with different dielectric constants is proportional to the particle's Lorentz factor  $\gamma$  and is at very small angles to the particle track  $\left(\langle\theta\rangle \approx \frac{1}{\gamma}\right)$ . The TR foils are made of polypropylene for good X-ray transparency; this means that the X-rays are absorbed mainly in the drift chamber gas, which is a xenon based mixture. The planar chambers provide additional measurements of the



primary particle's  $\frac{dE}{dx}$ . A combined TR and  $\frac{dE}{dx}$  estimator may be constructed by using a truncated mean of the largest pulses from the radials (maximum sensitivity to TR), along with truncated means of the signals from both the radials and planars (maximum sensitivity to  $\frac{dE}{dx}$  loss). Tracks which pass through the whole forward tracker ( $7^\circ \leq \theta < 17^\circ$ ) provide up to 72  $\frac{dE}{dx}$  measurements.

Combining information from the tracking detectors and the calorimeter enables further refinement of the  $e/\pi$  separation. The measured momentum can be used to predict the mean shower characteristics of the candidate electrons. An estimator based on the comparison of the energy measured in the calorimeter with the tracker's momentum measurement provides enhanced hadronic rejection (typically by up to an order of magnitude), and in particular rejection of overlap contamination. Further rejection of the  $\pi^\pm \gamma$  contamination (where the  $\pi^\pm$  decays to  $\mu^\pm \nu$  with the  $\mu$  being emitted within the multiple scattering cone, or the  $\pi^\pm$  punches through the calorimeter) will be provided by the matching of the extrapolated charged track with calorimeter based impact point reconstruction.

The track measured in the iron streamer tube system ( $25^\circ < \theta < 130^\circ$ ), or in the forward toroidal muon spectrometer ( $3^\circ < \theta < 17^\circ$ ) for a pattern recognised "muon" can be matched to extrapolated tracks from the inner detectors for muon identification. Beside impact point matching, the muon streamer chamber system also offers independent momentum measurement with a resolution varying from 35% at 5 GeV to about 75% at 15 GeV. This measurement can be combined with the momentum measurement in the inner detector to further reduce the number of eventual falsely tagged high momentum "muons".

## 1.5 Conclusion

The HERA accelerator will produce electron-quark and electron-gluon collisions in previously unobtainable kinematic regions. As outlined above the H1 experiment will be well equipped to exploit both the foreseen physics and the unexpected. The high centre of mass energies and asymmetric beam configuration lead to a strong flux of particles into the forward cone. The radial wire drift chambers will form the mainstay of the forward track detector in a region which is expected to be densely populated with tracks. They will measure the track momenta, ionisation losses and detect any transition radiation present for incident charged particles, using the transition radiation detection to enhance the particle discrimination.

- 
- <sup>1</sup> S L Glashow, Nucl. Phys 22 (1961) 579,  
S Weinberg, Phys.Rev.Lett. 19 (1967) 1267,  
A Salam, Proc. 8th Nobel Symposium, *ed.* N Svartholm, 1968, p367
  - <sup>2</sup> Study on the proton-electron storage ring project HERA, ECFA 80/42,  
DESY HERA 80/01, 1980
  - <sup>3</sup> D W Duke and J F Owens, Phys Rev D30 (1984) 49
  - <sup>4</sup> R J Cashmore *et al*, Phys Rep 122 (1985) 275
  - <sup>5</sup> Study on the proton-electron storage ring project HERA, ECFA 80/42,  
DESY HERA 80/01, 1980
  - <sup>6</sup> G Ingelman and R Rückl, Quark momentum distributions from *ep* collisions:  
strategies and prospects, DESY 89-025

- 
- 7 J Bijnens, Proceedings of the HERA workshop, *ed.* R D Peccei, 1987, p 819, and R J Cashmore *et al*, Phys Rep 122 (1985) 275
  - 8 N Harnew, Proceedings of the HERA workshop, *ed.* R D Peccei, 1987, p 829
  - 9 Technical proposal for the H1 detector, DESY, 1986
  - 10 W Braunscheig *et al*, Results from a test of a Pb-Fe liquid argon calorimeter, DESY 89-022, submitted to NIM
  - 11 G Ingelman *et al*, Top search strategies for HERA, DESY 88-143
  - 12 A Ali *et al*, Heavy quark physics at HERA, DESY 88-119
  - 13 G Ingelman *et al*, Proceedings of the HERA workshop, *ed.* R D Peccei, 1987
  - 14 Y Sirois, Lepton Identification section of Meeting on Simulation for Physics Analysis, DESY, H1-05/89-112 (1989)
  - 15 W W M Allison and J H Cobb, Ann. Rev. Nucl. Part. Sci. 30 (1980) 253

# Chapter 2: The H1 Forward Track Detector

## 2.1 Overview Of Forward Track Detector

The H1 Forward Track Detector (FTD), depicted in figure 2.1.1, covers the laboratory angles between  $5^\circ$  and  $30^\circ$  with respect to the proton beam direction. It occupies the cylindrical volume  $130 \text{ cm} < z < 259 \text{ cm}$ , and  $11 \text{ cm} < r < 88.8 \text{ cm}$ .

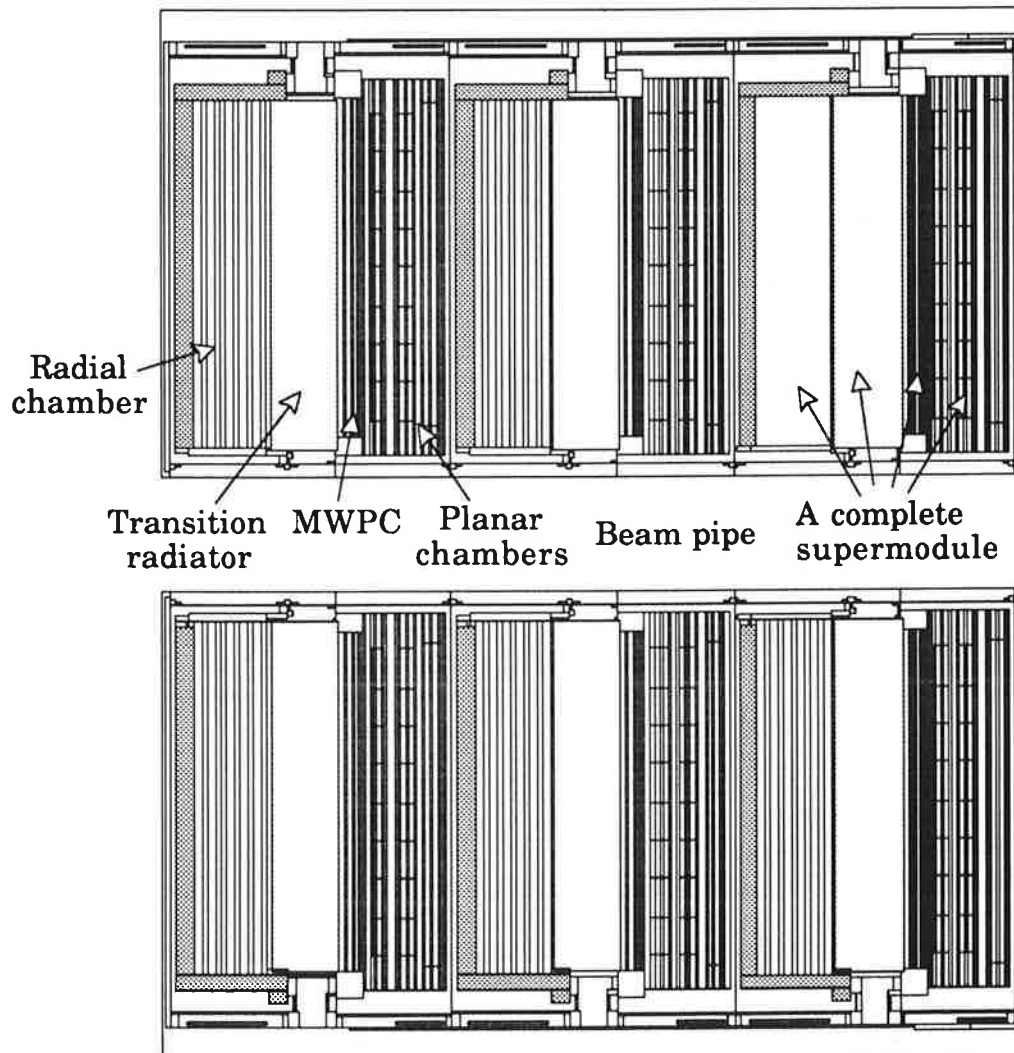


Figure 2.1.1 Layout of H1 Forward Track Detector.

The design objectives for the forward tracker are:

- good momentum resolution of tracks, with  $\sigma(p)/p^2 < 0.003 \text{ GeV}^{-1}$
- angular resolution of tracks with  $\sigma < 1 \text{ mrad}$
- efficient track pattern recognition
- efficient electron identification, with  $\pi$  contamination below 10% for particle momenta up to 60 GeV
- fast ray trigger, provided by the MWPCs, with the further possibility of a track trigger.

These objectives are subject to the overall constraint of introducing the minimum amount of material before the calorimeter.

The detector is realised as three ‘identical’ sub-units, known as supermodules. Each supermodule, when seen in “proton’s eye” view, consists firstly of three layers of planar geometry drift chambers, oriented at  $0^\circ$ ,  $\pm 60^\circ$  in  $\phi$ , followed by a MWPC, then transition radiator material, and finally a radial wire drift chamber. The principal difference between each supermodule is the rotational offset of each radial chamber about the  $z$  axis. This rotation ensures that a track which is unresolved behind another track, within the two-track resolution in one chamber, will be detected in front of this other track in the next chamber.

As each part of the supermodule uses a different gas mixture, Ar/C<sub>3</sub>H<sub>8</sub> for the planar chambers and MWPCs, He/CO<sub>2</sub> for the transition radiator and Xe/He/C<sub>2</sub>H<sub>6</sub> for the radials, the supermodule is housed in a correspondingly segmented gas tank. The tank also forms the mechanical

'back bone' for the FTD, supporting the FTD on rails inside the liquid argon cryostat.

## 2.2 Overview Of Radial Chamber

Each of the three radial wire drift chamber modules in H1 consists of 48 wedge shaped segments, each segment subtending  $7.5^\circ$  in  $\phi$ . Each wire plane, centred radially in the segment, consists of twelve sense wires, spaced apart by 1 cm along the beam direction, and eleven intermediate field wires, strung between a central hub and the outer shell. This radial segmentation is visible in figure 2.2.1, which depicts the mounting of the front field formers to the first production chamber. The sense wires are alternately staggered  $285 \mu\text{m}$  out of the true radial plane, to permit rapid resolution of the 'left/right' track ambiguity.

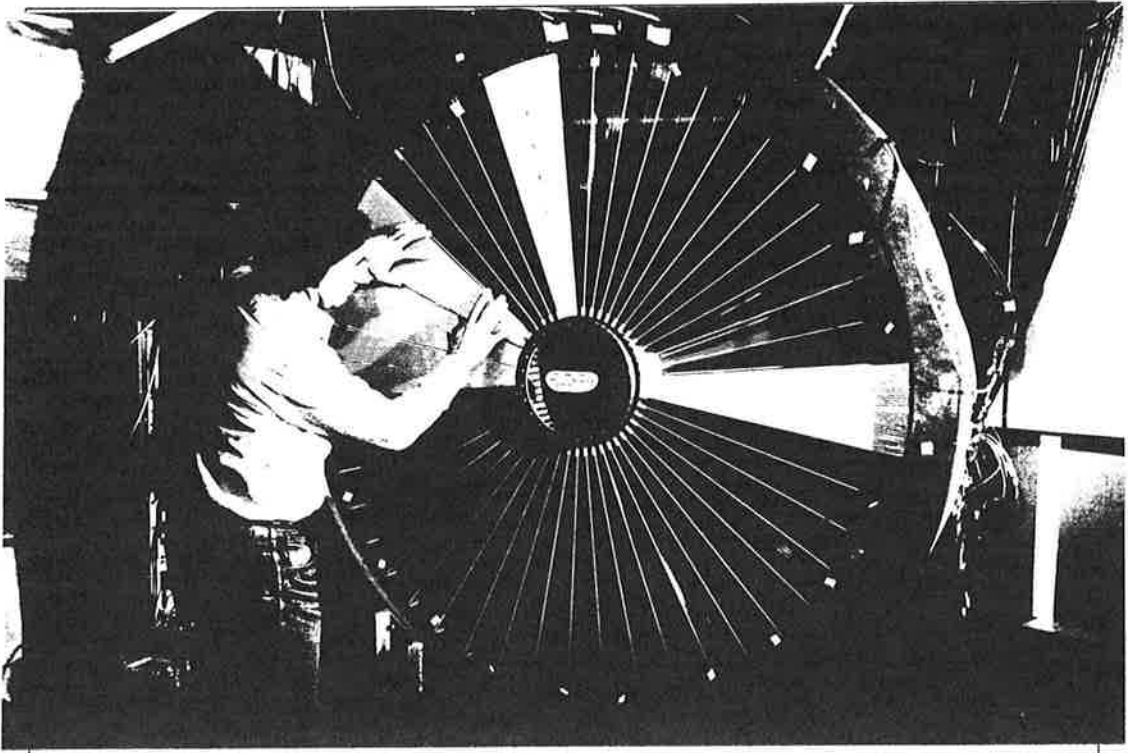


Figure 2.2.1 Photograph depicting the mounting of the front field formers to the first production chamber.

The radial wire geometry described above was dictated by the following reasoning:

- the available space is filled most efficiently, providing drift cells of smaller size at smaller radius, where track illumination is higher.
- multi-track pattern recognition is optimised, because a track makes hits which have a linear dependence of  $\phi$  on  $z$ . This is exploited in the pattern recognition, which starts by searching for track segments in individual radial chambers, before associating these segments into complete tracks along with hits from the planar chambers.
- the drift time measurement is an accurate determination of the track sagitta in the  $r\phi$  projection of the solenoidal magnetic field, so that optimum particle momentum precision may be achieved.

The field wires are 125  $\mu\text{m}$  diameter beryllium/copper and are electrically grounded to the preamplifier input. The sense wires are 50  $\mu\text{m}$  diameter Stablohm 800<sup>1</sup>. The simultaneous requirements, both of having the chamber operate in proportional mode for  $\frac{dE}{dx}$  measurements and of demanding total ionisation collection for efficient transition radiation (X-ray) detection, dictates the choice of relatively large diameter sense wires.

At the inner radius each sense wire is connected to its partner 105° away in  $\phi$ : each pair of wires is read out at the outer circumference of the chamber and the radial coordinate reconstructed from charge division along the pair. The sense signals are amplified close to the chamber us-

ing a differential input preamplifier, and recorded by 104 MHz 8-bit monolithic flash analogue-to-digital convertors (FADCs)<sup>2</sup>.

This geometry does have three major disadvantages:

- $r$  and hence  $\theta$  is only measured by charge division along the wire.
- particles in a jet with similar  $\phi$  coordinates are only moved apart slowly in  $\phi$  by the magnetic field. Thus any particles unresolved in one module tend to remain unresolved in the other modules. The effect of the chamber rotation is that overlapping hits remain unresolved, but that different tracks are resolved in each module.
- tracks with similar drift times, but different  $r$  coordinates (or possibly even in different connected cells) have their  $r$  measurements badly smeared: the charges seen at each end of the wire are the sum of the individual charges, with little information with which to resolve the contribution from each particle.

The planar chambers are included in order to address these shortcomings: they provide an orthogonal measurement for those tracks which are not resolved in the radials, thereby improving two-track resolution within a jet. They also improve the  $r$  and  $\theta$  precision, when planar hits have been correctly associated with radial track segments. The geometry of the planar chambers is sketched in figure 2.2.2. This may be contrasted with that of the radial chamber in figure 2.2.1.



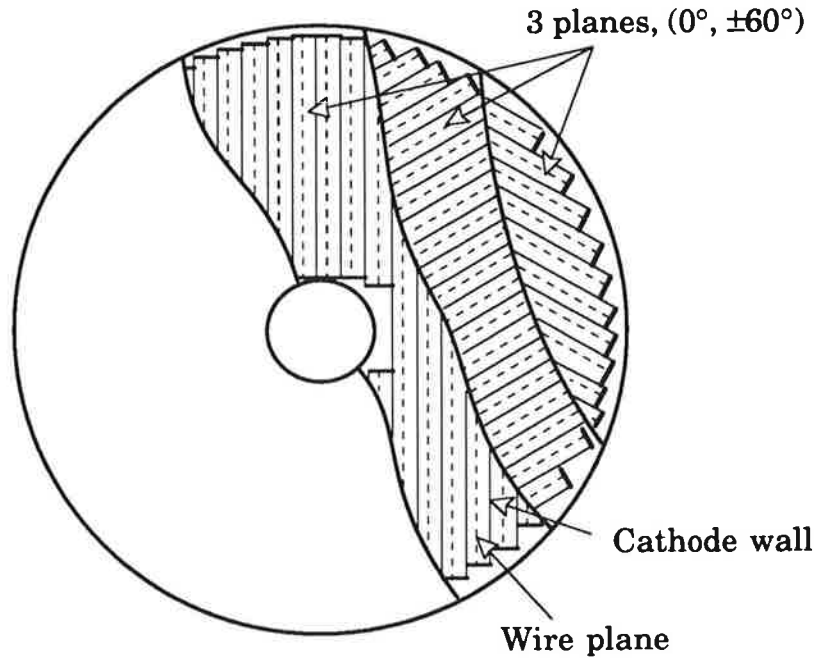


Figure 2.2.2 Schematic of a Planar Supermodule element showing the three wire plane orientations.

The inclusion of a transition radiator in the FTD complements the  $e/\pi$  discrimination provided by the calorimetry, particularly for particle energies of less than 100 GeV. The detection of the TR X-ray signal in a high resolution ‘conventional’ tracking chamber is a novel departure, removing the need for a separate X-ray detector. This emphasis on tracking is a direct contrast to the first combined TR detector (TRD) and track detector, which formed part of the HELIOS experiment<sup>3</sup>. The HELIOS TRD was based on MWPCs, with the emphasis on the TR detection, although it also aimed to provide some track information. The combination of track detection with TR detection raises the possibility of enhanced  $e/\pi$  discrimination over and above that obtainable with a dedicated TRD<sup>4</sup>; the precise spatial reconstruction of each track segment whose  $\frac{dE}{dx}$  measurements are used in the  $e/\pi$  discrimination means that much of the usual “knock-on” background which is present in other TR detectors can be recognised and eliminated.

## 2.3 Radial Chamber Construction

The chamber shell consists of a thin 'saucepan-like' structure made of nomex and kevlar epoxy composite, sketched in figure 2.3.1. This comprises 0.5 mm kevlar skins bonded to a honeycomb array of nomex, an increasingly widely used construction technique where maximum rigidity is required with minimum weight<sup>5</sup>. The use of these materials means that none of the chamber contains any silicon based material, thereby eliminating one potential cause of premature chamber aging<sup>6</sup>. The shell is manufactured using a cold lay-up procedure to achieve the required precision<sup>7</sup>. It is rigid enough to support the tension of the sense and field wires strung radially between the outer walls and an inner 'hub' made of noryl<sup>8</sup>, a stable and readily machinable thermoplastic.

The outer rim of the chamber shell provides the means by which it is supported in the gas tank and aligned with the other elements of the FTD. For this purpose there are aluminium inserts in the shell rim, which are machined to form bolt holes and two dowel holes. These dowels provide the alignment with the rest of the detector. The open face of the chamber is sealed by a thin front X-ray transparent window. Radial 'dividers' with conducting strips (cathode planes), which provide the necessary radial voltage gradient for uniform transverse drift field, separate the structure into the 48 'wedges', each of which forms a self contained transverse drift chamber with 12 sense wires. Field forming strips close the electrostatic field cage on the front and back surfaces of the chamber and permit fine tuning of the gas gain on the first and last sense wires.

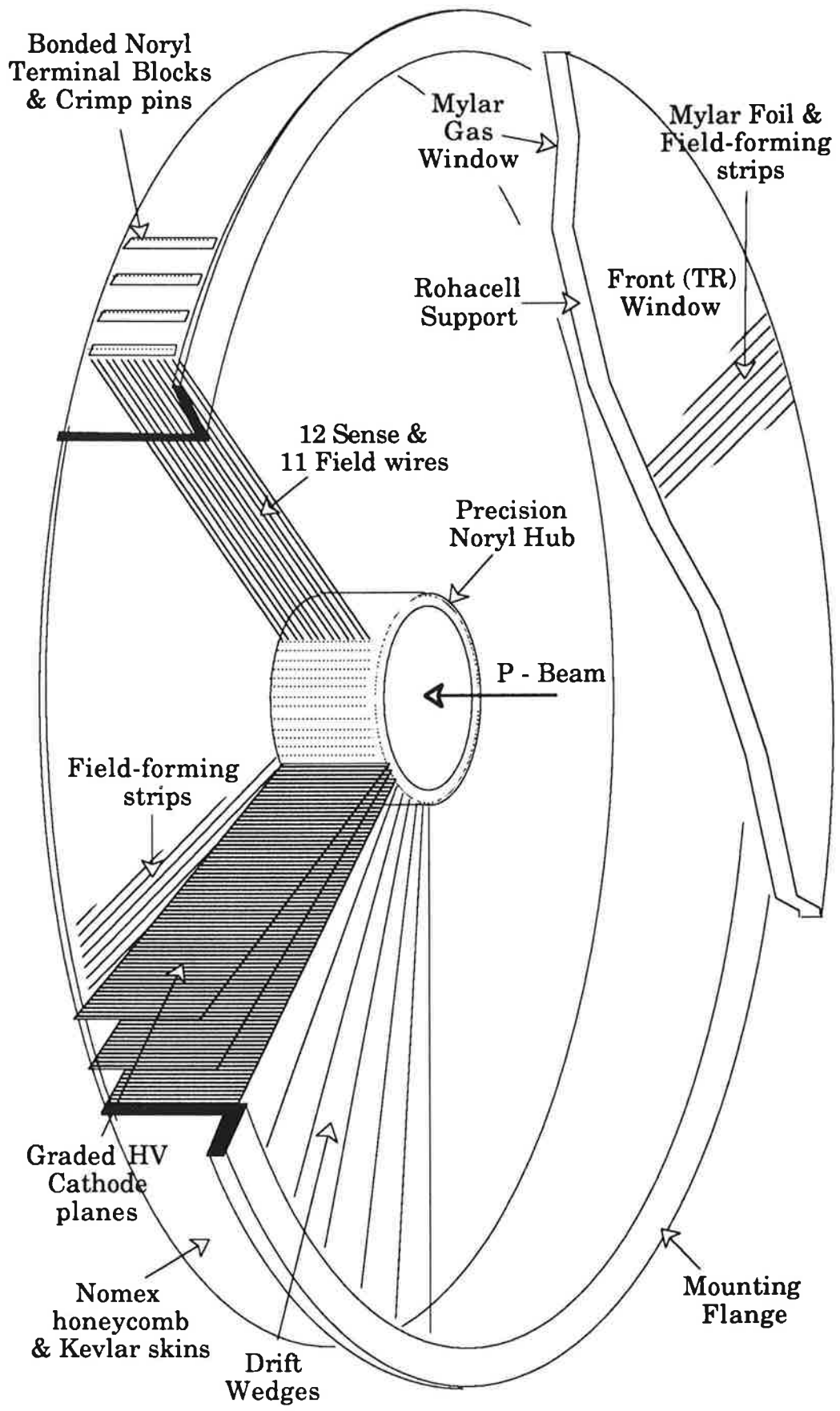


Figure 2.3.1 Exploded diagram of radial chamber.

The accurate location of the sense and field wires is achieved by means of precision jigs. The composite shell with the inner location ring is positioned accurately on a jig plate made of unstressed aluminium whose surface and dowel holes are machined to 25  $\mu\text{m}$ . All the feed-through holes are then drilled. After the central hub<sup>9</sup> containing the holes for the wire crimp pins has been correctly positioned on the jig plate, the supports for the other ends of the wires can be mounted by means of jigs attached to the plate at the outer radius. The 12 sense and 11 field wires of each wedge are supported at the outer radius by a noryl template block, in which holes have been accurately drilled to hold the crimp pins.

The radial position of each template need not be known to the same degree of accuracy as azimuth  $\phi$  and  $z$ , and the concentricity of the outer surface of the composite frame is not guaranteed to such tolerance. Therefore an oversize shim of noryl is glued in position, then machined away to produce an accurately orientated backing plate on which to mount the template. The template is then glued in position using a thin film of glue. In this way the high precision of the jig plate is used to align the wire pins on the outer rim with their partners on the inner hub, despite the fact that the composite structure cannot be manufactured to the same high accuracy.

The templates and the central hub are machined from noryl, rather than from metal, in order to reduce the amount of material before the EM calorimeter. Extensive measurements of the finished parts demonstrate that the desired precision of less than 30  $\mu\text{m}$  can be reliably achieved, although the thermal expansivity of the plastic ( $\sim 50 \text{ ppm } ^\circ\text{C}^{-1}$ ) needs to be taken into account over distances greater than a few centime-

tres. Figure 2.3.2 shows the mean hole residuals, after subtracting off the wire stagger, for the hub and templates used in the second production chamber. The error bars are the RMS scatter for each hole about the mean (cross checks in the measurements show that the measurement precision is around the  $3\ \mu\text{m}$  level). The odd holes correspond to the alternately staggered sense wire holes, the even holes to the field wire holes. The remaining stagger visible in the measurements for the hub corresponds to the hub having a mean stagger of  $290\ \mu\text{m}$  rather than the nominal  $285\ \mu\text{m}$ . The scatter and errors on the mean values are consistent with there being no other source of systematic distortion.

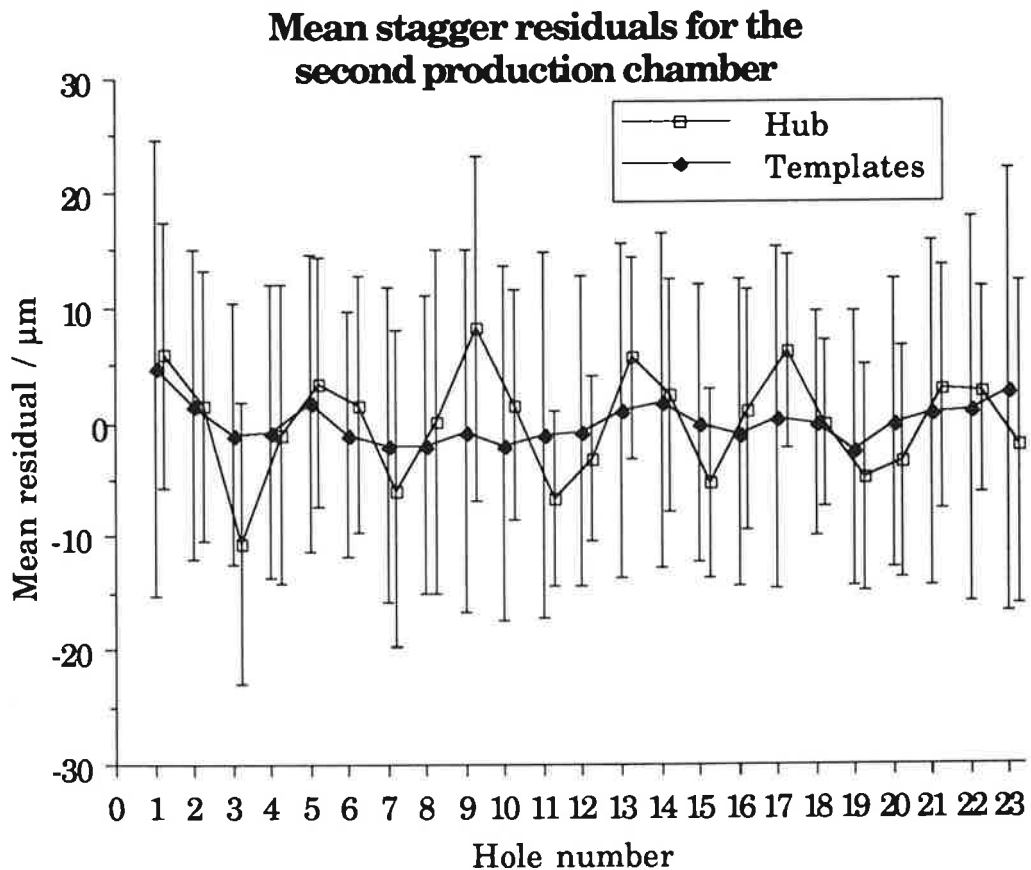


Figure 2.3.2 Plot of residuals versus hole number for one of the production chambers.

Once the hub and terminal blocks are mounted, the locating strips for the cathode planes are inserted, again making use of the jig table. The

rear field shaping electrodes are also bonded to the composite shell at this stage. These electrodes consist of 2 mm wide copper strips with 3 mm spacing, on 0.3 mm paper-epoxy<sup>10</sup>.

With the electrodes in place the chamber may then be wired. The open structure of the chamber makes wiring extremely easy; the wires are fully accessible even when the chamber is fully strung. Figure 2.2.1 shows the chamber mounted on the wiring jig, albeit after the assembly of the front window. The wires are strung in the horizontal plane, tensioned by weights (170 g for the sense wires, 280 g for the field wires) and then crimped. The order in which wedges are wired is staggered to ensure a uniform build-up of stress in the structure. The excellent accessibility combined with the large diameter sense wires results in each chamber comprising of 1104 wires taking typically 15 days to wire.

The cathode planes are made from 0.6 mm thick paper-epoxy printed circuit board ( $1 X_0 \approx 40$  cm), laminated on each side with 17  $\mu$ m copper using standard manufacturing techniques. The conductor on each face is segmented into 86 strips each 6 mm wide (along the radial coordinate) and separated by 1 mm. The strips are connected in series by 10 M $\Omega$  surface mount resistors (SMR) located near the back of the chamber, such that they are coplanar with the backmost field wire. They are supported in position by means of accurately machined slits on the central hub and small noryl guides on the inner surfaces of the composite frame.

The performance of the detector depends critically on the careful design of the front window, which must not only be X-ray transparent (in the energy range  $1 < E_\gamma < 20$  keV), but also support field forming electrodes. The electrodes are necessary to ensure that X-ray energy deposition can

be detected as close as possible to the front of the first drift cell. This is of paramount importance when trying to achieve good TR photon detection, as even with a 30% xenon gas mixture, the mean free path of 10 keV X-rays is 35 mm. Field strips mounted inside the chamber would introduce a serious loss of efficiency for primary ionisation within the first few mm of the gas volume<sup>11</sup>. Therefore the strips are positioned upstream, on a rigid supporting layer of 5 mm rohacell foam<sup>12</sup>, in order to minimise the losses arising from the strip structure. The TR photon yield is not compromised by this arrangement. Indeed, rohacell has been investigated as a candidate radiator in its own right<sup>13</sup>; although it is not as effective a radiator as foils or fibres, it is one of the few rigid transition radiator materials.

The gas seal at the front of the chamber is provided by a 50  $\mu\text{m}$  thick mylar gas window positioned 5 mm from the first sense wire, coincident with the location of the extrapolated periodic drift cell boundary. This window is held taut and bonded to an inner noryl ring and an outer ring of resin-impregnated wood<sup>10</sup>. Slotted noryl strips 2 mm wide are bonded onto the inside surface to locate the upstream edges of the cathode plates. The electric potential at the front of the chamber is maintained by the external 12  $\mu\text{m}$  thick aluminium strips 2 mm wide with 3 mm spacing, mounted on 25  $\mu\text{m}$  polyester film<sup>14</sup>. With this construction the electrostatic field is similar in all drift cells and ionisation produced immediately inside the chamber is collected efficiently. The field is parallel to the gas window along most of its surface so that charging effects due to ionic accumulation are small.

## 2.4 Summary

The emphasis on using composite materials and plastics in the construction of the FTD results in a very low mass detector. The material distribution as seen by a particle originating from the interaction point is shown in figure 2.4.1. The peaks in the distribution in general arise from those parts of the detector where the requirements of rigidity prevent the use of composites, such as the inner hub of the radials and the gas tank flanges.

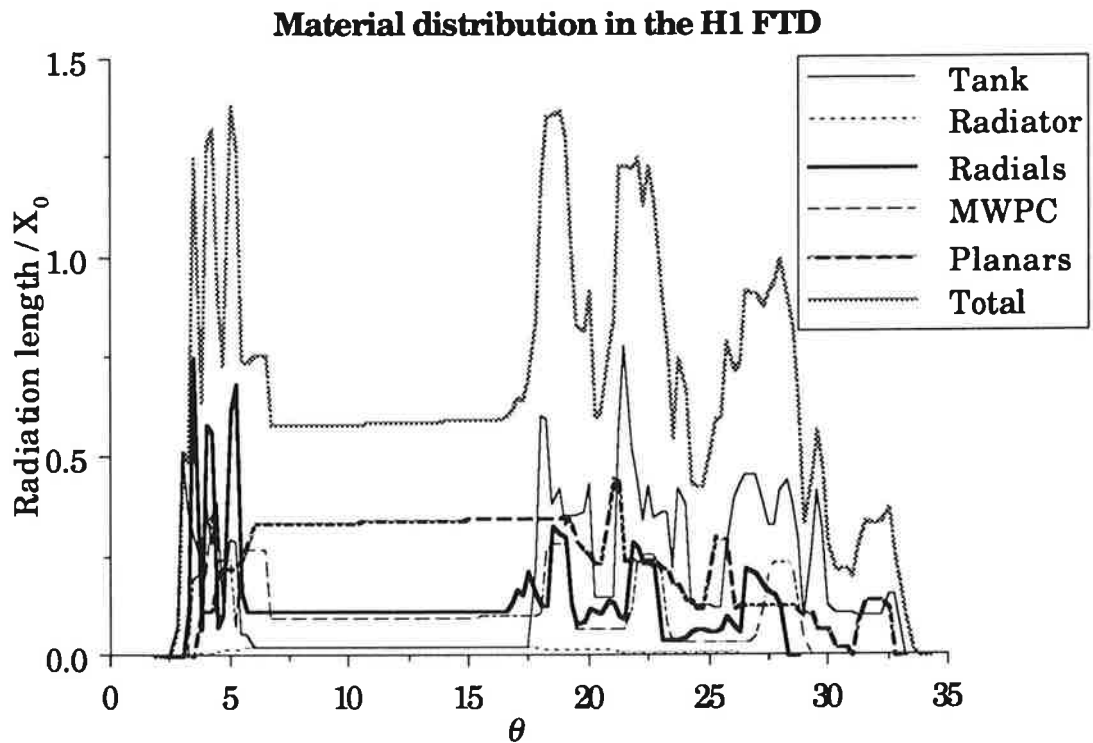


Figure 2.4.1 Material distribution of the FTD measured in terms of radiation lengths traversed by particles coming from the interaction point.

The open geometry of the radial chambers means that the bulk of the material is concentrated at the inner and outer radii; the active volume contains minimal material, in contrast to the more uniform distribution



of material in the planar chambers. In any case there is everywhere the minimum amount of material before the electromagnetic calorimeters.

---

- 1 CrNiAlCu alloy manufactured by California Fine Wire Company, Grover City, Ca., USA
- 2 W Zimmerman, DESY, Struck F1000 FADC system
- 3 H Gordon *et al.* CERN SPSC/83-51, SPSC/P189 (1983)
- 4 B Dolgoshein NIM A252 (1986) 137
- 5 Hunting Composite Review (1989), private communication, Hunting Composites
- 6 J Va'Vra NIM A252 (1986) 547
- 7 Hunting Composites, Havant, Hants, UK
- 8 Noryl: polyetherpolyphenylene plus 6% filler (titanium oxide)
- 9 Hub and templates machined by Marcus Engineering, Wirral, UK
- 10 Permali Ltd, Gloucester, UK
- 11 J Allison *et al.*, NIM 201 (1982) 341
- 12 Röhm GmbH, Darmstadt, FRG
- 13 Appuhn *et al.* NIM A263 (1988) 309
- 14 Yeovil Circuits, Yeovil, Somerset, UK

# Chapter 3:

## Electrostatics Of The Radial Chamber

### 3.1 Introduction

The radial chambers in H1 differ from 'conventional' drift chambers in a number of ways, for example by virtue of the cell taper, as illustrated in figure 3.1.1. The cell dimensions are those used for the 1987 test chamber (the test chambers are described in detail in chapter 4). However the basic principles governing the design are the same as for any other drift chamber. Figure 3.1.2 shows the chamber cut through the slice marked A A' in figure 3.1.1. The similarity in this projection with any other "transverse drift" wire chamber, where the primary ionisation is collected by drifting perpendicular to the incident charged particle track, is obvious. Before considering the complexities introduced by the cell taper and the requirements of efficient charge collection for X-ray detection, it is instructive to first investigate the behaviour of a 'conventional' drift chamber.

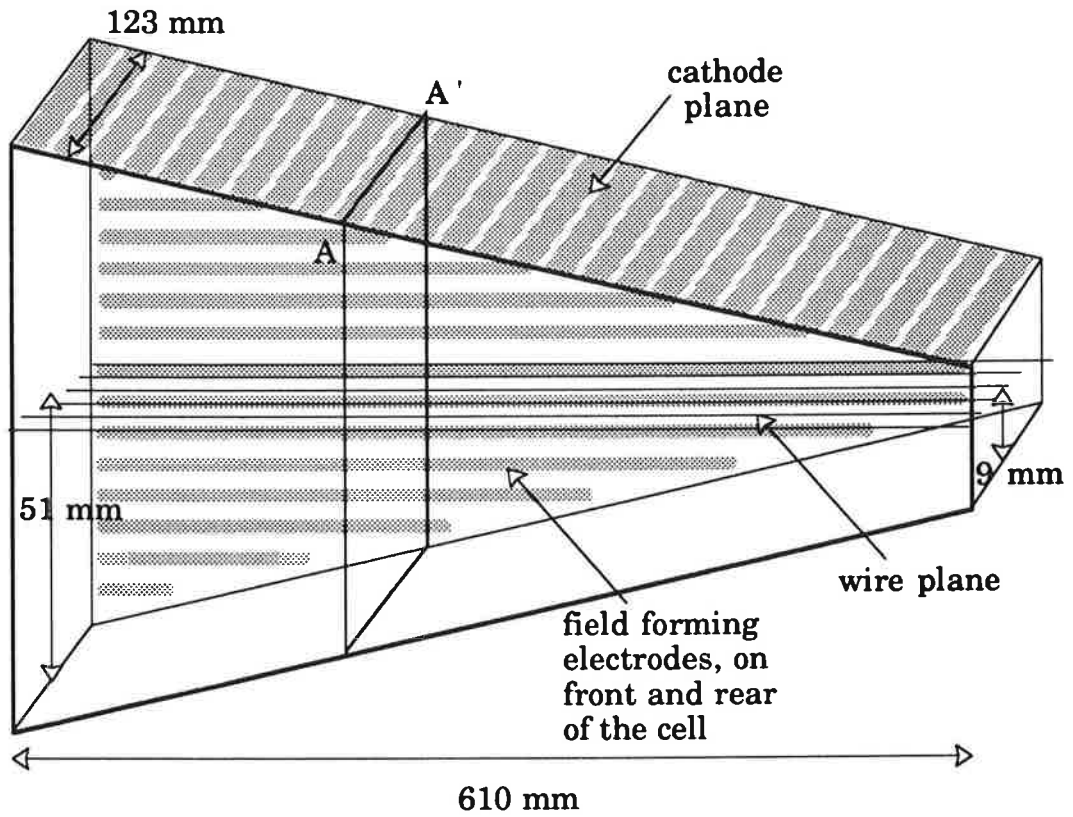


Figure 3.1.1 Perspective view of drift cell.

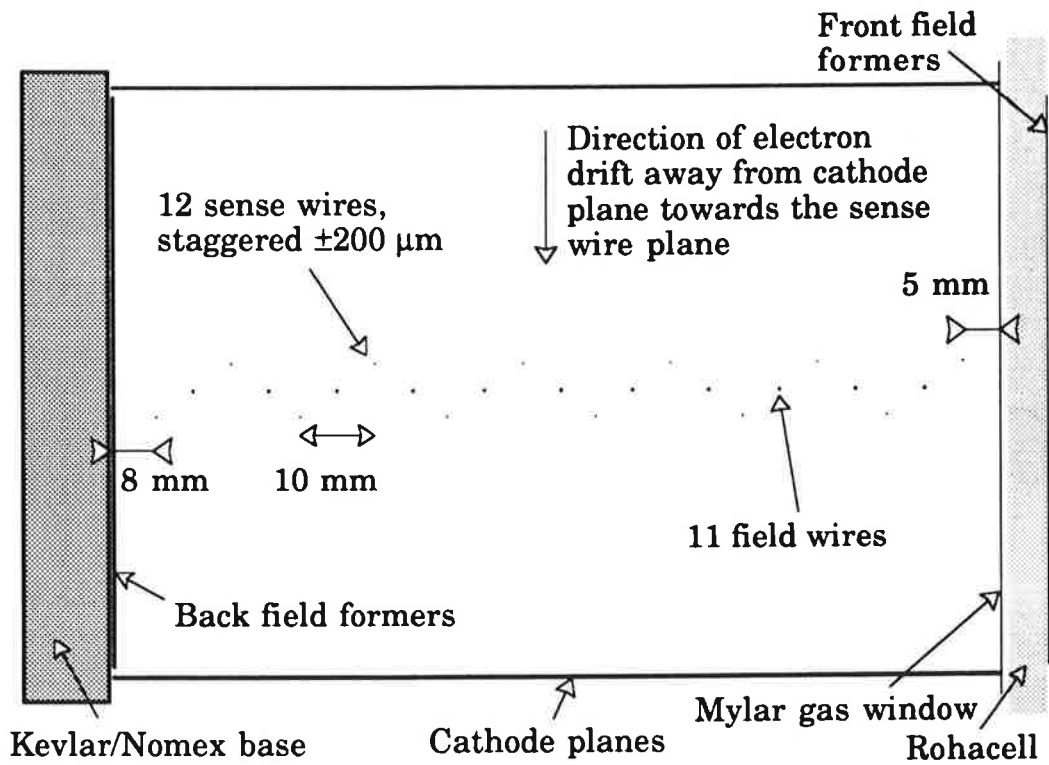


Figure 3.1.2 Cut through the plane A A'.

## 3.2 Electrostatics Of A Conventional Drift Cell

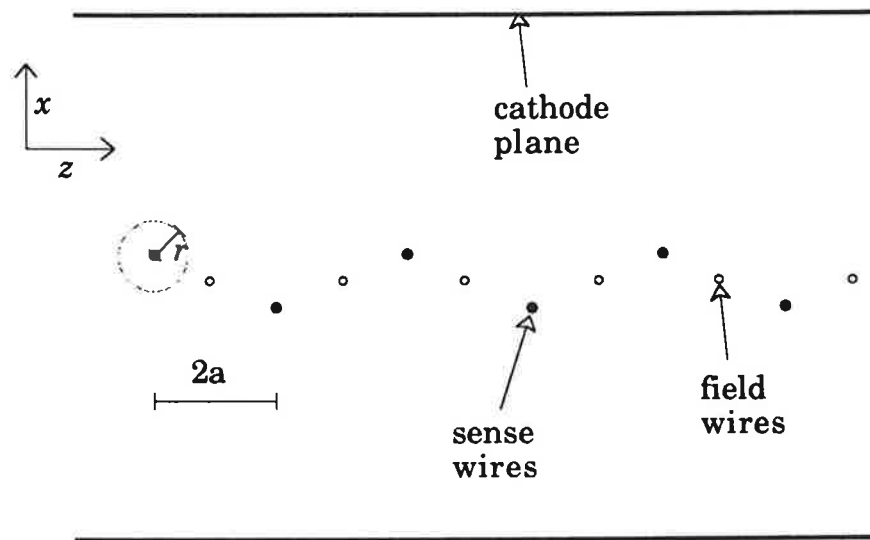


Figure 3.2.1 Sketch of 'ideal' drift cell.

At a small radius  $r$  from the nearest wire, the electric field due to an infinite array of wires, represented by line charges of equal strength  $\sigma$  per unit length and spacing  $2a$  (figure 3.2.1) is given by:

$$E(r) = \frac{\sigma}{2\pi\epsilon_0 r} \quad [3.2.1]$$

At a sufficiently large distance the structure of the array is not discernible; away from the wire plane, it looks like a uniform plane of charge density  $\frac{\sigma}{2a}$ , with the field given by:

$$E_D = \frac{\sigma}{4\epsilon_0 a} \quad [3.2.2]$$

Gauss' theorem gives the following important relationship between the drift field  $E_D$  and the field at the surface of the wire,  $E_s$ , for a drift chamber consisting of a uniform array of wires of radius  $R$ , separation  $2a$ , between two widely spaced cathode plates :

$$E_s = E_D \cdot \frac{2a}{\pi R} \quad [3.2.3]$$

For a drift field of  $1 \text{ kV cm}^{-1}$ , and sense wires of  $50 \text{ }\mu\text{m}$  diameter separated by  $1 \text{ cm}$  as in the radial chambers, this gives the field at the wire surface as  $127 \text{ kV cm}^{-1}$ . From measurements of the gas gain<sup>1</sup> this combination of wire diameter and field corresponds to a gas gain of about  $2 \times 10^4$  in HRS gas (Ar/CO<sub>2</sub>/CH<sub>4</sub> 90/10/1). This is comfortably in the proportional region.

Returning to the array of line charges, a good approximation to the electric potential is given by:

$$V(x, z) = V_0 - \frac{\sigma}{4\pi\epsilon_0} \cdot \ln \left\{ 4 \left[ \sin^2 \left( \frac{\pi z}{2a} \right) + \sinh^2 \left( \frac{\pi x}{2a} \right) \right] \right\} \quad [3.2.4]$$

where the charge is situated at  $x = 0, z = 0, \pm 2a, \pm 4a$  etc<sup>2</sup>.  $V_0$  represents an arbitrary offset potential.

The equipotentials are circular close to each wire. At a distance  $x$  from the wire plane comparable to the wire spacing they are parallel to the  $z$  axis and almost straight: the deviation from linearity across the cell is  $\pm 0.28 \text{ mm}$  at  $x = 5 \text{ mm}$ ;  $\pm 6 \text{ }\mu\text{m}$  at  $x = 10 \text{ mm}$ ;  $\pm 0.01 \text{ }\mu\text{m}$  at  $x = 20 \text{ mm}$ . At distances of the order of a centimetre the effect of the wire structure is quite negligible, leading to:

$$V(x) = V_0 - x \cdot E_D \quad [3.2.5]$$

$$V_f = V_0 - E_D \cdot \frac{a \cdot \ln 4}{\pi} \quad [3.2.6]$$

$$V_s = V_f + E_D \cdot \frac{2a}{\pi} \cdot \ln \left( \frac{2a}{\pi R} \right) \quad [3.2.7]$$

where  $V_s$  denotes sense wire potential, and  $V_f$  the potential at the turning point mid-way between wires where in general the guard or field wires would be located. Equation [3.2.5] is the asymptotic limit at large  $x$  of equation [3.2.4]. The effect of the wire radius is merely to determine

the sense wire potential and surface field, and it has no effect on the shape of the potential surface outside the wire.

For a given geometry there is only one free field parameter ( $E_D$  above), and an arbitrary choice for zero potential which does not affect the physics of the cell.

The same equation that is satisfied by the electric potential in free space (Laplace's equation) also applies to the deformation of a uniformly tensioned elastic membrane ("stretched rubber sheet"); this analogy has been used previously for photomultiplier design<sup>3</sup>. It has also provided a quick way of understanding the more complicated corners of the drift cell electrostatics of the radial chamber, and of checking some of the numerical calculations.

### **3.2.1 The Effect Of Introducing Field Wires**

With the electrostatic arrangement outlined above there is no possibility of independently varying the gas gain and the drift field. This variation may however be achieved by inserting field wires mid-way between the sense wires, as indicated in figure 3.2.1. More importantly the field wires also provide de-coupling of the cross-talk between neighbouring cells, this being one of the reasons for the use of double guard wires in many chambers<sup>4</sup>.

The principle of superposition allows the application of equation [3.2.4] twice, once for charges centred on the sense wire positions and again for charges centred on the field wire positions. This leads to an overall electric field, comprising the sum of the separate drift fields due to the sense wires and the field wires,  $E_D$ , and  $E_{D_f}$ :

$$E_D = E_{D_s} + E_{D_f} \quad [3.2.8]$$

Sense wire surface field, from equation [3.2.3]:

$$E_s = E_{D_s} \cdot \frac{2a}{\pi R_s} \quad [3.2.9]$$

Defining the potential of the field wires as zero then fixes the sense potential, from equation [3.2.7]:

$$V_s = \frac{2a}{\pi} \cdot \left\{ E_{D_s} \cdot \ln \left( \frac{2a}{\pi R_s} \right) - E_{D_f} \cdot \ln \left( \frac{2a}{\pi R_f} \right) \right\} \quad [3.2.10]$$

and the cathode voltage, valid for distances greater than the wire spacing:

$$V(x) = V_0 - x \cdot E_D \quad [3.2.11]$$

with the constant term given by:

$$V_0 = \frac{2a}{\pi} \cdot \left\{ E_{D_s} \cdot \ln 2 - E_{D_f} \cdot \ln \left( \frac{a}{\pi R_f} \right) \right\} \quad [3.2.12]$$

In terms of the sense wire potential and the drift field and units of kV and cm, with constants evaluated for the radial wire drift cell geometry ( $a = 0.5$  cm,  $R_s = 25 \times 10^{-4}$  cm,  $R_f = 62.5 \times 10^{-4}$  cm), this gives<sup>5</sup>:

$$E_s = 45.7V_s + 57.1E_D \quad [3.2.13a]$$

$$E_f = 28.1E_D - 18.3V_s \quad [3.2.13b]$$

$$V_0 = 0.449V_s - 0.469E_D \quad [3.2.13c]$$

where  $E_s$  is the sense wire surface electric field, and  $E_f$  is the field wire surface electric field. The transformation between the two sets of independent variables  $V_s$ ,  $E_D$  and  $E_D$ , and  $E_{D_f}$  is derived from equations [3.2.8] and [3.2.10]:

$$\begin{bmatrix} E_{D_s} \\ E_{D_f} \end{bmatrix} = \begin{bmatrix} \frac{2a}{\pi} \ln\left(\frac{2a}{\pi R_s}\right) & -\frac{2a}{\pi} \ln\left(\frac{2a}{\pi R_f}\right) \\ 1 & 1 \end{bmatrix}^{-1} \begin{bmatrix} V_s \\ E_D \end{bmatrix} \quad [3.2.14]$$

Since there are only two free parameters, here drift field and sense wire voltage, all operating conditions can be displayed as contours on a 2-D plot (figure 3.2.2), and because the above relations are linear they all appear as straight lines on this plot.

There are two special lines on this plot which define the limits for operation of the chamber:

- $E_f = -20 \text{ kV cm}^{-1}$ :

This is a commonly accepted operational limit beyond which chambers start to run into problems with field emission from the field wires.

- $E_f = 0$ :

This corresponds to zero charge on the field wires. Below this line the field wires are positively charged and therefore capture electrons from a portion of the cell. This portion is then effectively dead, leading to a loss of primary ionisation and proportionally reduced detection efficiency for spatially localised energy deposition, such as is produced by X-ray absorption. Therefore  $E_f = 0$  defines the boundary for acceptable operation of the cell as an X-ray or transition radiation detector.



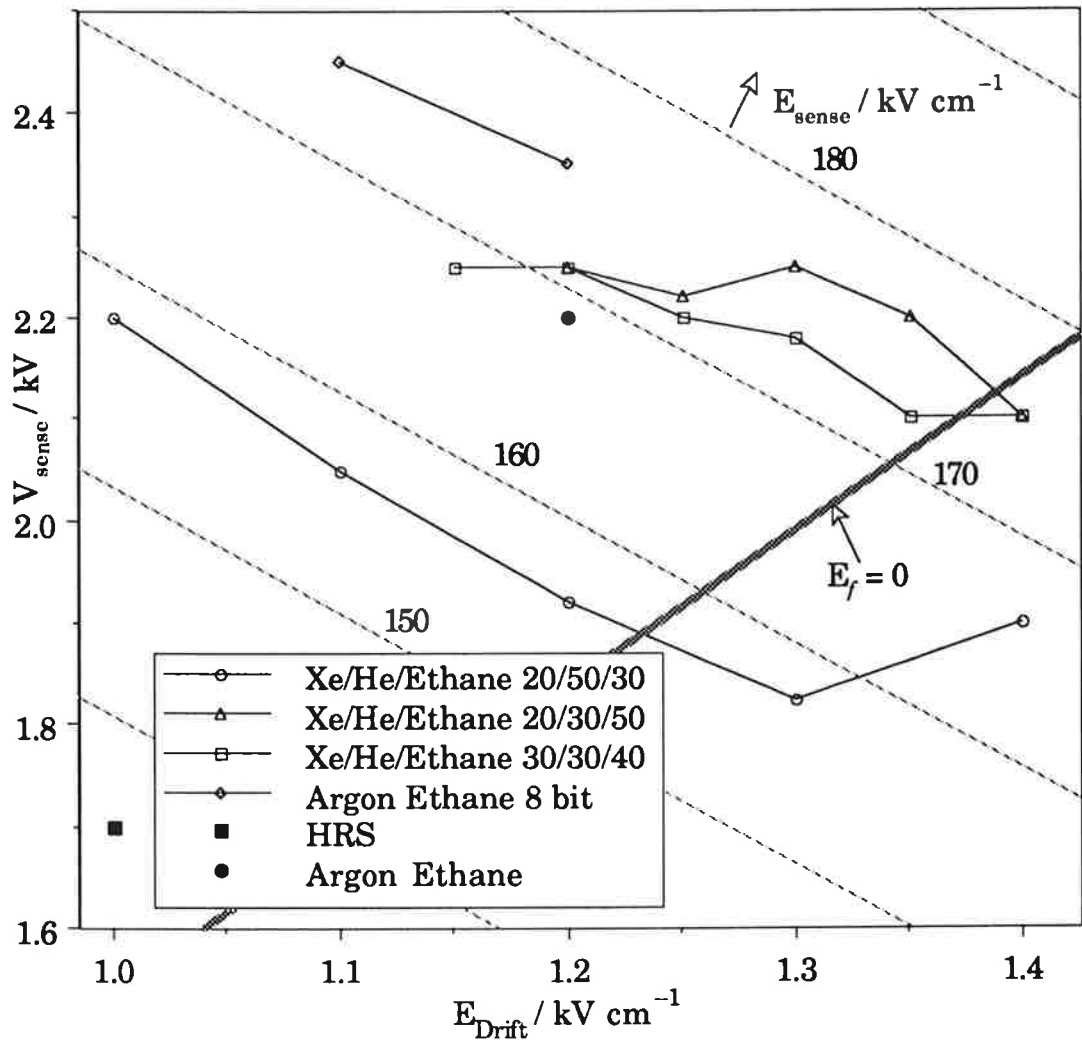


Figure 3.2.2 Chamber Operating Conditions

Above the line  $E_f = 0$  (tending towards higher gain and lower drift field) the field wires are negatively charged; drift trajectories are focussed towards the sense wires, thereby improving isochronicity.

On the line  $E_f = 0$  the field wires are uncharged. In principle the drift trajectory for ionisation produced arbitrarily close to the cell boundary makes a right-angled turn at the wire plane, so that its drift length is longer by 5 mm than that for ionisation deposited in the centre of the cell. The spectrum of drift paths (and to a good approximation drift times) is at its worst in this case. For a given cell geometry and gas mixture this configuration gives the minimum gas gain consistent with the

collection of all primary ionisation. It is this constraint, brought about by the simultaneous requirement for  $\frac{dE}{dx}$  measurements and total ionisation collection, which led to the choice of 50  $\mu\text{m}$  diameter sense wires.

Also shown in figure 3.2.2 are the operating points which were found for the radial drift cell tests at DESY. During the first series of tests an initial drift field was chosen, and the cathode potentials set up corresponding to equation [3.2.4] *et seq.* The sense potential was then adjusted (with the electron beam in a particular region of the wedge) to give a “standard” pulse height on the oscilloscope. The chosen potentials are seen to follow the lines of constant  $E_s$ , and correspond to a gas gain of about  $4 \times 10^4$  for the argon/ethane and HRS gases, as measured by the CDF group. The later inclusion in the theoretical model of the effects of charged field wires leads to an expected variation of gain with radial coordinate; this effect was observed in the off-line analysis. In the second set of tests equations [3.2.11] and [3.2.13] were applied iteratively, by first choosing a sense wire voltage and drift field, optimising the pulse height by varying the sense wire voltage, and then recalculating the correct voltages. With hindsight it was decided that a larger pulse height than in the first series of tests was necessary.

### 3.3 Consequences Of The Wedge Shape

The major geometric difference between the radial chambers and a “conventional” drift chamber is the wedge shape of the drift cell. This however causes only a minor increase in the complexity of the design. For example, consider a rectangular chamber with parallel cathodes, viewed along the wire plane and perpendicular to the wires

(figure 3.3.1). Once the electrode potentials are given, the electric potential  $V(x,z,R)$  has been defined at every point in the chamber volume. On insertion of a finely segmented radial set of electrodes  $C'$ , maintained at the potentials given by  $V$ , it is possible to remove the original cathodes without changing the field inside  $C'$ . This segmented set of electrodes corresponds to the chamber boundary in the radial wire drift cell.

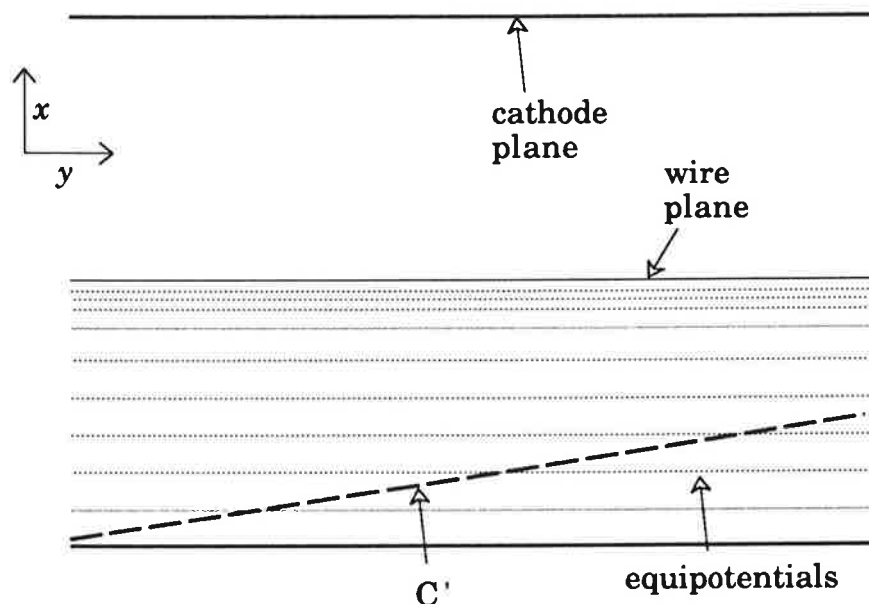


Figure 3.3.1 Sketch of rectangular drift chamber.

As the electric potential in this region of the radial drift cell is linear to better than 1%, the minimum cathode:wire spacing being 9 mm, the required potential on the radial electrodes  $C'$  is also linear in  $x$  as given by equation [3.2.11].

This linear potential can be achieved with radial cathodes consisting of strips running parallel to  $z$ , held at the required potential by a resistive divider chain. The alternative solution of a uniform resistive coating on the cathode planes was found not readily to be feasible. In practice, each strip has a finite width along  $R$ , and is separated from its neighbour by a finite gap (in the 1987 test cell these were 6 mm and 4 mm respectively,

which was far from ideal). The nature of these effects on the shape of the electrostatic field is sketched in figure 3.3.2.

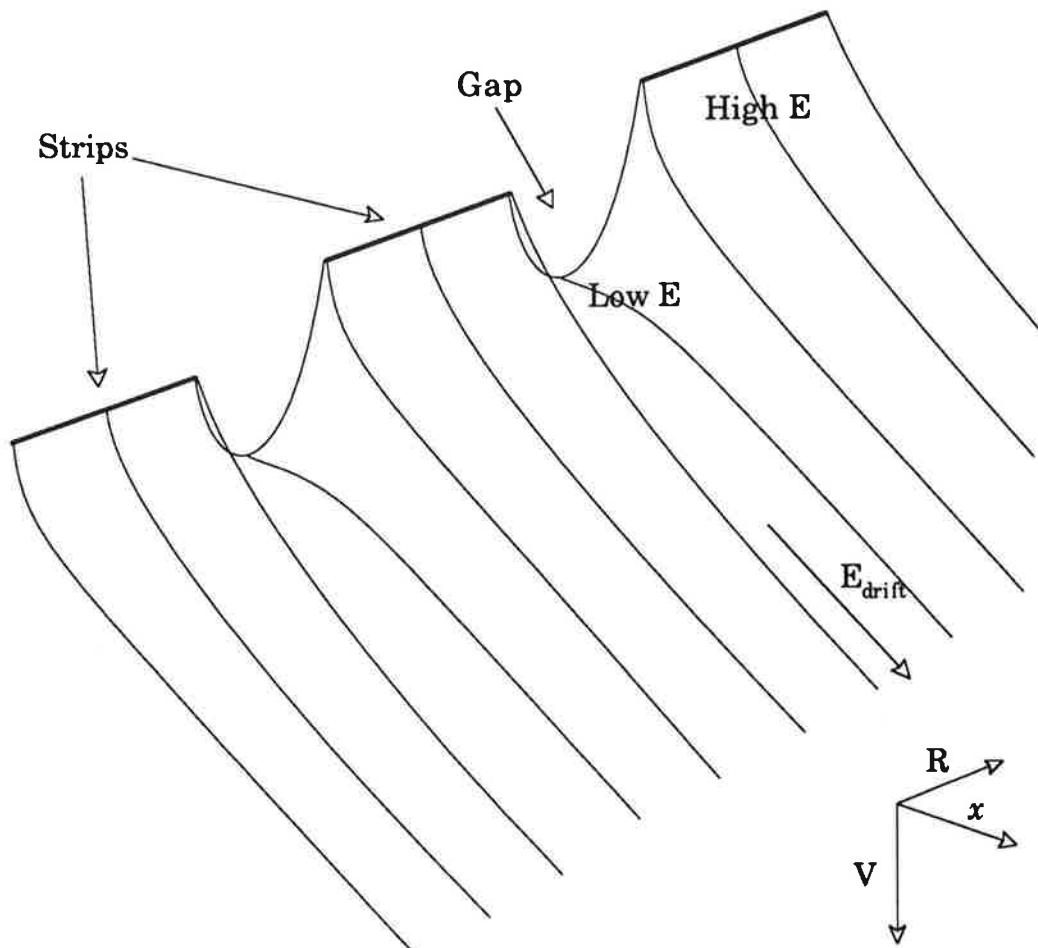


Figure 3.3.2 Sketch of electrostatic potential in neighbourhood of segmented cathodes.

The electrostatic potential is constant on the surface of each strip, whereas in principle it should increase along the R coordinate. This leads to a discrepancy from the ideal potential at the edges of the strip of:

$$\Delta V = \pm w \cdot E_D \cdot \frac{\pi}{96} \quad [3.3.1]$$

where  $w$  is the width of the strip, and the cell geometry has been taken into account. This effect was simulated, with a drift field of  $1.4 \text{ kV cm}^{-1}$ , for strips with zero space between them and the fraction of the cell for

which the field differed by more than 2% from the mean value was calculated, for a cell with 10 mm drift length<sup>5</sup> (table 3.3.1).

Strip width/mm	$\Delta V$	% cell affected
4	18	8
6	27	12
8	37	16

Table 3.3.1 Fraction of cell with distorted electric field for various strip widths.

Across the gap the potential drops slightly. This has been simulated, for four different gap values, all for 10 mm pitch (table 3.3.2).

Strip width/mm	Gap/mm	$\Delta V$	% cell affected
6	4	270	40
7	3	198	35
8	2	127	23
9	1	56	4

Table 3.3.2 Fraction of cell with distorted electric field for various strip:gap ratios.

These suggest that a gap of 2 mm or greater would be the dominant source of field distortion, with a marked improvement as the gap is reduced below 2 mm. The regions of the cell affected by a 2 mm gap and 6 mm strips are mapped out in figure 3.3.3.

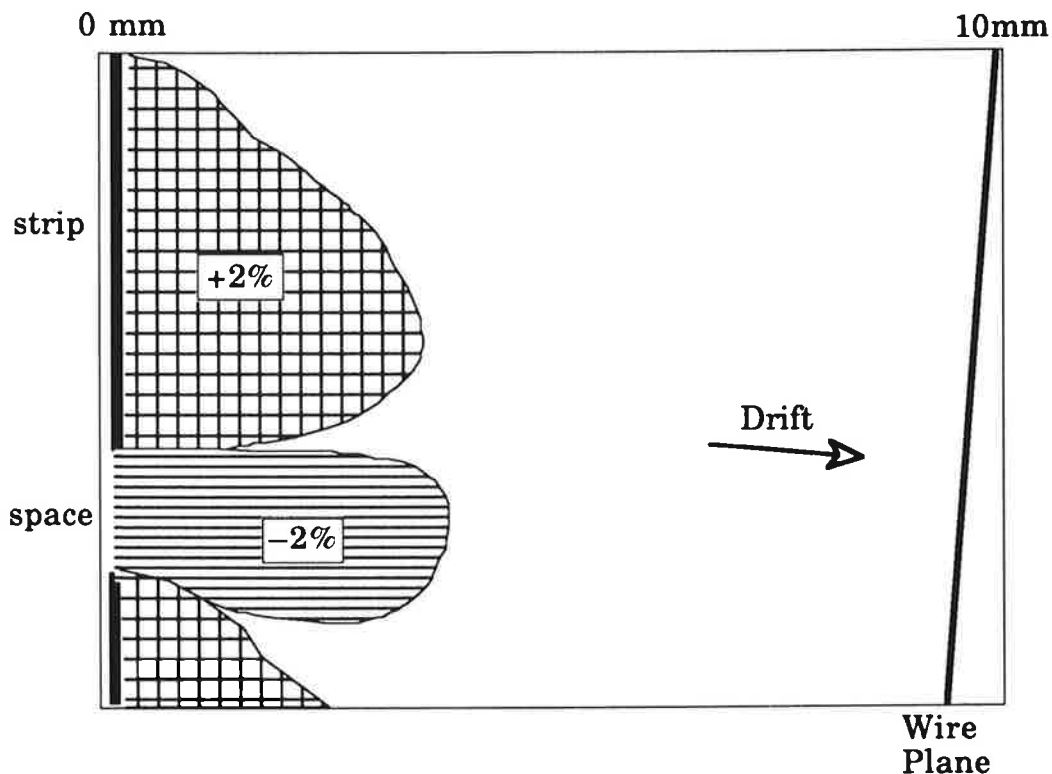


Figure 3.3.3 Field distortion due to cathodes with 6 mm strips and 2 mm gaps.

In general the minimum distortion occurs for a strip:gap ratio of about 25:1. A gap of less than 1 mm is however difficult to achieve reliably.

The magnitude of these effects was verified (for the gap) by scaling measurements of a real rubber sheet model. On the 1988 prototype and the production chambers the cathode structure is 6 mm wide strips spaced by 1 mm, the same mark:space ratio which Atac used<sup>6</sup>. A slight adjustment must be made to the strip potential in order to compensate for the systematic reduction in the actual drift field.

### **3.4 Consequences Of The Requirement For Total Ionisation Collection**

Adjacent to the front window, the electron drift trajectories must run parallel to the front window, and must then terminate on the sense wire; otherwise the X-rays which are absorbed in this region would not be detected. With the electrode strips mounted inside the gas volume, the finite strip width would have the effect of creating small dead regions, where the drift trajectories end on the strips. In order to avoid this loss of the localised ionisation from X-rays the electrode strips are positioned a short distance upstream on sectors of 5 mm thick rohacell foam. This structure in the field and its associated inefficiency then lies safely outside the active volume of the chamber and the electron trajectories do in general terminate on the sense wires (figure 3.4.1).

The upstream face of the chamber is then defined by the mylar gas window, which may become charged and induce unstable or unpredictable behaviour in the electron drift. However, provided the chosen chamber operating point has zero field wire charge, the ideal field everywhere along the window is parallel to its surface. Both the amount of charge attracted to the surface and the consequent change in electric field should in principle be negligible.

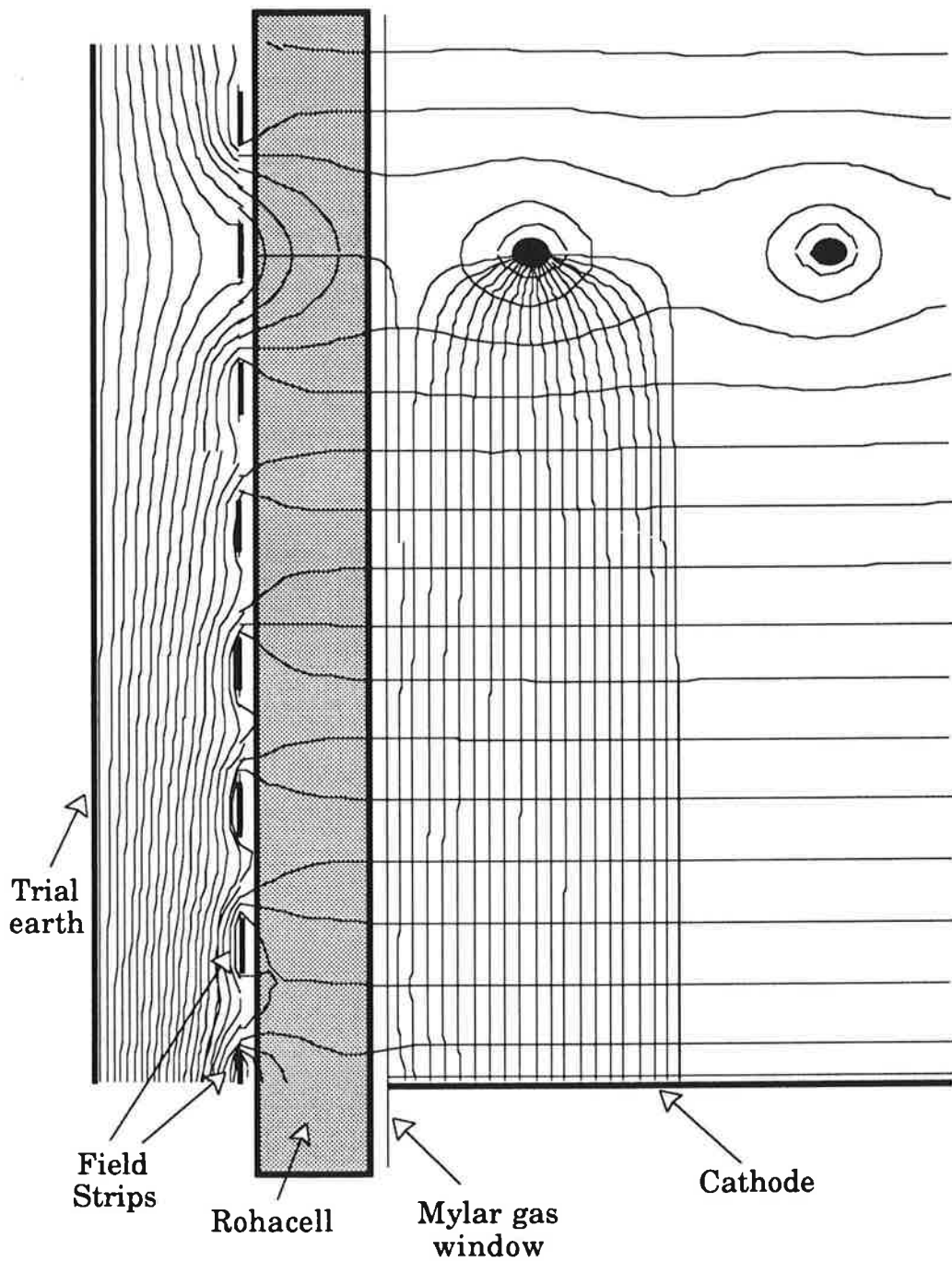


Figure 3.4.1 Simulation of electrostatic field in neighbourhood of front window<sup>7</sup>.



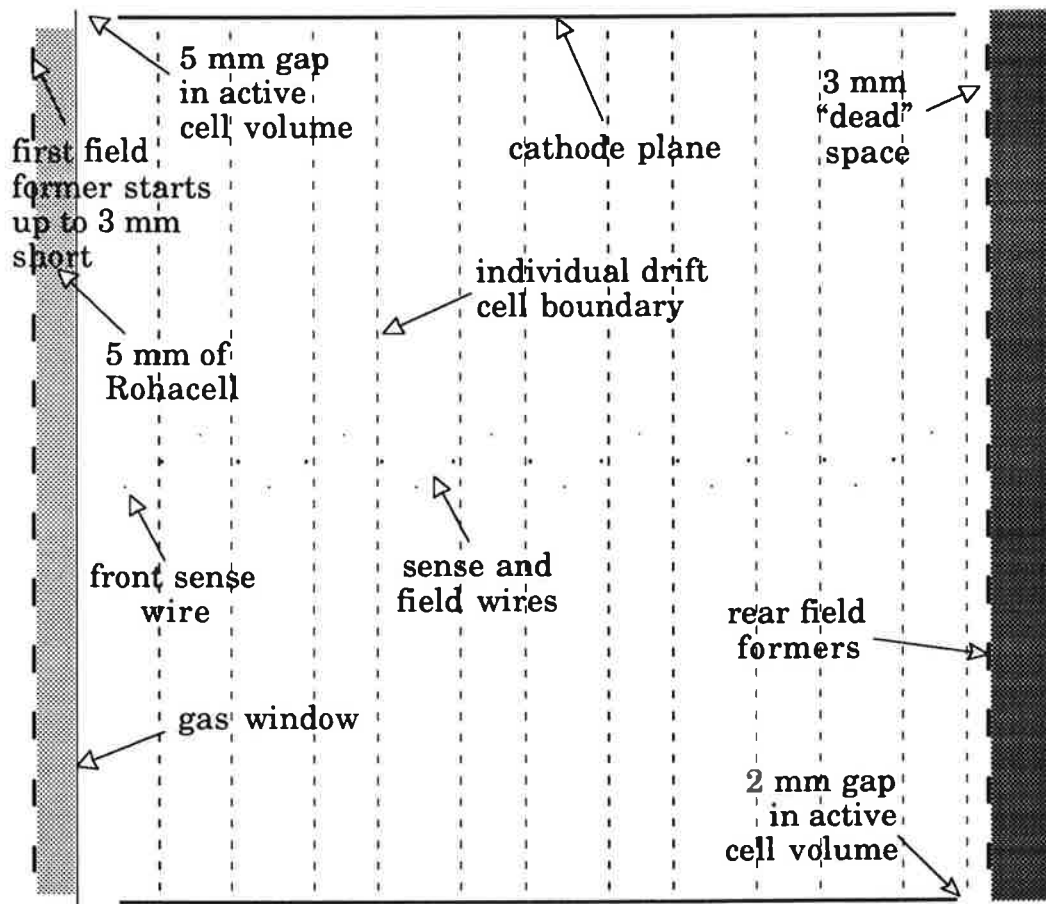


Figure 3.4.2 Sketch of cathode plane and field former arrangement

In practice, the cathode plane strips stop short of the front window; on the 1988 prototype and the full size chambers, the cathode electrodes stop up to 5 mm short of the edge, in order to minimise the risk of electrical breakdown between neighbouring cells when one cell is powered and the neighbouring cell has been switched off. Likewise the field forming electrodes at the front stop up to 3 mm short of the cell edge, and are spaced 5 mm upstream. These features are illustrated in figure 3.4.2. In general the chamber is also operated with some charge on the field wires. Empirically the potential on each electrode strip must be more negative than the naive extrapolation of the drift field potentials would have predicted. If the cell is operated symmetrically with non zero field wire charge then there should be a component normal to the dielectric sur-

face near the wire plane and some ionic charging of the mylar should result.

On the 1987 prototype, where the cathodes extended up to the front window, the front field forming electrodes were set 600 V more negative than the neighbouring drift field, for  $1.2 \text{ kV cm}^{-1}$  drift. Here the long term gas gain on the front wire was a factor two down when compared to the centre of the cell. The experience in test beam was that any charging effect had a time period of about five to ten minutes duration, during which time the gain on the front wire dropped by a factor of about 20%, and after which the chamber appeared stable. This corresponds with the findings of Allison *et al*<sup>8</sup>. On the 1988 prototype the electrode potentials were set to the same value as that of the extrapolated drift field. This voltage setting, combined with the fact that the cathode strips stopped short of the cell edge, meant that the front two wires in the chamber had inoperably low gas gain. The response at the front of the chamber was recovered on the full-scale prototype by increasing the applied voltages, such that next to the sense wire the electrode potential was 1 kV more negative than in the neighbouring drift region.

At the rear of the chamber the constraints are less severe, and some dead space may be tolerated. Therefore the field formers are mounted in the active chamber volume 3 mm back from the periodic drift cell boundary. The additional 3 mm of space also means that the shortened cathodes affect less of the rear-most cell (2 mm without cathode rather than 5 mm without cathode). There were no difficulties with the operation of this part of the chamber.

The field formers are also mounted on the inner face of the outer radius of the chamber, continuing up from the rear field formers. This main-

tains the correct electric field out to the maximum radius of the detector, resulting in the maximum possible active volume.

## 3.5 Conclusions

In spite of the complexities introduced by the unusual shape of the drift cell, the electrostatic behaviour of the radial wire drift chambers is very similar to previous detectors, and indeed the cell taper has caused no problems in operation on any of the prototypes.

The major complexity arises from the requirement for the active volume to start immediately inside the gas volume, with the ability to tolerate very little dead space in this region. The constraints on dead space are compounded by the requirement for fail safe operation of the full-size chambers, but nevertheless the proposed design does appear to satisfy both these constraints. Each cell is well insulated from its neighbours and also has maximum sensitivity to transition radiation.

Apart from an initial period of rapid ionic charging of the front window the response of the front section of the cell is sufficiently stable for acceptable performance. In figure 3.5.1 the gain corrected  $\frac{dE}{dx}$  distribution for the front wire is compared with one of the central wires. The broadening in response is seen to be minimal.

Finally in the above no explicit reference has been made to the proposed sense wire stagger. When this is included in the simulation, a 200  $\mu\text{m}$  stagger leads to a 12% “left/right” variation in effective path length for normal incidence tracks, which effect is visible in the test beam data. This effect is dealt with further in the chapter on energy loss measurements and particle identification.

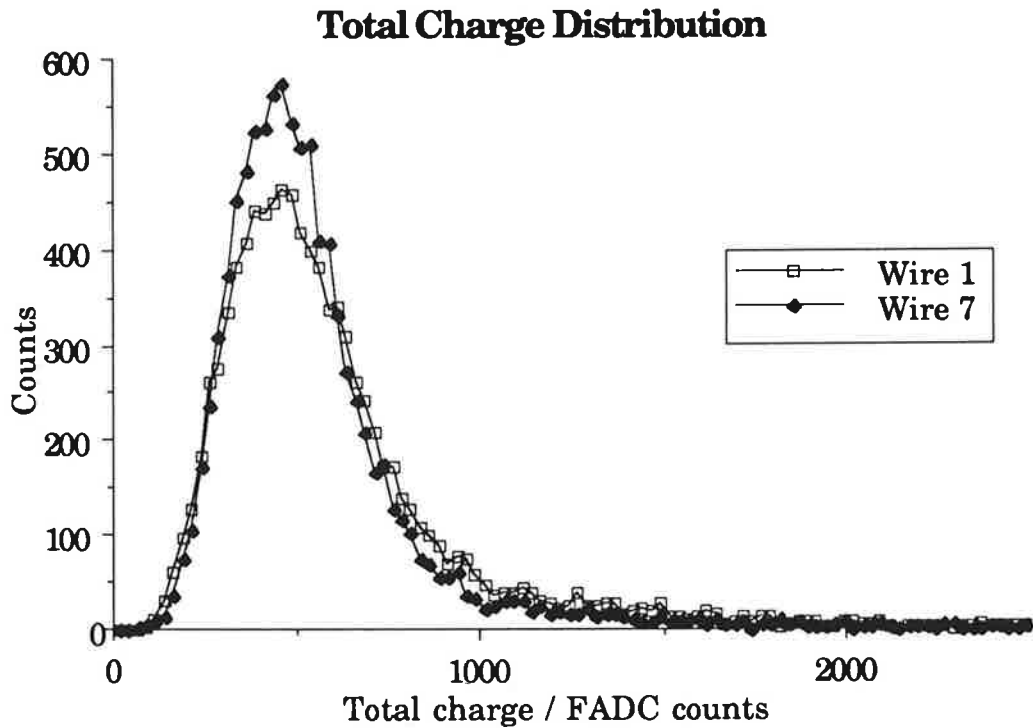


Figure 3.5.1 Comparison between the  $\frac{dE}{dx}$  distributions for wire 1 and wire 7.

- 
- 1 T Hessing and R W Kadel, Gas gain as a function of electric field, CDF Note No.176 (1983)
  - 2 for example G A Erskine NIM 105 (1972) 565, and the references therein
  - 3 Feynman Lectures Vol II, 12-6, Addison-Wesley (1964)
  - 4 for example the forward planar chambers and the CJC in H1, as detailed in the The Central Jet Chamber Of The H1 Detector At HERA, DESY, H1-TR 200 (1987) and The H1 Forward Tracker. Description And Status, DESY, H1-TR 205 (1987)
  - 5 G A Beck, Electrostatics of the Radial Wedge, (unpublished) 1987
  - 6 M Atac and T Hessing IEEE Trans. Nucl. Sci. NS-33 (1986) 189
  - 7 Figure courtesy of G A Beck

---

**8** J Allison *et al*, NIM 201 (1982) 341

# **Chapter 4:**

## **Description Of The Prototype Chambers**

### **4.1 Prototype 1: Initial Cosmic Ray Tests At Liverpool**

The first prototype single cell chamber was commissioned during the summer of 1986. This consisted of a wedge shaped cell with eight 25  $\mu\text{m}$  diameter Ni/Cr sense wires with additional field wires on either side of the cell, sketched in figures 4.1.1 and 4.1.2. The wires were 77 cm long although the active length was only 61 cm; this gave a typical sense wire resistance of 1510  $\Omega$ . The chamber electronics and data acquisition were very similar in the second prototype which was used for the majority of the test beam work. The track analysis techniques used on all of the prototypes were developed on the cosmic ray data taken with this first chamber. The only gas which was used in this chamber was bottled 90/10 Ar/CH<sub>4</sub>; this was used in an open circuit gas system, with slight over-pressure provided by a bubbler.

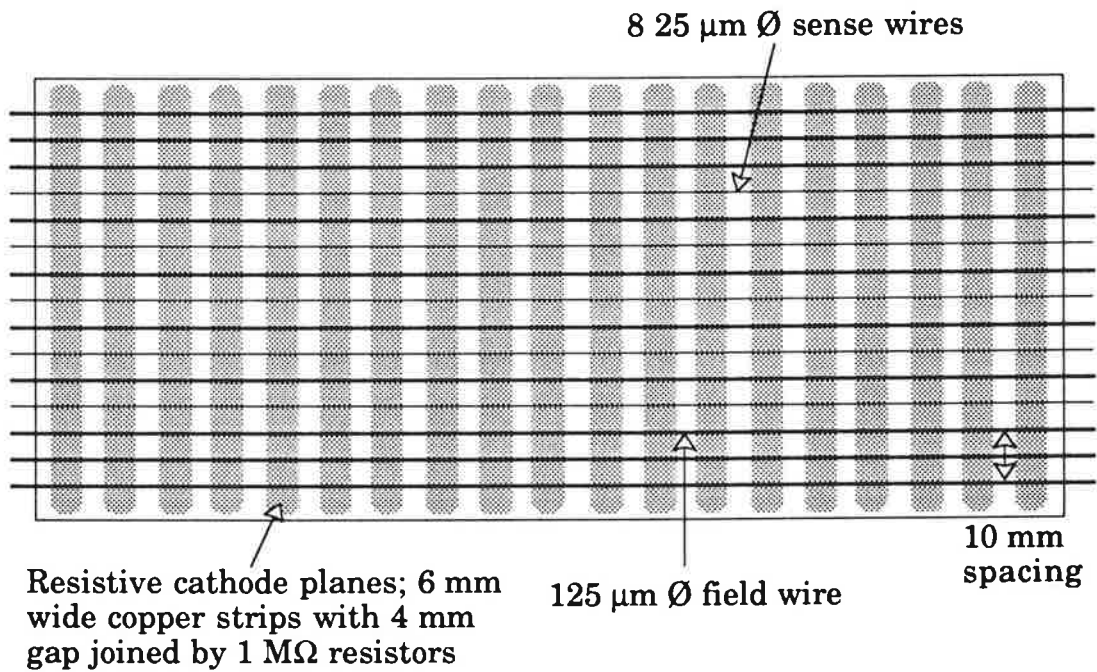


Figure 4.1.1 Side view of first prototype showing cathode structure.

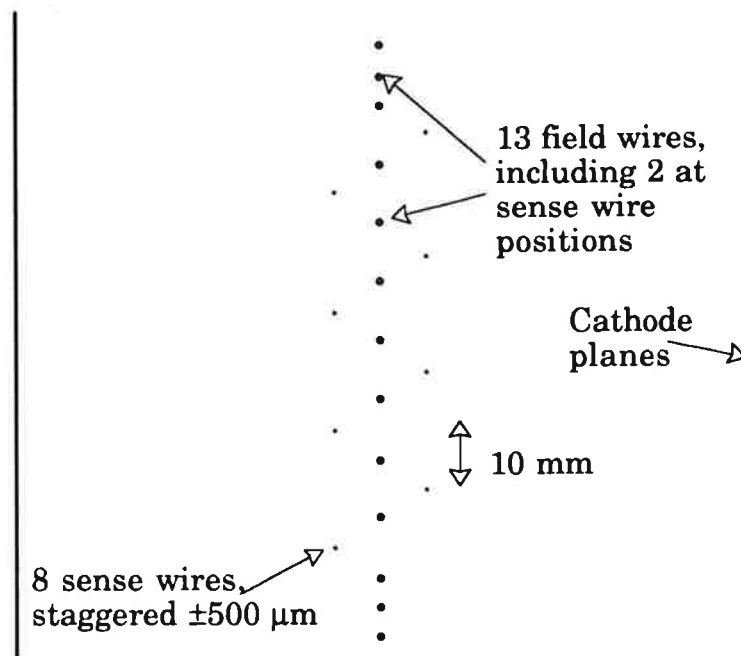


Figure 4.1.2 End view of first prototype.

## 4.2 Prototype 2

*The second prototype was christened "Bismarck" by person(s) unknown in the workshop. The graffiti on the side of the casing proved sufficient identification for the HM Customs and Excise*

*requirement of a serial number when the chamber was re-imported to the UK after completion of the test beam work.*

Building on experience with the first chamber, the second chamber was constructed to enable efficient X-ray detection. This was used for tests in one of the DESY electron test beams during the summer of 1987. The following investigations were planned:

- Performance with “standard” gas:
  - Space point precision for isolated tracks
  - Exploration of the required operating conditions, particularly with respect to results from simulations and the CDF group
  - Data with tracks at various well defined radial and drift distances, up to the maximum possible drift distance
  - Data with angled tracks including tracks crossing the wire plane
  - Two track resolution
  - Gain on outer wires, particularly evidence for dielectric charging
- Performance with “TRD” gas:
  - $e/\pi$  discrimination, for various xenon concentrations
  - Space point precision for isolated tracks

The major differences in the construction of this chamber and the first prototype were:

- 50  $\mu\text{m}$  diameter sense wire; Ni/Cr wire was used, with a specific resistance of  $5.3 \Omega \text{ cm}^{-1}$ .
- Field formers at front and rear of the chamber, instead of additional ‘guard’ wires. At the rear of the chamber these were cop-



per strips on fibre glass epoxy (G10), at the front these were aluminium strips on mylar.

- X-ray transparent front window made from 100  $\mu\text{m}$  thick mylar sheet, with a rohacell spacer for the front field formers.
- Flat front surface to chamber, allowing mounting of radiator to front, and active volume starting immediately inside the gas volume, with the first sense wire only 5 mm from the front window.
- Well defined gas flow down the wedge, as foreseen for the gas flow in the full size detectors.
- Use of final construction materials such as noryl and the kevlar nomex composite. The use of noryl feedthroughs for the wires permitted the use of operating voltages as detailed in chapter 3. The aluminium feedthroughs on the first prototype suffered electrical breakdown for sense wire voltages more than 1 kV. The electrodes were however still made from G10.
- Cell dimensions to match full-scale design, especially with regard to the depth of the chamber.
- Use of a computer controlled recirculating gas system, with very precise pressure control. With the mylar membrane forming the start of the active volume of the chamber, the detector could not withstand a pressure variation from atmospheric of more than about 50  $\mu\text{bar}$ .

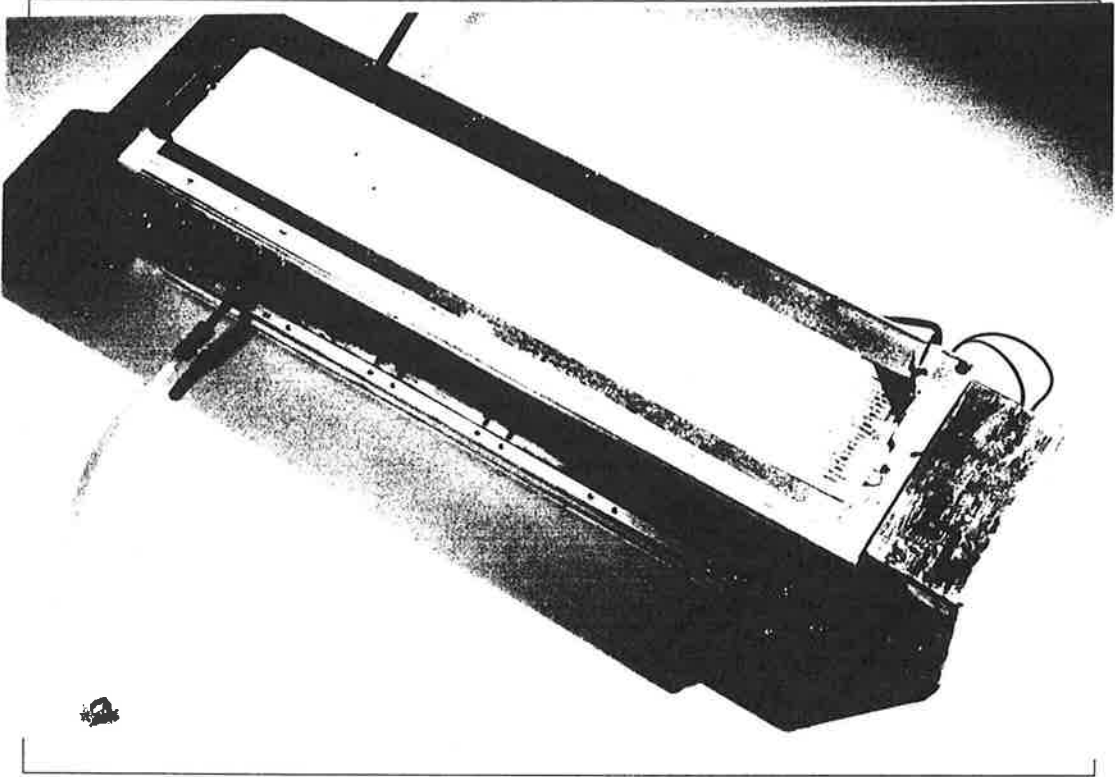


Figure 4.2.1 Photograph of chamber with front field formers *in situ*.

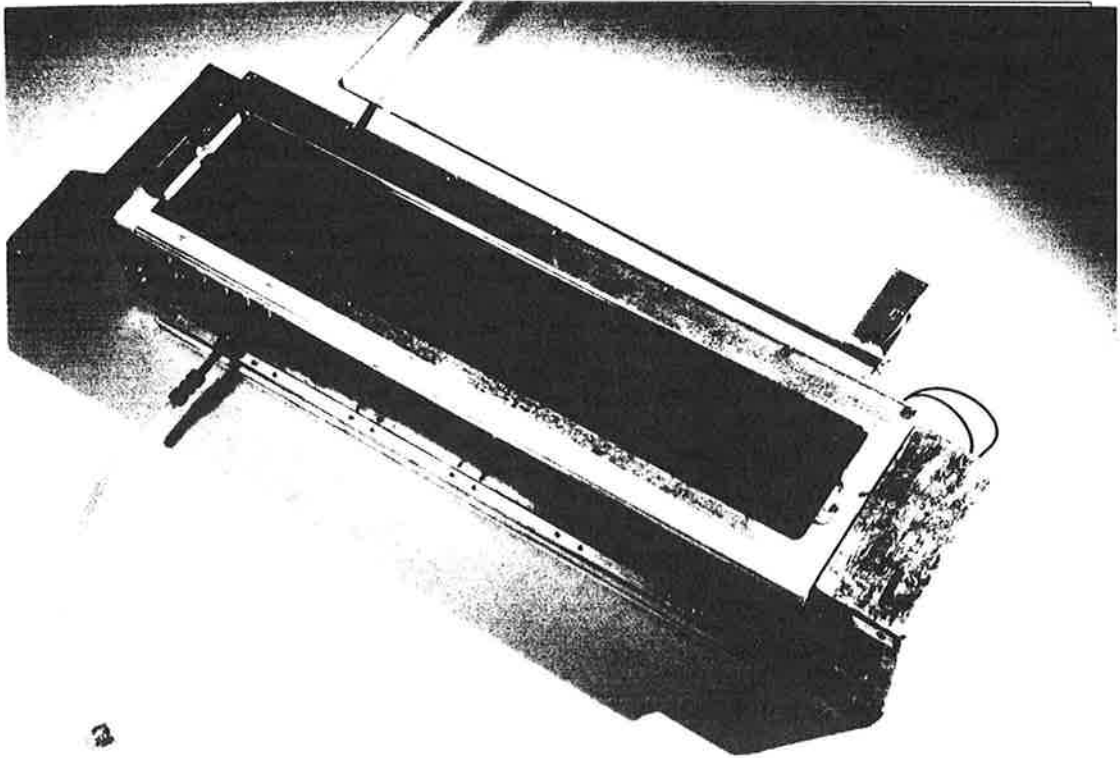


Figure 4.2.2 Photograph of chamber with front field formers removed.

The chamber is shown in figures 4.2.1 and 4.2.2, with and without the front field formers *in situ*. The electrical connections are sketched in figures 4.2.3 and 4.2.4. In all there were five different high voltage lines required which provided the ability to vary independently the overall gas gain, the electric drift field and the response of the front-most and rear-most sense wires. To reduce the possibility of earth loops, the chamber was insulated from the traversing table on which it was mounted, and was only earthed through the cathode supply labelled -EHV. The earth shields were broken near the chamber on all the other supplies.

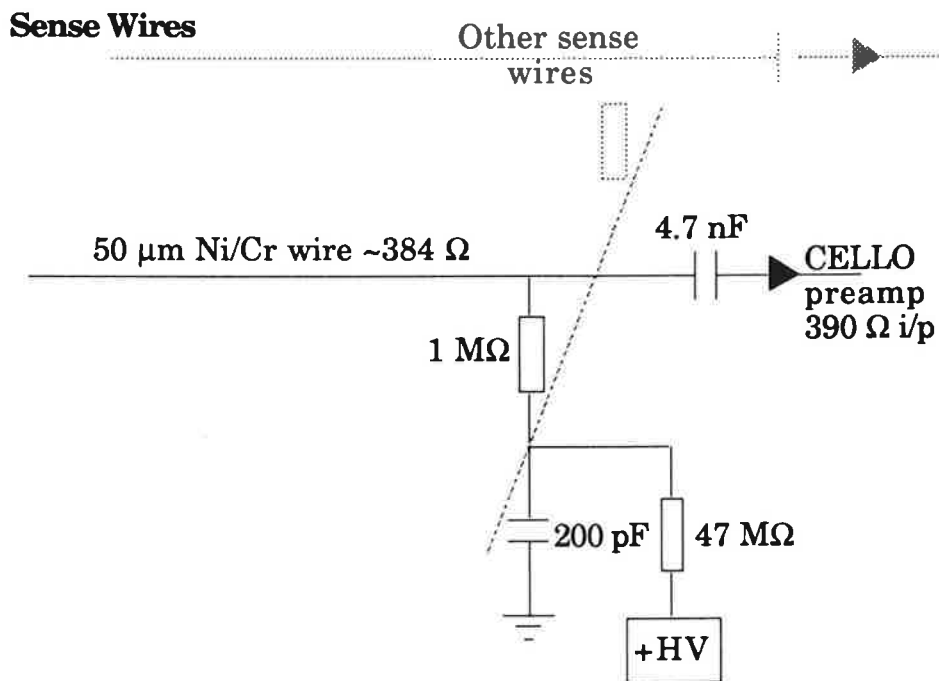


Figure 4.2.3 Electrical connections to the sense wires.

In the test beam data were taken with various gas mixtures, different electric fields, with and without transition radiator and at several beam energies. In all, just over 2 Gbyte of raw data were recorded to tape, corresponding to about 700,000 triggers. The read-out consisted of CELLO preamplifiers followed by double lengths of CELLO cables, digitised by DL300 FADCs which were read out via CAMAC into a PDP11 on-line computer, and thence logged to tape on the central DESY IBM via high

speed PADAC link<sup>1</sup>. The trigger was provided by two spatially separated 1 cm square finger scintillators in coincidence, down stream of the chamber.

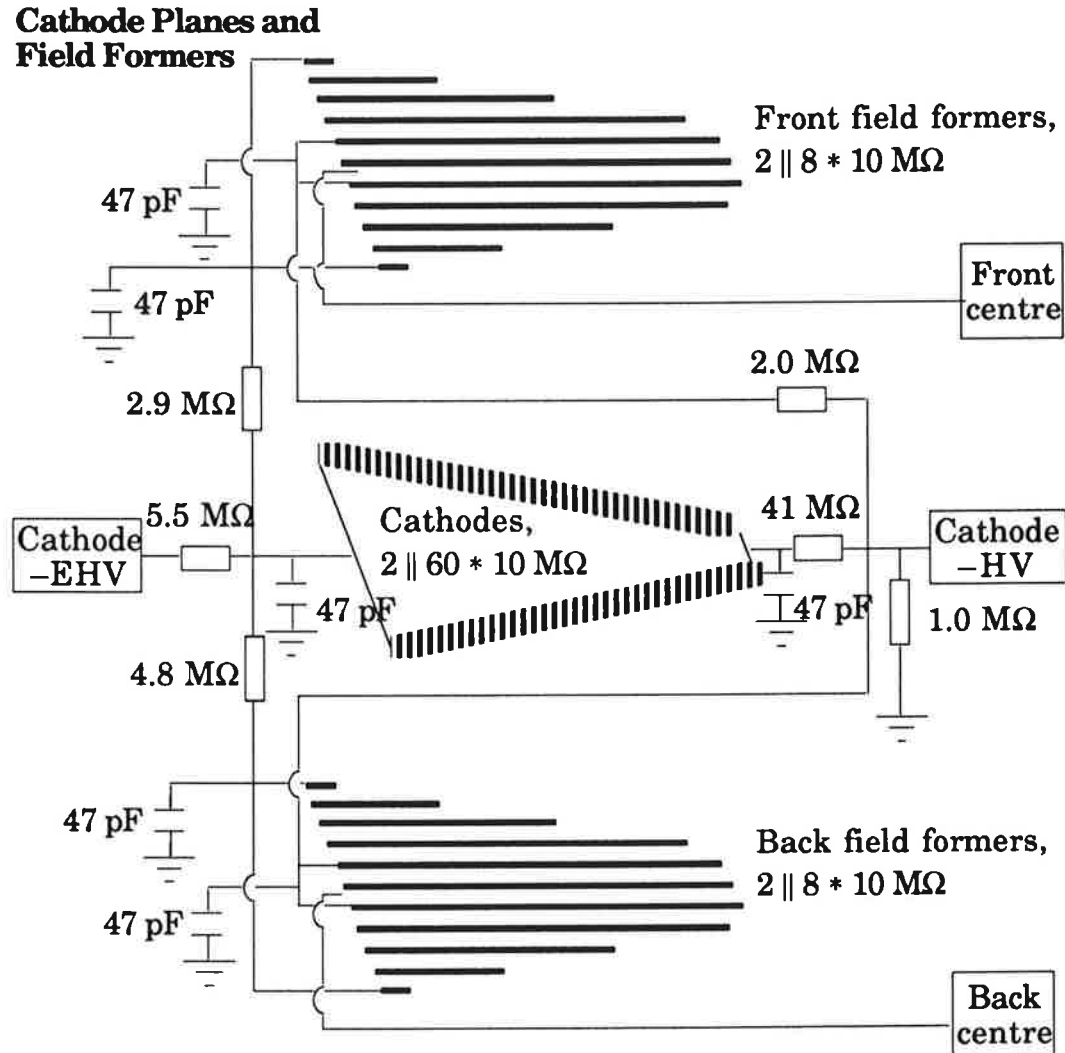


Figure 4.2.4 Electrical connections to the chamber.

The gas mixtures used were:

- HRS (Ar/CO<sub>2</sub>/CH<sub>4</sub> 90/10/1):

Systematic scan of the chamber at a nominal drift field of about 1.0 kV cm<sup>-1</sup>.

- Ar/C<sub>2</sub>H<sub>6</sub> 50/50:  
Extensive data with a ‘well known’ chamber gas, including some data with prototype 8 bit FADCs.
- Xe/He/CH<sub>4</sub>:  
Various TR favoured methane based mixtures. Xenon is chosen for its high X-ray absorption cross-section in the energy region of the TR photons, methane for its low mass and helium as a “filler” such that the resultant mixture had a density close to that of air. All exhibited a very slow drift velocity (although not as slow as Ar/CO<sub>2</sub> based gases), typically around 17 μm ns<sup>-1</sup>, and were therefore ruled out for use in H1.
- Xe/He/C<sub>2</sub>H<sub>6</sub>:  
Again various mixes, all of which showed a more rapid electronic drift velocity of about 30 μm ns<sup>-1</sup>, similar to that of the HRS gas.

### 4.3 Prototype 3

Whilst the second prototype established the feasibility of simultaneous TR detection and charged track space point reconstruction<sup>2</sup>, no tests had been performed in a magnetic field. Moreover the length of the chamber (84 cm externally) and the requirement of an axial magnetic field placed severe constraints on any suitable magnet; the only solenoid magnets available at DESY were compensation coils from the JADE experiment, which produced about 0.9 T at their maximum current of 5500 A. These however had an inner diameter of only 69 cm. It was therefore decided to construct a shortened test cell which could fit inside one of these compensation coils. This chamber was tested at DESY during November

1988. A copy of the design drawing for this chamber<sup>3</sup> may be found in the document pouch at the end of the thesis.

A three cell design was chosen so that the effect of having neighbouring cells could be investigated in test beam, including the analysis of tracks passing through the cathode plane between one cell and the next, as no test beam time was envisaged for the full-scale prototype. The effect of the hub connection on the charge division measurement could also be investigated for the outer wedge pair. The chosen section of the cell was truncated at the inner radius, so that the effects of the electrode structure at the outer radius as envisaged for the production chambers could be examined. This structure had not been present on either of the previous chambers.

The test cell design also included as many features from the final design as possible, including the paper epoxy electrodes, the polyester front field formers, Stablohm wire and the increased 300  $\mu\text{m}$  wire stagger. The chamber construction was completed using spare parts from the full-scale prototype, and where available, parts from the production chambers. The front Mylar window was 50  $\mu\text{m}$  thick, and tests were envisaged with the favoured polypropylene foil radiator, that had been constructed in the mean time, and which had not been available for the previous tests.

Data were taken using DL3000 FADCs, all with Ar/C<sub>2</sub>H<sub>6</sub> 50/50 on a recirculating gas system, for various magnetic fields up to 0.9 T, scanning the chamber from end to end, including the outer corners of the cell expected to be most affected by the revised electrode structure.

- 
- 1** Data acquisition program provided by G Franke, DESY
  - 2** H Gräßler *et al*, NIM A283 (1989) 626
  - 3** University of Liverpool Department of Physics drawing number NP25 A0001/95

# Chapter 5: FADC Analysis And Hit Detection

## 5.1 Introduction

The use of FADC read-out to record the time development of the drift chamber pulses, as in figure 5.1.1, ensures significantly improved multi-hit resolution compared to more conventional electronics, with a two-track resolution of around 2 mm being readily achievable; in addition accurate timing is facilitated, with the radial chambers achieving  $\sim 150 \mu\text{m}$  point precision. The pulse shape information also permits the determination of the charge integral for each pulse. This is exploited in the charge division measurements, giving true space-points, as well as in the X-ray detection and  $\frac{dE}{dx}$  measurements.

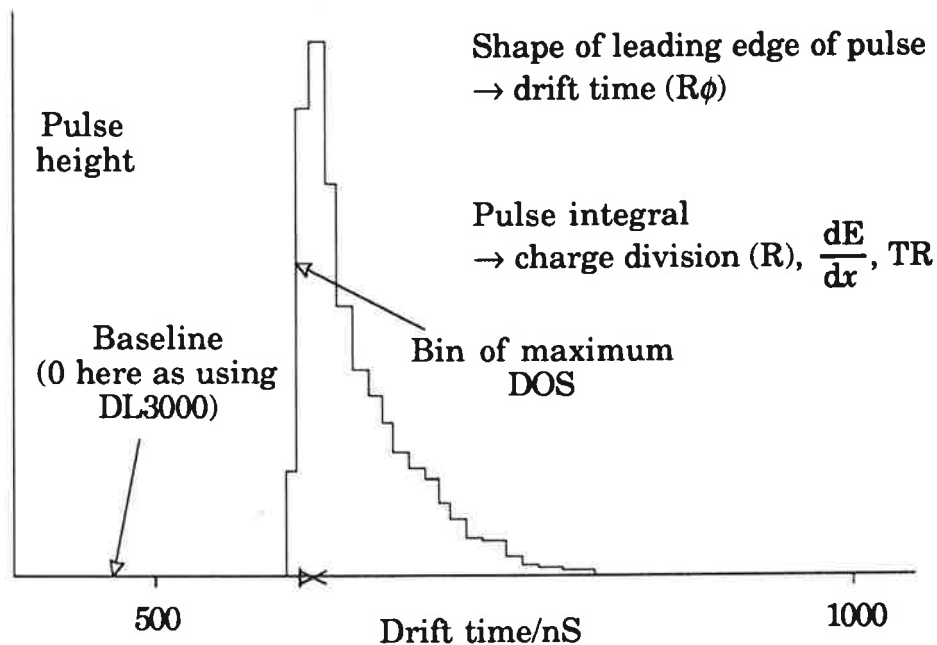


Figure 5.1.1 A typical pulse after re-linearisation.



The benefits of recording the pulse shape outlined above outweigh the drawbacks of using FADCs, the most severe of which is the huge quantity of raw data generated. At 100 MHz one FADC channel would take only 10  $\mu$ s to produce a kilobyte of raw data, and in the course of test beam work at DESY it transpired that a complete event for the two fully instrumented wedges of the prototype amounted to 12 kilobyte of packed raw data. It is therefore essential to perform some form of “zero suppression” as early as possible in the read-out chain. Three different solutions have been adopted:

- “Real time sparsification” of the digitised signal<sup>1</sup>, as used in the D0 central tracking chambers<sup>2</sup>. Here the FADC writes to 100 MHz buffer memory, which is simultaneously scanned for any pulses. Once a pulse is found the zero suppressed data is then copied to slower memory, whilst the FADCs continue to run. On initiation of the read-out, all that needs to be done is to read out the zero suppressed pulses. The cost of having a custom 100 MHz scanner chip is offset against the reduced amount of fast memory required.
- Having a dedicated digital signal processor (DSP) on each FADC card, ensuring rapid zero suppression as a result of the high degree of parallelism and the direct DSP access to the FADC memory without using the crate bus. This technique is used in the Aachen FADCs for the L3 experiment at CERN, the CDF experiment at Fermilab, and the ZEUS experiment at HERA<sup>3</sup>. The increased cost of additional electronics is offset by the reduced load on each DSP, allowing for the possibility of extensive on-line pre-processing, such as implementing a digital filter<sup>4</sup>.

- Implementing a fast scan with a single scanner for each crate of FADCs, using a special crate bus to ensure sufficiently fast read-out rates. This is the technique employed in the Heidelberg / Struck DL300 system<sup>5</sup>, where the FADCs are housed in a special crate with a 100 MHz back-plane; the back-plane is also used to fan out a global clock for the FADCs. An identical system is used for both the DESY / Struck DL3000 and the DESY / Struck F1000, in spite of the different crate size. In the latter, although the FADC memory can be directly accessed via “standard” VME, a special back-plane is used by the scanner to achieve the necessary read-out speed.

## 5.2 FADC Systems Used In The Radial Chamber Tests.

For all the data taken, the entire FADC memory was written to disk or tape. All data were taken with the FADCs operating in common start mode, relying on the propagation delay along the signal cables to allow a faster trigger signal to start the FADCs. The arrangement is sketched in figure 5.2.1 for the cosmic ray tests with the first prototype. A fast coincidence between the scintillators started the FADCs before the sense wire signal had traveled the length of the CELLO signal cables. To simulate the effect of the long distance between the H1 experiment and the electronics hut, all the DESY test beam data were taken using double lengths of CELLO cable.

Most of the test data, and all the data with TR radiators, were taken using DL300 FADCs. These FADCs are based on a 6 bit 100 MHz FADC chip, stretched to an effective 8 bits at low signal levels by using a ‘golden hyperbola’ non-linear input stage<sup>6</sup>. This is illustrated in figure 5.2.2.

With this non-linear response, the sensitivity varies between  $0.8 \text{ mV LSB}^{-1}$  and  $12 \text{ mV LSB}^{-1}$ , with electronic noise below 1 least significant bit (LSB). The effect of the non-linear response function is that 1 LSB is generally about 6% of the input pulse height. Each DL305 card has 4 FADCs, each with a 256 byte depth of memory. This corresponds to a maximum drift time of  $2.56 \mu\text{s}$  when operated at 100 MHz.

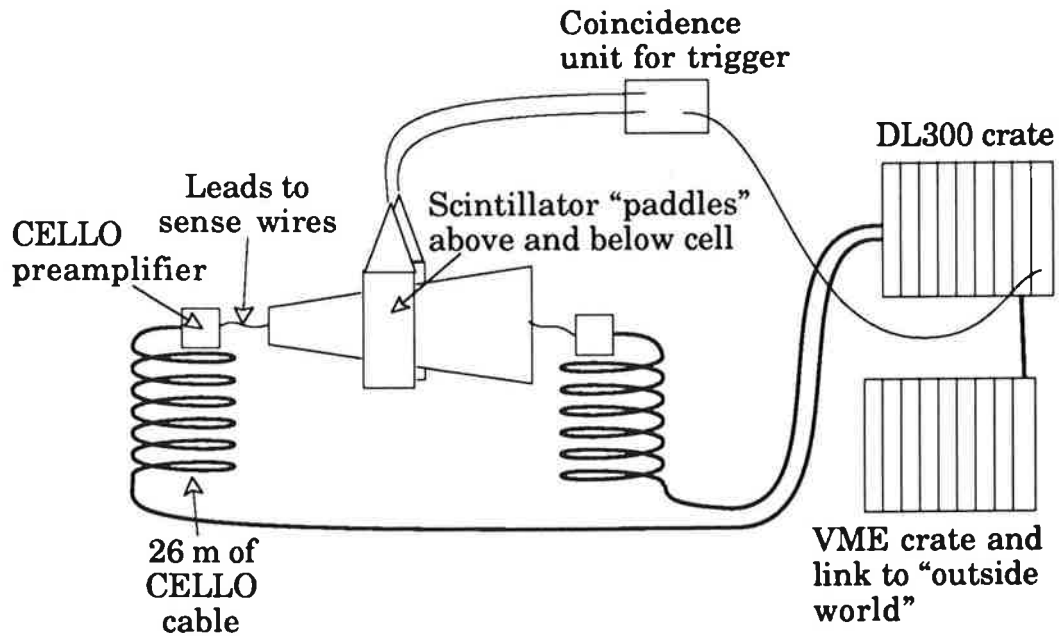


Figure 5.2.1 Schematic of chamber read-out for first prototype.

Generically similar to the DL300s are the DESY / Struck DL3000s, which were used in the 1988 tests. These are 'plug compatible' with the DL305s, although the card size is much deeper. They are based on 8 bit 100 MHz FADC chips<sup>7</sup>, now with 8 FADC chips per card, but still the same depth of memory for each FADC. Again a non-linear response function is implemented, giving a sensitivity varying between  $2 \text{ mV LSB}^{-1}$  for small signals (effectively 10 bit precision) and  $32 \text{ mV LSB}^{-1}$  at the maximum 2V input (6 bit precision).

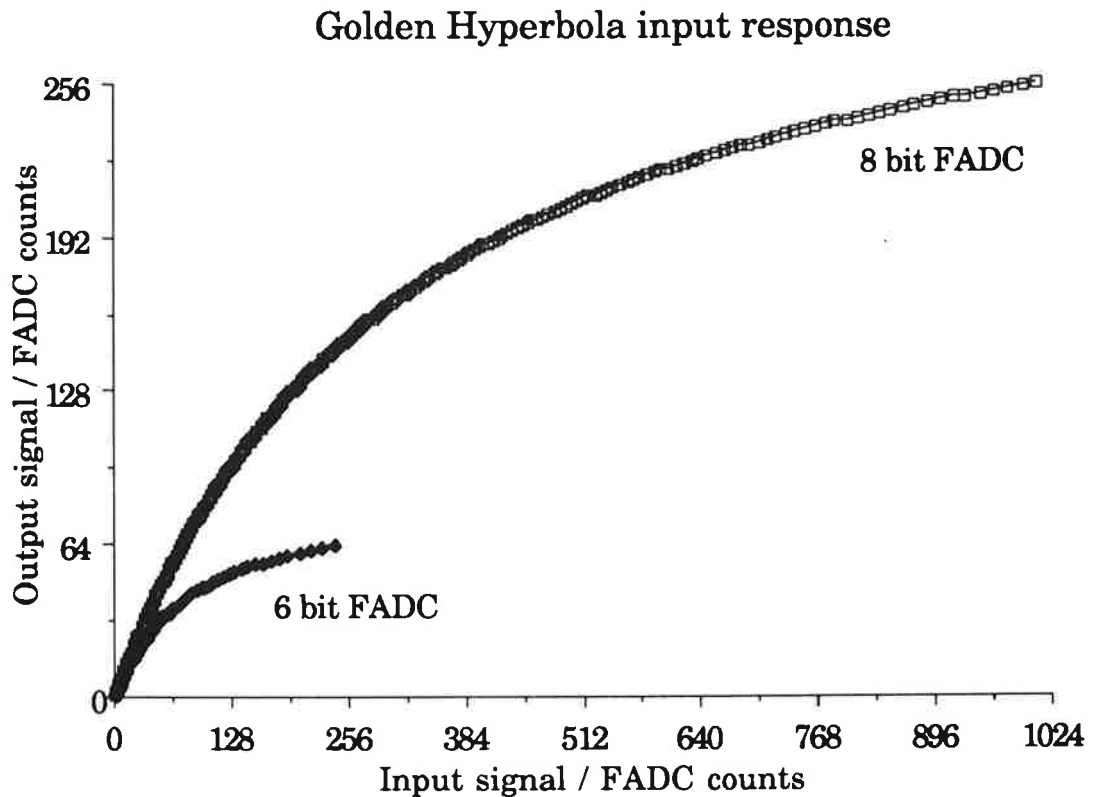


Figure 5.2.2 Non-linear response function.

The F1000s that will actually be used in the H1 experiment use the same SONY FADC chips as the DL3000. The implementation is different, with the back-plane being VME based, and a still larger board size, allowing 16 FADC chips on each card, but their response should be very similar to the DL3000s.

### 5.2.1 Properties Of The Preamplifiers Used

CELLO preamplifiers were used for the original cosmic ray tests and for the 1987 test beam work. These have a rise time of 10 ns, well matched to the 10 ns binning of the FADCs. For the 1988 tests prototypes of the eventual H1 preamplifiers were adopted. This design incorporates the sense wire high voltage distribution into the front section of the card, with the amplifier stage being a higher gain integrated circuit development of the CELLO design. These have a sensitivity of  $100 \text{ mV } \mu\text{A}^{-1}$ , with an input

impedance of  $200 \Omega$ ; the output load is  $2 \times 50 \Omega$ , with a maximum output amplitude of  $\pm 2.5 \text{ V}$  bipolar. The resulting electronic cross-talk is better than  $0.5\%$ , with a linearity of better than  $0.1\%$ , and output noise below  $5 \text{ mV}$ .

The disadvantage of using such a high gain preamplifier mounted on the chamber is the high power consumption,  $170 \text{ mW}$  per channel, on the actual detector. In H1 extensive measures are being taken in order to provide sufficient cooling on the detector.

### **5.3 Zero Suppression And Base Line Determination**

The zero suppression referred to above will be effected by a special hardware processor in the F1000 system, the F1020 scanner. This will rapidly transfer the entire FADC memory into its own internal buffer and simultaneously produce a set of pointers to regions containing non-zero data (hit detection). This will enable the FADCs to restart running within  $0.8 \text{ ms}$ .

The pointers and hit data in the scanner will then be read out by the front end processor (FEP). This information may be analysed to give a drift time and pulse integral for each hit, which will then be passed on to the later stages of the data acquisition (DAQ). It will be possible to have an event undergoing analysis in the FEPs and a scanned event waiting in the scanner buffer, whilst the FADCs continue running; this will give a degree of pipe-lining in the front end DAQ, necessary for a HERA experiment where it will be possible for events to be separated by only the read-out time of around  $0.8 \text{ ms}$ .

In all the test beam work either DL300s or DL3000s were used. Although there is a scanner module within the DL300 system no use was made of the FASTSCAN provided by it. Instead the entire contents of the FADC memory was written to tape. In order to speed up the later data analysis, a software 'scanner' was implemented which not only mimicked the action of the F1020 scanner, but also evaluated a background level before the first pulse on each wire.

The background evaluation is necessary for the DL300, where the input signal is DC coupled to the FADC. This DC coupling causes the pulses to sit on a non-zero pedestal. The DL3000 and F1000 on the other hand have the input signal inductively de-coupled from the FADC. With the DL3000 the base line is forced to be zero, as in figure 5.1.1. The F1000 has the base line offset, in spite of the AC coupling, in order to reduce the risk of any negative excursions in the pulse shape; effects of this nature arise from cross-talk. The response of the DL300 in particular to such an excursion was exceptionally poor, resulting in a totally unanalysable pulse.

With the DL300 data this background level was evaluated on an event by event basis, as it was not observed to be particularly constant. It is especially important to identify correctly the base line when attempting any second coordinate determination by charge division, as the systematic errors induced by using an invalid base line, whilst at least being monotonic, are unfortunately far from linear.

## 5.4 Overflows, Re-linearisation And Cross-talk Compensation

One unfortunate aspect of the DL300 FADC is that it sets overflows to zero. However, the effect within a pulse is easily recognisable, as illustrated in figure 5.4.1, and the following recovery technique was adopted: if at most ten consecutive time bins were zero and the two immediately adjacent bins were at least seven counts greater than background in the non-linear data, then the zero bins were assumed to have overflowed. This may be corrected by setting the relevant bins to the minimum value that would cause overflow, namely 64, which corresponds to a value 256 on the linear scale. The pulses were then included in any following analysis. With the 8 bit FADCs this problem does not occur, as they instead stick at 255; however, pulses this large suffer from obvious distortion.

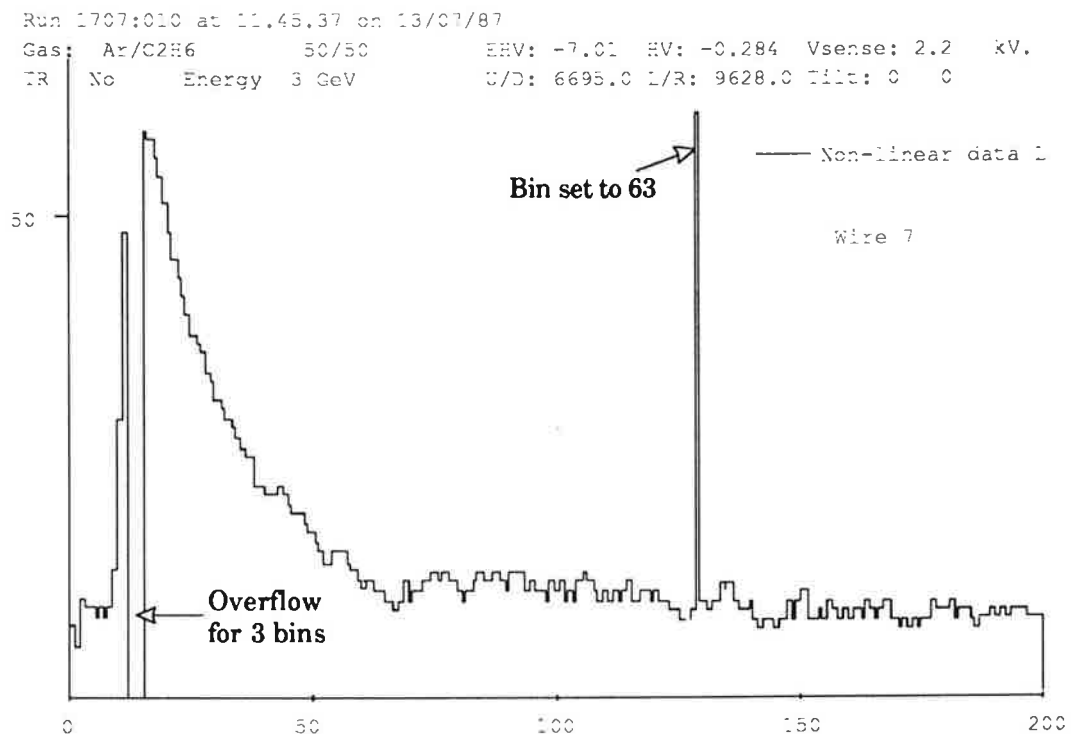


Figure 5.4.1 Example of pulse that has overflowed the FADC.

The use of a non-linear input with all the FADCs requires that the raw data must first be re-linearised before attempting any pulse analysis. The effect of this re-linearisation is illustrated in figure 5.4.2. Moreover with the chosen wire geometry there is cross-talk between neighbouring sense wires at the level of 7%. This effect is readily compensated, either by using a cross-talk filter after the preamplifier, as in the OPAL jet chamber<sup>8</sup>, or in software, by adding on a fraction of the neighbouring wire's read-out, on a bin by bin basis, when this information is available. The effect of this compensation is illustrated in figure 5.4.3, where the uncorrected and corrected neighbouring wire signals are displayed for an isolated pulse. In general the analysed charge and drift time are all that will be available, so that the final correction must be based on these.

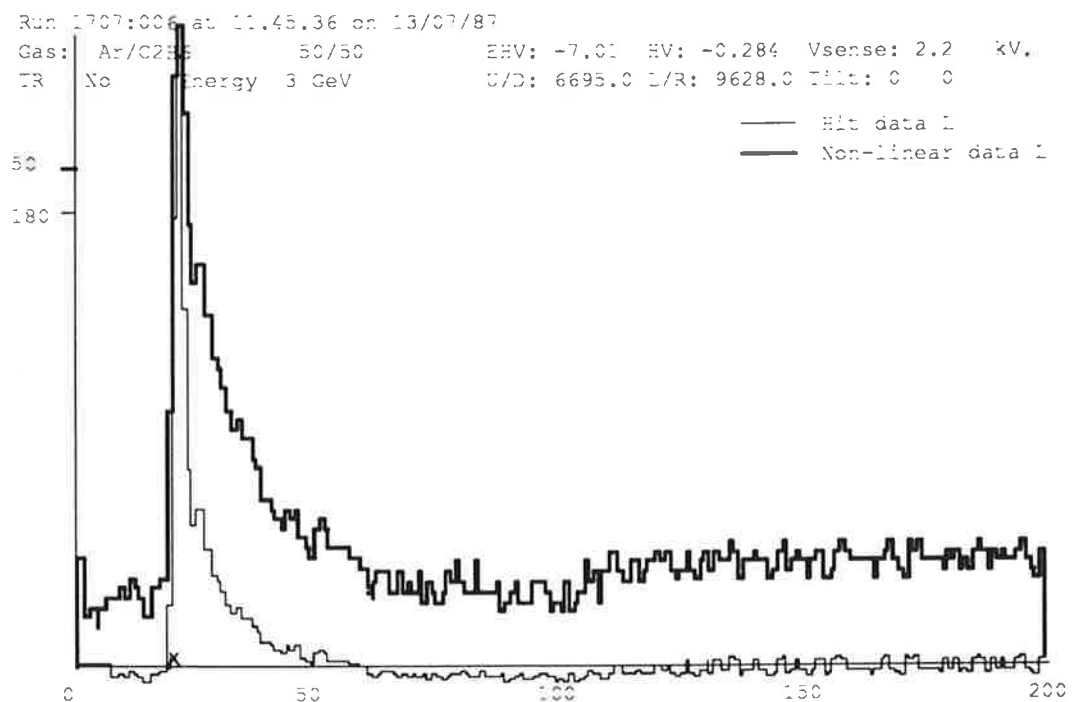


Figure 5.4.2 Comparison between raw and re-linearised data.



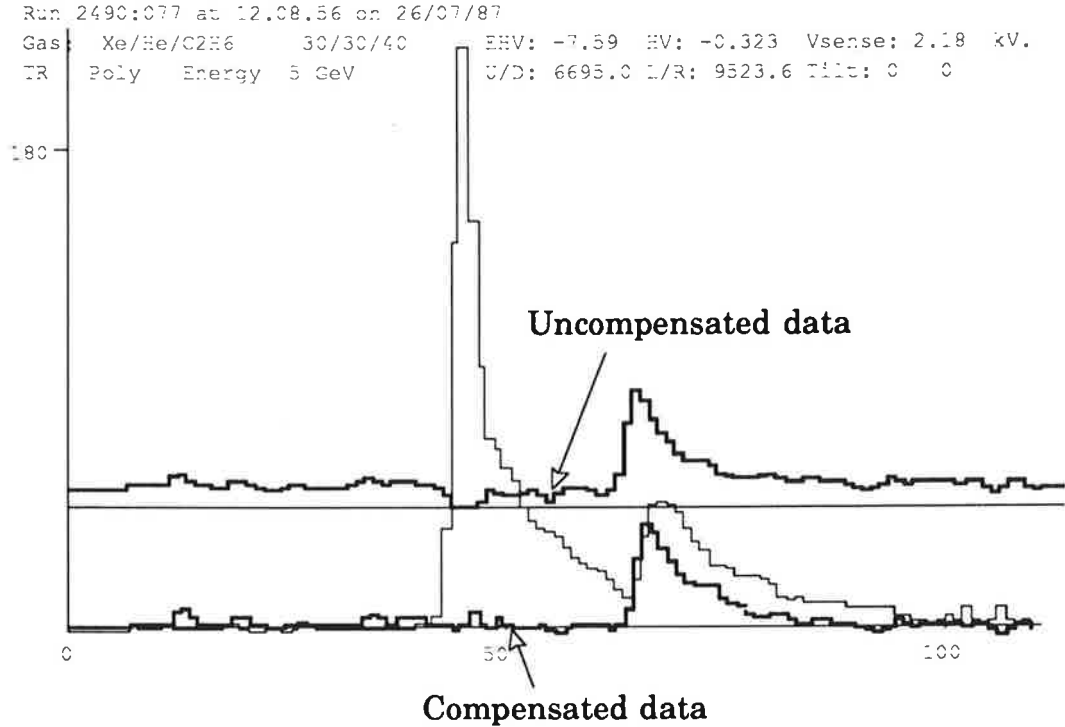


Figure 5.4.3 Comparison between cross-talk compensated and uncompensated data.

## 5.5 Hit Finding

After re-linearisation and cross-talk compensation of the regions flagged by the 'scanner', a second more sophisticated software hit-finding algorithm was implemented. This was initially developed on the original Liverpool cosmic ray data, in order to provide a very powerful discrimination between signal and noise. Conventional techniques, such as the simple threshold cut employed by the scanner, or derivatives thereof, such as a threshold cut in the difference of samples (DOS, defined as  $d_j = a_j - a_{j-1}$ , where  $a_j$  is the re-linearised data for time slice  $j$ )<sup>9</sup>, do not cope very well with a non-uniform background.

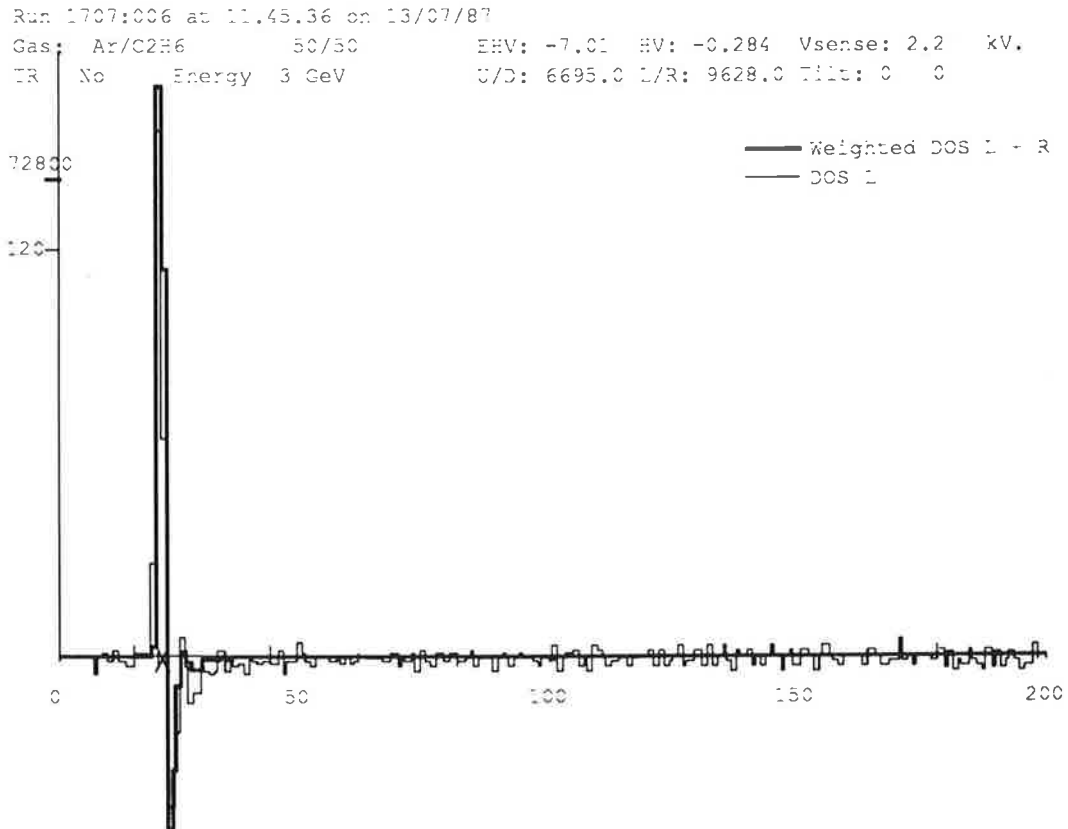


Figure 5.5.1 Comparison of the DOS and weighted DOS data.

Given the ability to define some form of pedestal, it is possible to construct the product of the difference of samples, and the absolute height from this pedestal,  $s_j = d_j \times a_j$ . This forms a signal which is relatively insensitive to an oscillating or gently rising baseline, and which provides a very strong signal for any pulse. This is shown in figure 5.5.1, along with the DOS data, for the same pulse as in figure 5.4.2. For a pulse this size sitting on this level of noise, there is a difference of about 2 orders of magnitude in the signal to noise ratio between the weighted DOS and the conventional DOS. This signal is, moreover, extremely sensitive to any secondary pulses that may be behind the initial detected pulse. In essence this algorithm searches for rising edges that continue to rise, a characteristic of any chamber pulse, but not in general a characteristic of noise.

By applying a threshold cut in this weighted difference of samples, calculated using the sum of the left and right hand read-outs, a set of pointers to regions containing potential hits may be constructed. These are then passed on to the timing algorithms and the pattern recognition.

### 5.5.1 Chamber Efficiency

Shown in figure 5.5.2 is the distribution of hits which were included in a reconstructed track versus drift time obtained for a scan of 4 runs with the 1988 prototype where the nominal beam spot moved from 1 cm from the wire plane to 4.7 cm from the wire plane. The reconstructed beam spot distribution typically had a standard deviation of 12 FADC bins, corresponding to the 1 cm square scintillators used to form the trigger, resulting in the individual run positions not being resolved. In the gas used, Ar/C<sub>2</sub>H<sub>6</sub> 50/50, this corresponds to a maximum drift time of about 90 FADC bins, and a beam spot standard deviation of about 6 mm.

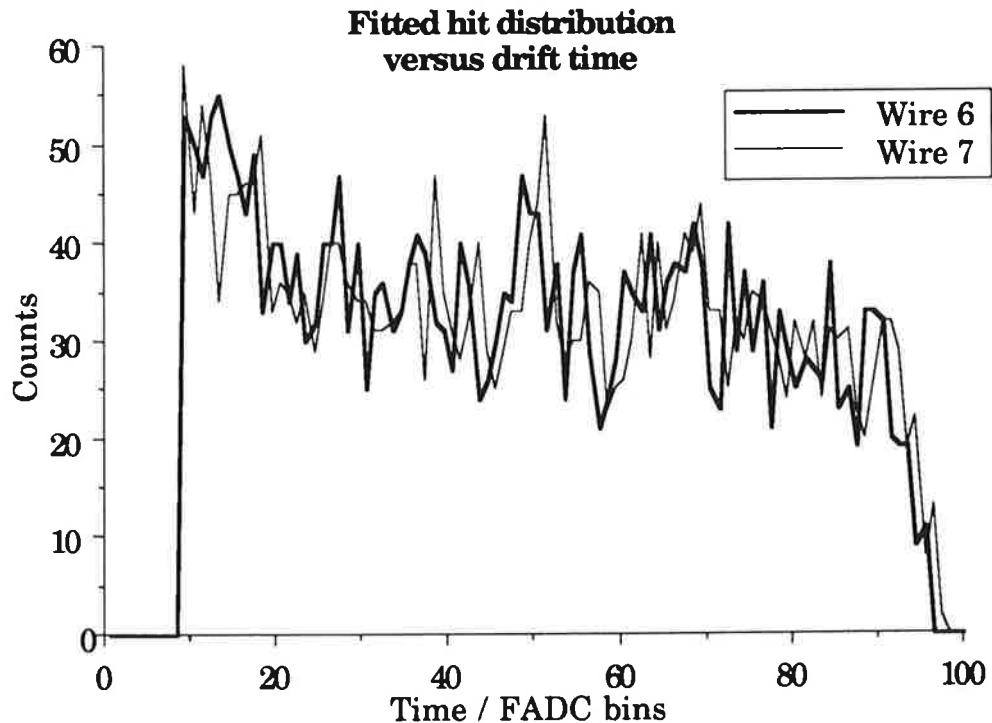


Figure 5.5.2 Hit distribution versus drift time.

The results from an efficiency calculation performed by checking for a detected hit within a time window defined by the reconstructed track road unfortunately are biased by the poor performance on the front wires of the chamber. For the remainder the efficiency remains above 99%. An absolute efficiency is moreover impossible to calculate from the data taken because of the ill defined beam spot.

## 5.5.2 Two Track Resolution

Shown in figure 5.5.3 is an event from a run where a 2 cm block of steel was placed immediately after the final collimator, and the FADC trigger was formed by a coincidence between two crossed finger scintillators and a paddle scintillator which had a 1 cm hole aligned with the spot defined by the finger scintillators. This was intended to trigger on a track with secondaries.

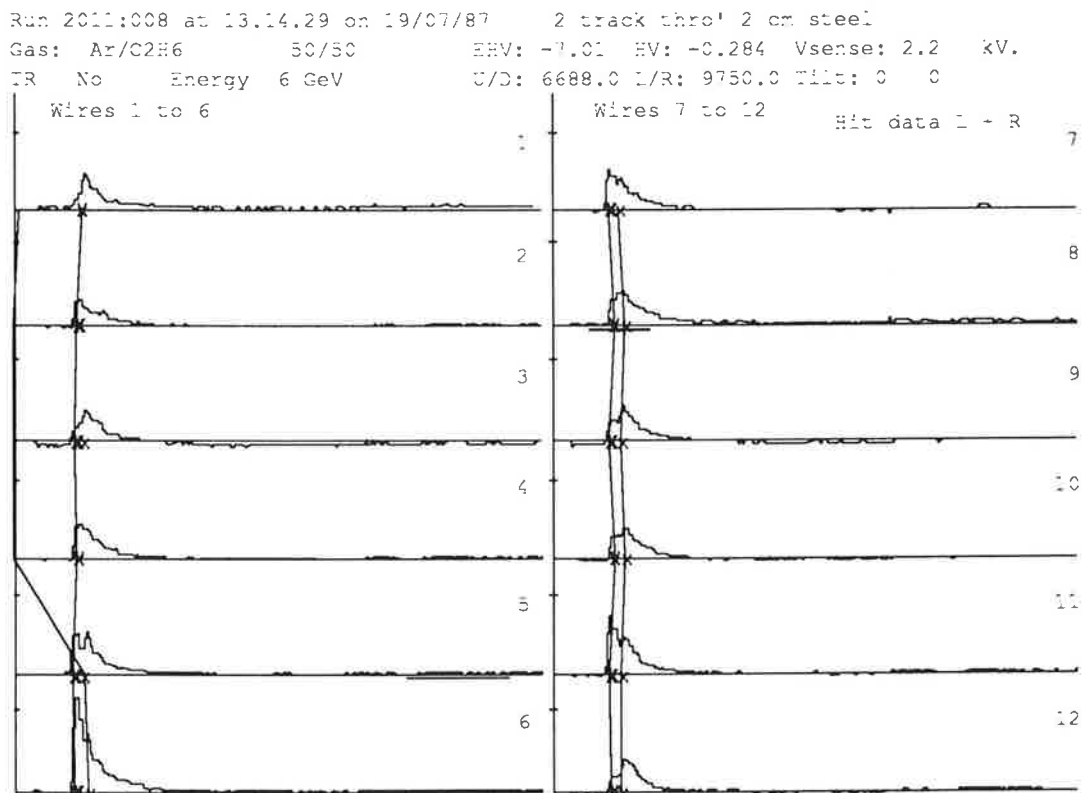


Figure 5.5.3 A two track event

The data are arranged with wires 1 to 6 in the left hand column and wires 7 to 12 in the right hand column. The detected hits are indicated by "x"s and "+"s, with the reconstructed tracks shown by the staggered lines through these points. On wires 1, 2 and 4 the two hits were not resolved, whereas on wire 3 the resolved hit was not recognised by the pattern recognition. Figure 5.5.4 is an exploded view of wires 5 and 6, and in figures 5.5.5 and 5.5.6 are the similar displays for the weighted DOS and ordinary DOS data for these two wires.

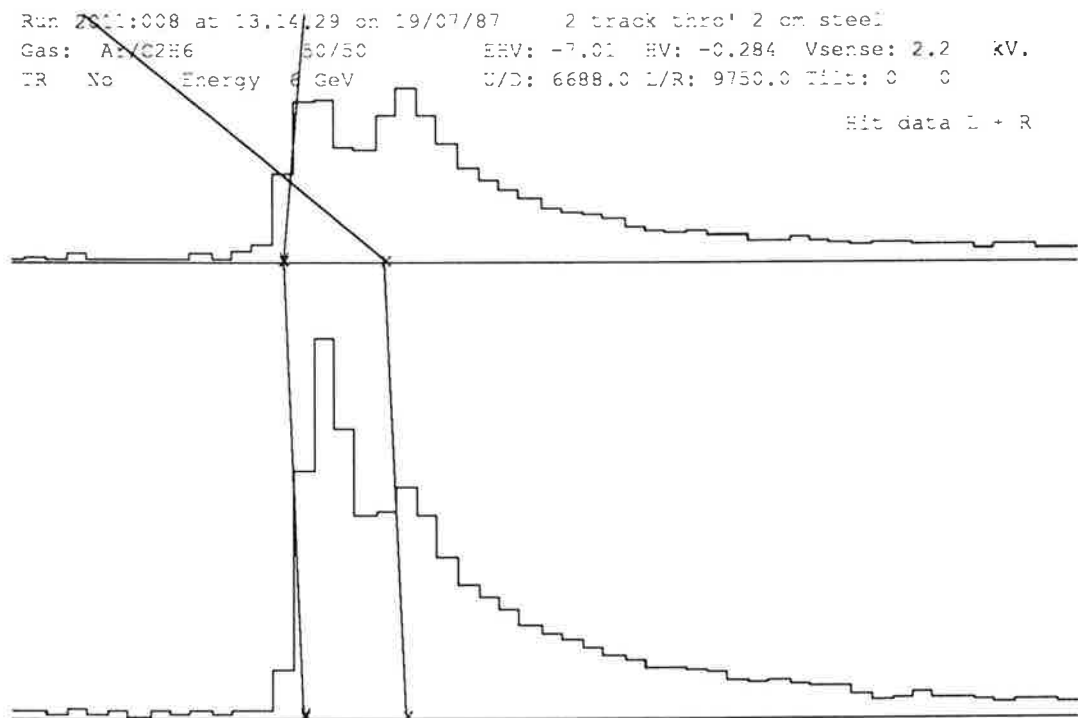
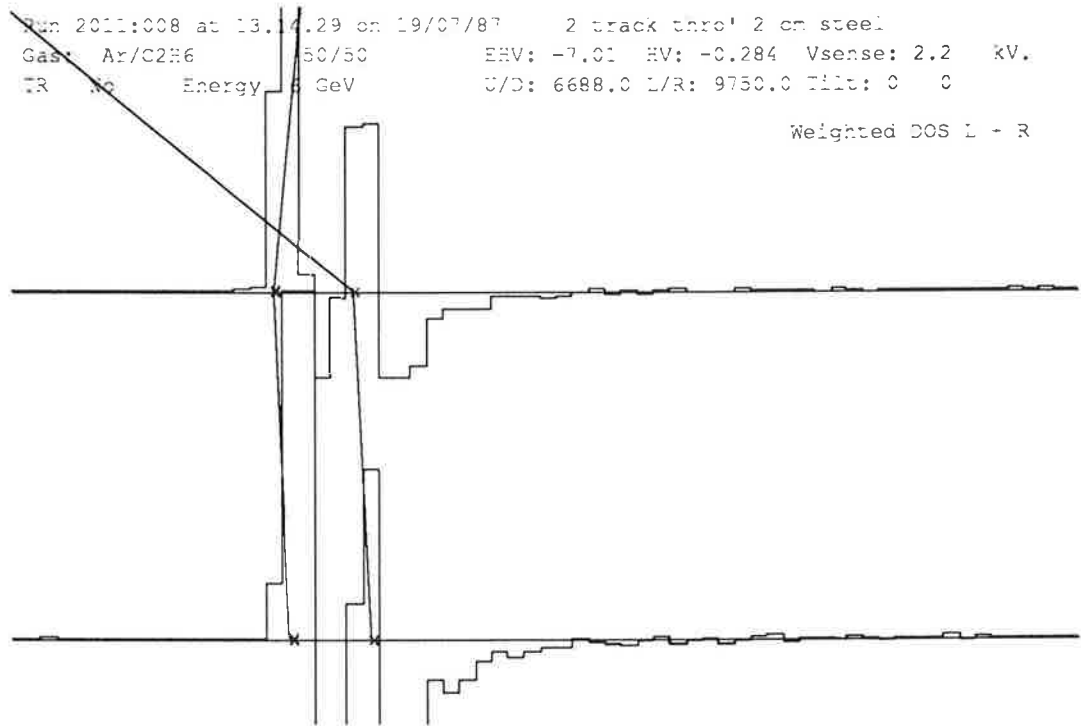
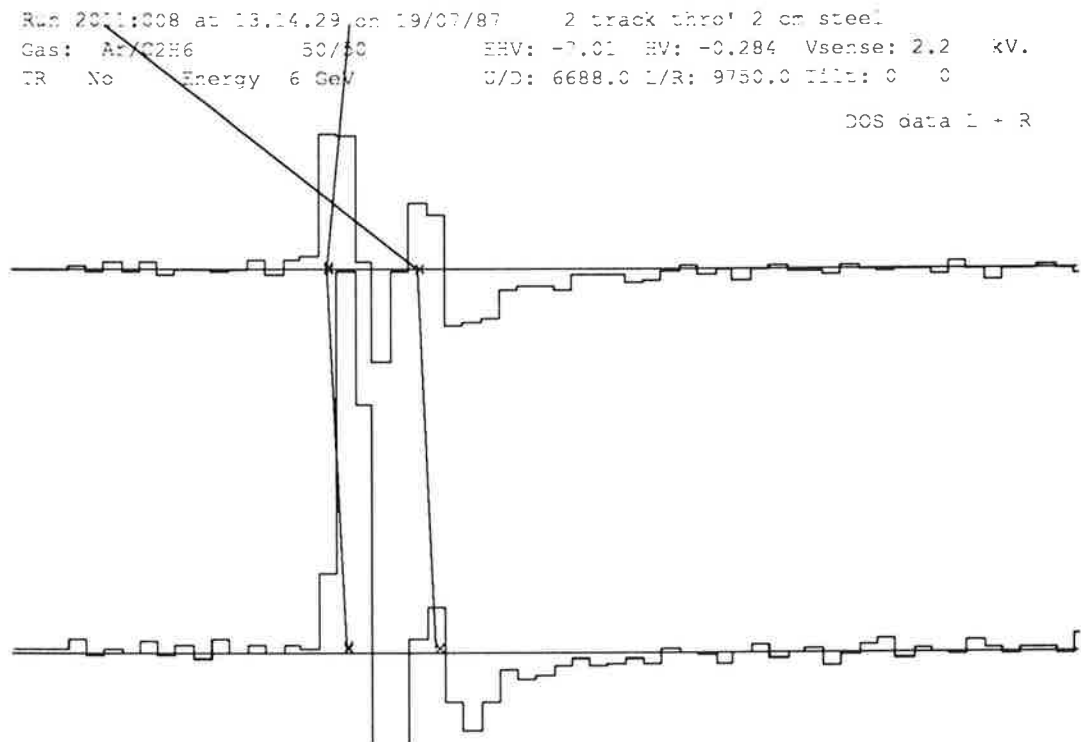


Figure 5.5.4 Zoomed-in view of wires 5 and 6. Wire 5 is above, wire 6 is below.



**Figure 5.5.5** Zoomed-in view of the weighted DOS for wires 5 and 6.



**Figure 5.5.6** Zoomed-in view of the DOS data for wires 5 and 6.

The separation between these pulses is 5 FADC bins for both these wires. In the gas used, Ar/C<sub>2</sub>H<sub>6</sub> 50/50, this corresponds to a spatial separation of 2.5 mm. The improved resolution afforded by the weighted DOS in

comparison to the traditional DOS is apparent, particularly on detecting the second pulse on the trailing edge of the first pulse on wire 6. As this data consists of real multi-track events, the fall-off in efficiency as a result of overlapping hits can not be quantified.

---

- 1** M I Martin, M E Johnson, M J Mayberry and D C DeGroot, IEEE Trans. Nucl. Sci. NS-34 (1987) 258
- 2** A R Clark *et al*, NIM A279 (1989) 243
- 3** The ZEUS detector technical proposal, DESY, 1986
- 4** F F Wilson *et al*. Application of Digital Filtering to Tracking Chamber Signals, ZEUS-RAL-89-004
- 5** Struck DL300 FADC system, using Siemens SDA 5010 6 bit 100 MHz FADC chip
- 6** B Hallgren and H Verweij, IEEE Trans. Nucl. Sci. NS-27 (1980) 333
- 7** SONY CX20118 8 bit 100 MHz FADC chip
- 8** H Breuker *et al*, NIM A260 (1987) 329
- 9** D Schaile, O Schaile and J Schwarz, NIM A242 (1986) 247

# Chapter 6:

## Timing Algorithms

### 6.1 Introduction And Integer Drift Time Evaluation

The drift distance measurement in the radial chambers in H1 will provide an accurate determination of the track sagitta in the  $r\phi$  projection of the solenoidal magnetic field. This will allow the optimum particle momentum precision to be easily achieved. The design drift distance precision for the radial chambers is around  $150\ \mu\text{m}$ , permitting a momentum precision of  $\sigma(p)/p^2 < 0.003\ \text{GeV}^{-1}$ .

A simple threshold cut on the raw FADC data from each wire would create a set of 'integer' drift times associated with the  $9.6\ \text{ns}$  binning of the FADC. For a gas mixture of  $\text{Ar}/\text{C}_2\text{H}_6$  50/50 at a drift field of  $1.2\ \text{kV cm}^{-1}$  the electronic drift velocity is such that  $9.6\ \text{ns}$  corresponds to an electronic drift distance of about  $500\ \mu\text{m}$ , limiting the drift distance precision to an absolute minimum of  $\sim 145\ \mu\text{m}$ . The actual precision obtained under the above conditions on using these 'integer' times is illustrated in figure 6.1.1 (the track fit used in the derivation of these results and the fit shown on the figure are described in sections 6.8 and 6.2 respectively). In order to achieve the desired accuracy of  $150\ \mu\text{m}$  over most of the drift space, an improved drift time must be constructed on the basis of information from the FADC bins adjacent to the 'raw' integer time. In general the correction is derived from the neighbouring and next-to-neighbouring FADC time bins, concentrating on the "leading edge" of the pulse.



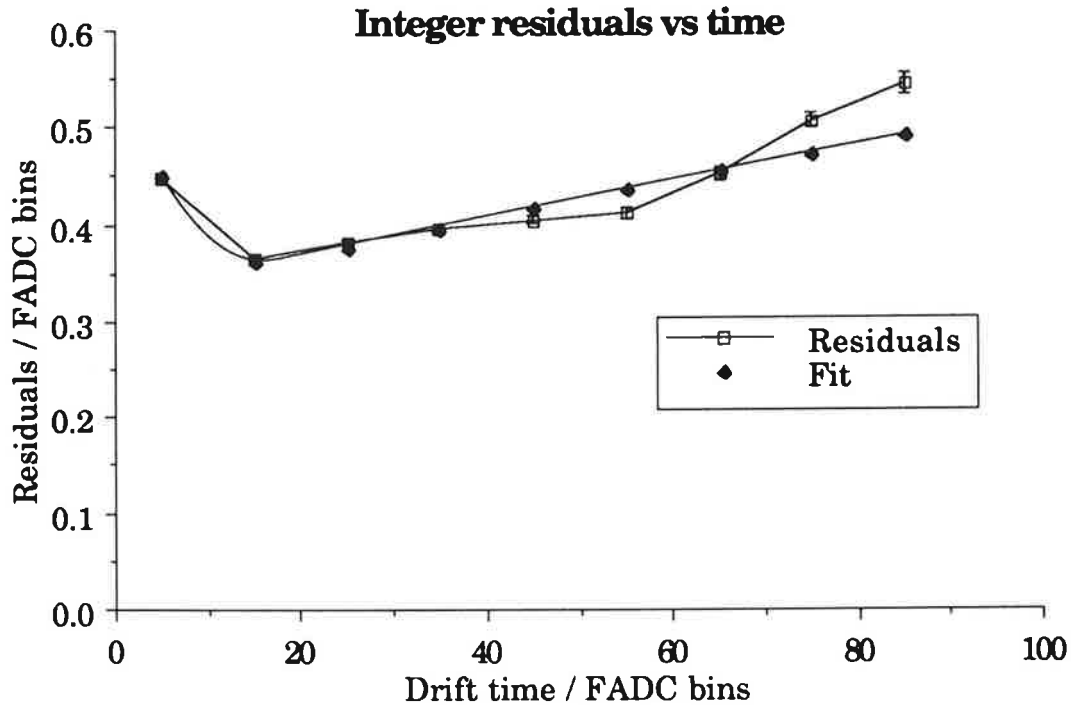


Figure 6.1.1 Drift precision as a function of drift time for ‘integer’ timing, 8 bit 100 MHz FADCs and Ar/C<sub>2</sub>H<sub>6</sub> 50/50.

The calculation of the drift time is a two stage process; first the nearest time bin to the ‘true’ time is identified to give the ‘raw’ integer drift time, then the correction is calculated. For each pulse, the left and right hand re-linearised FADC read-outs of each wire are combined on a bin by bin basis. The ‘raw’ integer drift time,  $t_i$ , is defined as the time bin  $i$  corresponding to the peak in the difference of samples in each region which is above threshold in the weighted DOS, as described in chapter 5. Various different algorithms for calculating the correction,  $\Delta t$ , have been investigated. These are detailed in sections 6.2 to 6.6, where the results of analysing the same data as for figure 6.1.1 are also presented.

Section 6.7 describes a technique for improving the precision for each of the  $\Delta t$  corrections, and section 6.8 describes the fitting procedure used in evaluating the results presented in the previous sections.

There are moreover two distinct scenarios; the left and right hand FADC read-outs can either be treated separately, a single correction being calculated by weighting the left and right hand times according to their charge integral, or the combined data can be used to calculate a single correction. Treating each end separately might be expected to be superior when the propagation delays along the wire are significant, whereas combining the data should result in an improvement when the precision is limited by quantisation effects. For the prototype chambers the latter produces marginally better results, the marked reduction in quantisation effects more than compensating for the errors introduced by neglecting the propagation differences between each end of the wire. The results quoted in the following sections have all been evaluated using the combined data.

None of the prototypes have a total wire length greater than 77 cm, with a maximum propagation delay along the wire of about 5 ns, whereas the full size chambers will have a total combined wire length of 122 cm. The propagation delay effects along the sense wires will be proportionately larger and it may well be necessary to treat each end separately when analysing data from the full size chambers.

## **6.2 Constant Fraction Discrimination Method**

This technique<sup>1</sup>, known as the CFD method, has recently found wide favour within both the H1 and ZEUS collaborations. Having found a pedestal level before the pulse and the pulse maximum, the time corresponding to a set fraction of the difference in pulse height between these is defined to be the 'true' drift time. The correction is calculated within

a FADC bin by linear interpolation. This is one of the fastest algorithms, and also one of the most accurate, particularly over the relatively short drift distances encountered on a jet chamber.

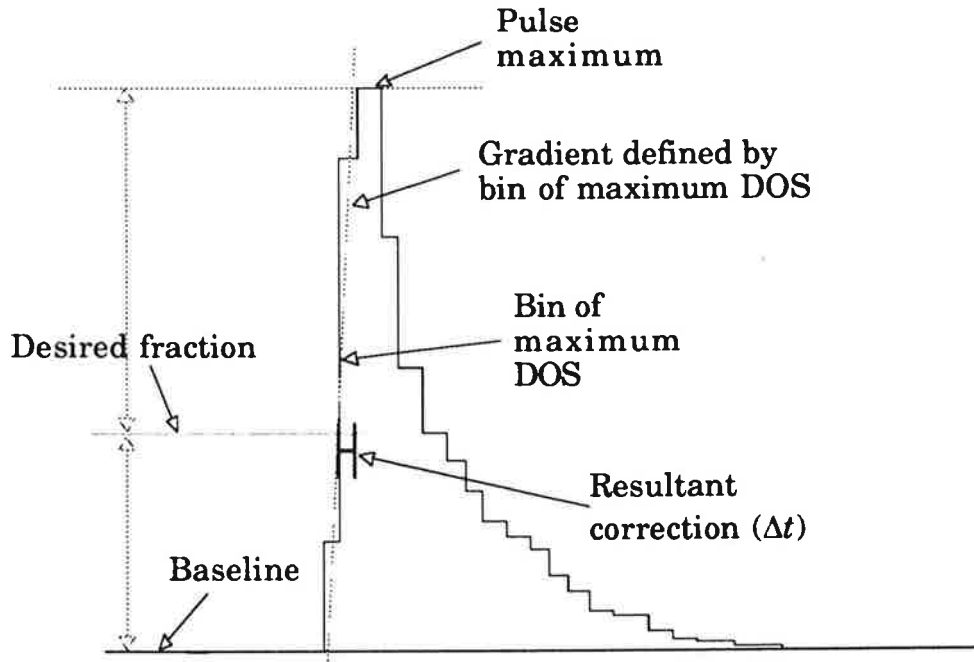


Figure 6.2.1 Illustration of CFD method.

The specific implementation for the radial chambers, illustrated in figure 6.2.1, works as follows:

- the time bin for the hit is as defined above;
- the nearest minimum before the hit is taken as the pedestal;
- the nearest maximum after the hit is taken as the pulse maximum;
- the interpolation is performed by interpolating or extrapolating from the hit bin (peak in DOS) to a specified fraction of the pulse height, using the gradient given by the DOS of the hit bin. The resultant time difference forms the correction.

The extrapolation from the bin corresponding to the peak in the DOS reduces the influence of quantisation errors and noise when the threshold is set very low compared to an interpolation between the FADC bins bracketing the threshold level. The effect of varying the pulse height threshold is summarised in table 6.2.1 below. The values quoted are the point precision results derived from a Gaussian fit to the overall fitted track residual distribution and from fitting the RMS track residuals as a function of drift distance to:

$$\sigma^2 = A^2 + B^2x + C(x) \quad [6.2.1]$$

$\sigma$  is the point precision,  $A$  and  $B$  define the expected parametrisation of precision with drift distance due to longitudinal diffusion<sup>2</sup>, and  $C$  is a term to account for poor precision at very short drift distances.

% height	$\sigma'/\mu\text{m}$	$A'/\mu\text{m}$	$B'/\mu\text{m} \sqrt{\text{cm}}^{-1}$	$\sigma/\mu\text{m}$	$A/\mu\text{m}$	$B/\mu\text{m} \sqrt{\text{cm}}^{-1}$
0	152	87	86	151	81	86
5	154	88	86	153	82	87
10	157	89	88	155	84	87
20	163	91	90	161	91	89
30	170	94	94	168	95	92
40	177	100	98	175	99	95
50	186	105	102	183	105	98

Table 6.2.1 Drift precision for various threshold levels using CFD timing, 8 bit 100 MHz FADCs and Ar/C<sub>2</sub>H<sub>6</sub> 50/50.

The nature of the track fit means that the track residuals are underestimates of the true point precision by a factor  $\sqrt{\frac{9}{12}}$ . The results quoted have therefore been corrected for this factor.  $\sigma'$ ,  $A'$  and  $B'$  are the results using the  $\Delta t$  derived as above,  $\sigma$ ,  $A$  and  $B$  using this  $\Delta t$  calibrated as

discussed in section 6.7. The resultant precision with the threshold set at 10% is illustrated in figure 6.2.2, incorporating the transformation discussed in section 6.7, under the same conditions as for figure 6.1.1, along with the above fit.

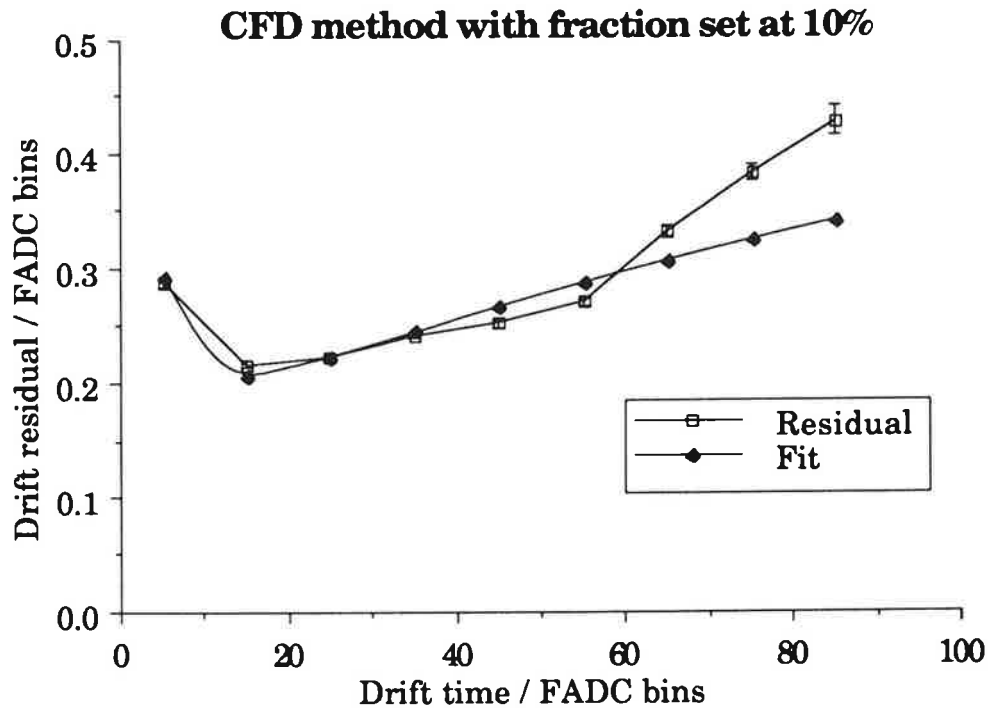


Figure 6.2.2 Drift precision as a function of drift time for CFD timing with the threshold set at 10%, 8 bit 100 MHz FADCs and Ar/C<sub>2</sub>H<sub>6</sub> 50/50.

### 6.3 First Electron Method

This algorithm is equivalent to the CFD method with the required fraction of the total pulse height set to zero; the gradient given by the DOS of the hit bin is extrapolated down to give an intercept with the pedestal with no reference to the pulse maximum. The distribution of this intercept,  $\alpha$ , measured relative to the 'raw' drift time, is approximately triangular in the range between  $-1.5$  and  $0$  FADC bins, and is shown in figure 6.3.1 for data taken with both the DL300 and DL3000. The slight

difference between the distributions arises from the improved precision with the DL3000 data, which also accounts for the reduced discontinuity at  $\alpha = -5$  ns, this being a result of quantisation effects.

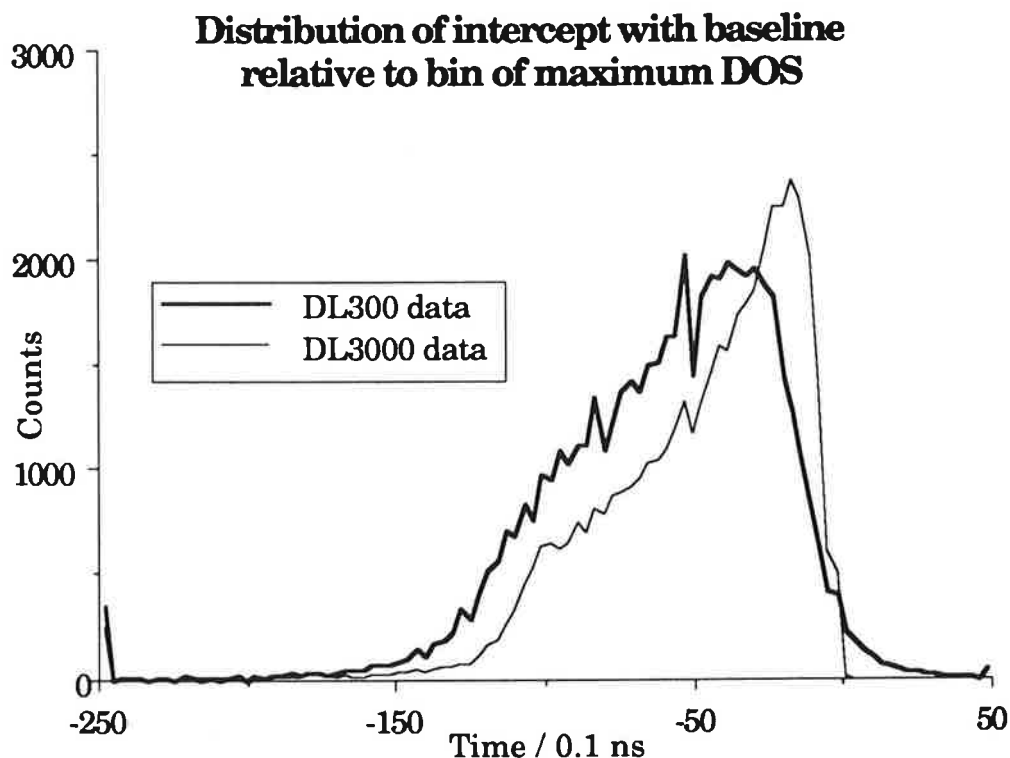


Figure 6.3.1 Distribution of leading edge intercept with the base line relative to the bin of maximum DOS.

The correction  $\Delta t(\alpha)$  to be applied to the crude drift time should be distributed uniformly in the range  $-0.5$  to  $+0.5$  over a sample of events, assuming that the bin of maximum DOS is the nearest bin to the 'true' time. On the assumption that this intercept,  $\alpha$ , is a monotonic function of the desired timing correction, the histogrammed distribution may be readily inverted to give a timing correction as a function of intercept. The technique for performing this is outlined in section 6.7. The resultant precision is illustrated in figure 6.3.2.

Again this is a very fast and accurate timing algorithm, with an overall point precision of  $\sigma = 152 \mu\text{m}$ ,  $A = 82 \mu\text{m}$  and  $B = 87 \mu\text{m} \sqrt{\text{cm}^{-1}}$ . It makes

reference to the pedestal level, as with the CFD method, but does not require a pulse maximum. The slight difference in results between this method and the CFD method with the fraction set to 0 are a result of a different definition of the base line. As implemented here the data are assumed to already be pedestal subtracted, whereas in the CFD method an independent pedestal is calculated.

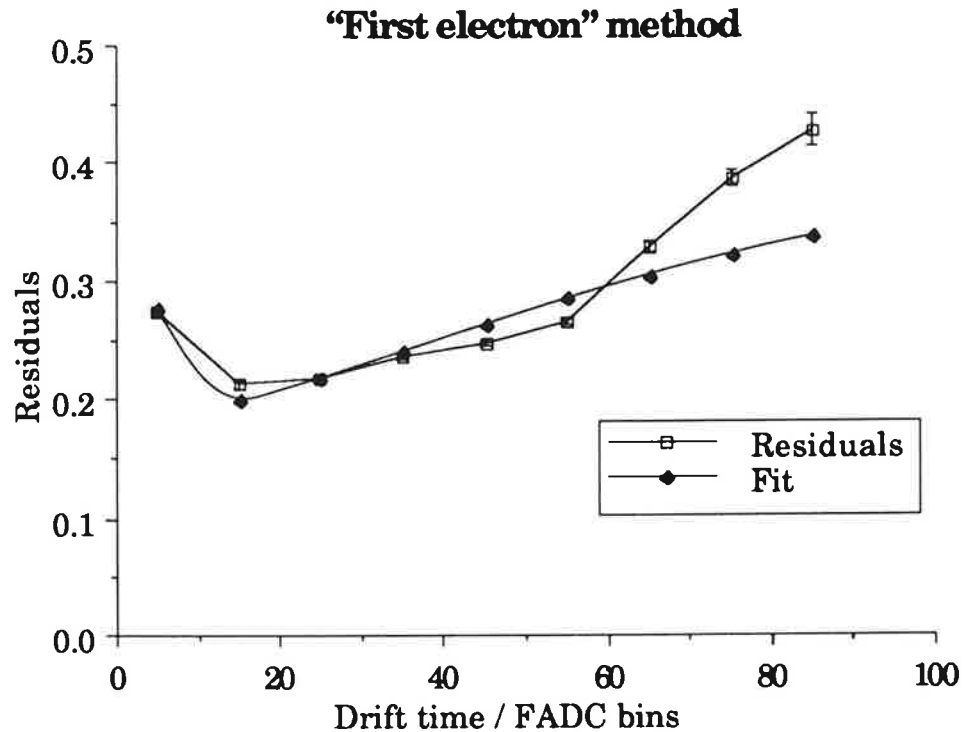


Figure 6.3.2 Drift precision as a function of drift time for “first electron” timing, using 8 bit 100 MHz FADCs and Ar/C<sub>2</sub>H<sub>6</sub> 50/50.

## 6.4 Fraction Of Charge Method

The two methods outlined above concentrate on the leading edge of the pulse. An alternative method has also been tried, which extracts timing information from the whole pulse rather than the leading edge alone, reducing the effect of longitudinal diffusion in the drifting electron swarm over large drift distances. The pulse is integrated from the start

until a set fraction of the total charge has arrived; the total charge is assumed to be the pulse integral for the charge division measurement. Within the  $j^{\text{th}}$  FADC bin corresponding to time  $t_j$  the instantaneous pulse height at time  $t$ ,  $h_j(t)$ , is assumed to be a linear function of time (figure 6.4.1), namely:

$$h_j(t) = \frac{(a_{j+1} - a_{j-1})}{2} (t - t_j) + a_j \quad [6.4.1]$$

where  $a_j$  is the FADC contents for bin  $j$ .

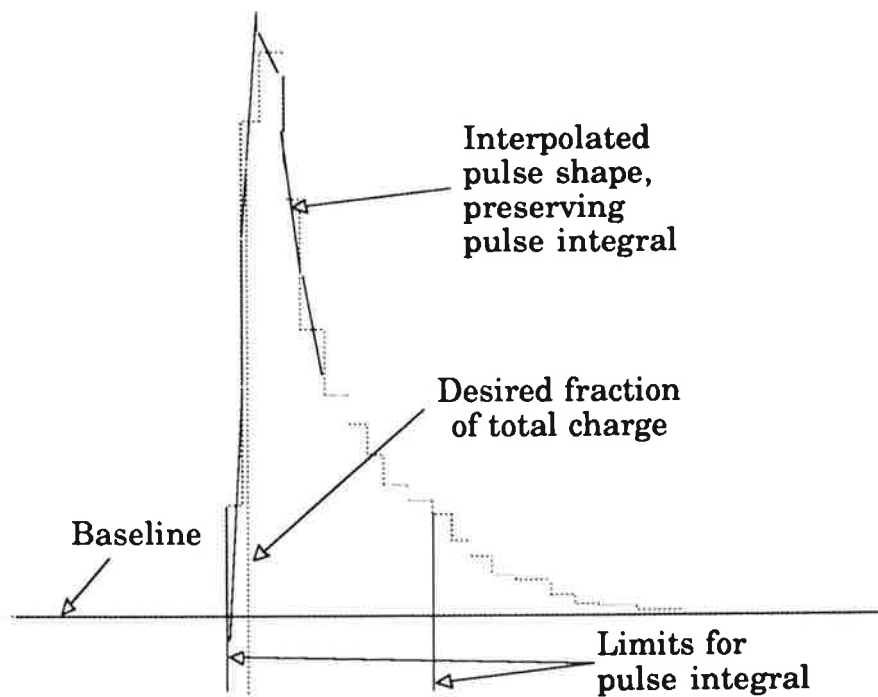


Figure 6.4.1 Illustration of fraction of charge method.

This parametrisation represents a reasonable compromise between computational effort and smoothness of the resulting pulse shape, with the feature that the pulse integral for each bin remains equal to the bin contents, thus ensuring agreement on a bin by bin basis with the integrated pulse. The square root required in converting from pulse integral to drift time however rules out the use of this algorithm on-line, as the front end processor will only be capable of integer arithmetic.



This method was envisaged as a fast alternative using the entire pulse profile to a reference pulse algorithm; the latter has the disadvantage that sets of reference pulses must be constructed for various drift distances and different shifts within an FADC bin. However the reason for using the entire pulse profile, namely the degradation in the timing information contained in the leading edge as a result of longitudinal diffusion, generally sets in at larger drift distances than those encountered in the H1 radial chambers<sup>3</sup>. Over the drift distances encountered in the H1 radial chambers the fraction of charge method produces worse results than any of the preceding methods (table 6.4.1).

% charge	$\sigma'/\mu\text{m}$	$A'/\mu\text{m}$	$B'/\mu\text{m}$	$\sqrt{\text{cm}^{-1}}$	$\sigma/\mu\text{m}$	$A/\mu\text{m}$	$B/\mu\text{m}$	$\sqrt{\text{cm}^{-1}}$
5	186	124	93		180	117	91	
10	206	140	101		196	134	94	
15	228	162	106		208	146	98	
20	259	192	114		225	159	105	
30	299	238	122		266	179	131	

Table 6.4.1 Drift precision for various threshold levels using fraction of total charge timing, 8 bit 100 MHz FADCs and Ar/C<sub>2</sub>H<sub>6</sub> 50/50.

## 6.5 Weighted Average Of DOS Method

An alternative scheme uses the cluster of positive bins around the maximum in the DOS, a technique originally developed within the OPAL group<sup>4</sup>. No reference is made to the absolute pulse height or to the pedestal level, rendering this a useful technique for processing overlapping pulses. A weighted average is calculated using these bins, to give a correction  $\Delta t$  to  $t_i$ , where  $d_i$  is the DOS for time bin  $i$ :

$$\Delta t = \frac{\sum_{j=-2}^1 j \cdot w_j \cdot d_{i+j}}{\sum_{j=-2}^1 w_j \cdot d_{i+j}} \quad [6.5.1]$$

Various weighting values have been used in order to try to obtain a flat distribution between  $-0.5$  and  $+0.5$  for this correction. No obvious technique exists for determination of these weights, but the final set used are  $w_j = 1.5, 2.0, 1.5$  and  $0.5$  for the bins  $d_{i-2}$  to  $d_{i+1}$  respectively. The correction distribution is shown in figure 6.5.1, where the spike at zero is a result of binning effects. This gives an overall point precision of  $\sigma' = 182 \mu\text{m}$ ,  $A' = 111 \mu\text{m}$  and  $B' = 97 \mu\text{m} \sqrt{\text{cm}}^{-1}$  before calibration and  $\sigma = 159 \mu\text{m}$ ,  $A = 94 \mu\text{m}$  and  $B = 86 \mu\text{m} \sqrt{\text{cm}}^{-1}$  after calibration. The resultant residuals as a function of drift time are illustrated in figure 6.5.2.

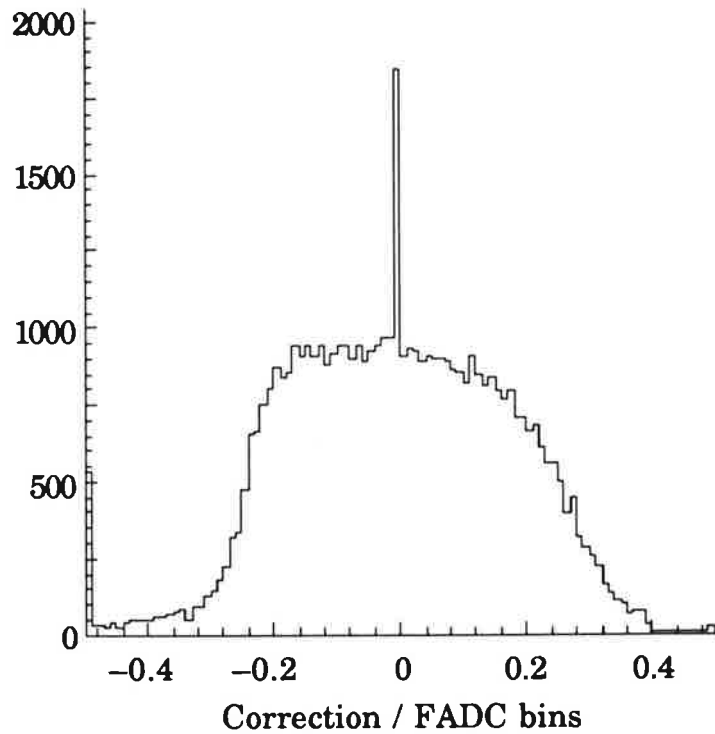


Figure 6.5.1 Distribution of weighted average of DOS correction relative to the bin of maximum DOS.

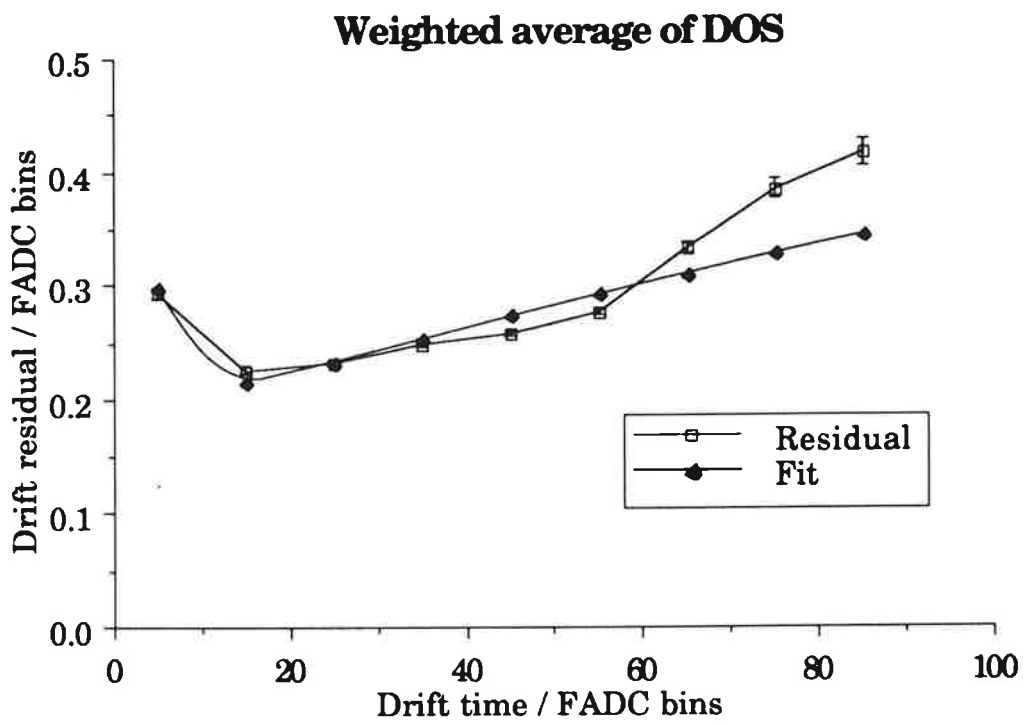


Figure 6.5.2 Drift precision as a function of drift time for weighted average of DOS timing, using 8 bit 100 MHz FADCs and Ar/C<sub>2</sub>H<sub>6</sub> 50/50.

## 6.6 Newton Raphson Method

The first three methods described above rely on the pulse sitting on a well defined base line, and their use with resolved but overlapping pulses requires that the fitted first pulse be subtracted off before analysing any second pulse. A second alternative which makes no reference to any pedestal level was devised specifically for this overlapping scenario; the method consists of approximating higher derivatives of the pulse shape by extending the definition of the difference of samples. This permits the application of the Newton Raphson interpolation algorithm in order to find a better estimate of the turning point in the DOS data corresponding to the maximum on the rising edge.

The difference of samples is defined as:

$$d_i = \left( \frac{da_i}{dt} \right) = a_i - a_{i-1} \quad [6.6.1]$$

The desired quantity is the time corresponding to the maximum DOS, namely when:

$$\left( \frac{d^2 a_i}{dt^2} \right) = 0 \quad [6.6.2]$$

The Newton Raphson formula defines an iterative procedure to find solutions to:

$$f(x_j) = 0 \quad [6.6.3]$$

where  $x_j$  is the  $j^{\text{th}}$  approximation to the solution. An improved value is given by:

$$x_{j+1} = x_j - \frac{f(x_j)}{f'(x_j)} \quad [6.6.4]$$

In order to apply this technique, the second and third time derivatives of the pulse shape must be defined. Equation [6.6.1] can be considered as the first derivative evaluated midway between time bins  $i-1$  and  $i$ . Extending this definition gives:

$$\left(\frac{d^2 a_i}{dt^2}\right) = \frac{1}{2}(a_{i+1} + a_{i-2} - a_i - a_{i-1}) \quad [6.6.5]$$

$$\left(\frac{d^3 a_i}{dt^3}\right) = a_{i+1} - 3a_i + 3a_{i-1} - a_{i-2} \quad [6.6.6]$$

where the derivatives are all centred midway between time bins  $i-1$  and  $i$ . Application of equation [6.6.4] then gives the correction:

$$\Delta t = -\frac{1}{2} \frac{(a_{i+1} + a_{i-2} - a_i - a_{i-1})}{(a_{i+1} - 3a_i + 3a_{i-1} - a_{i-2})} \quad [6.6.7]$$

### “Newton Raphson” method

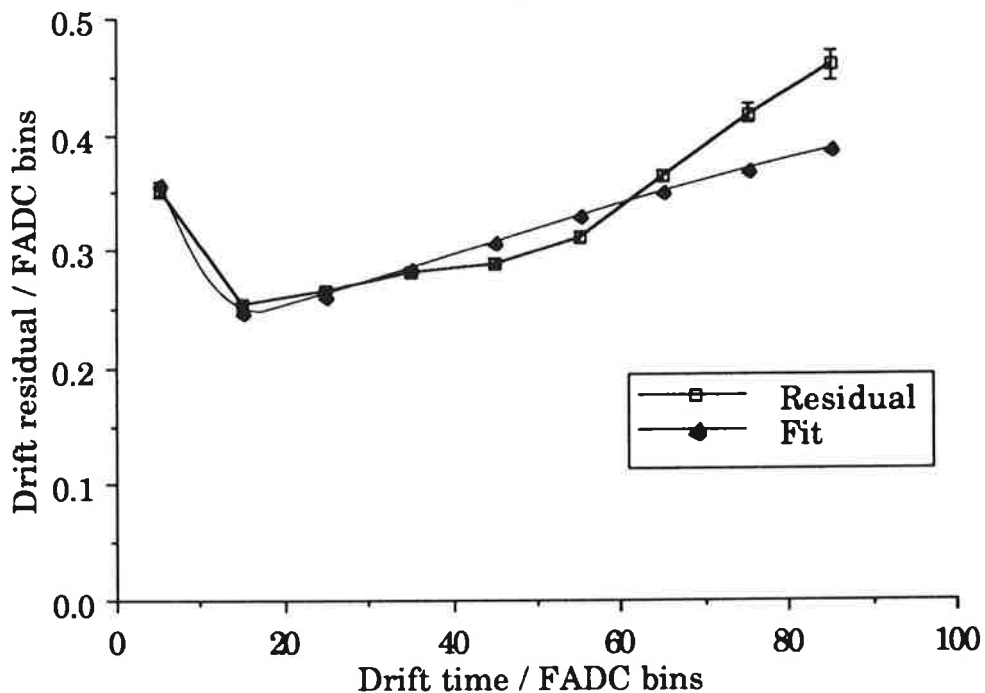


Figure 6.6.1 Drift precision as a function of drift time for Newton Raphson method, using 8 bit 100 MHz FADCs and Ar/C<sub>2</sub>H<sub>6</sub> 50/50.

The results obtained with this method are illustrated in figure 6.6.1. The method gives an overall point precision of  $\sigma' = 182 \mu\text{m}$ ,  $A' = 113 \mu\text{m}$  and  $B' = 94 \mu\text{m} \sqrt{\text{cm}^{-1}}$  before calibration and  $\sigma = 180 \mu\text{m}$ ,  $A = 106 \mu\text{m}$  and  $B = 96 \mu\text{m} \sqrt{\text{cm}^{-1}}$  after calibration. For isolated pulses this technique is less precise than the weighted average of DOS method.

## 6.7 Further Refinements

All the above algorithms produce a correction to the integer time corresponding to the detected hit. In general the distribution of the correction should be a 'top hat' function between  $-0.5$  and  $+0.5$ , assuming that the integer time is the nearest integer to the true time. The validity of this assumption is illustrated in figure 6.7.1, which depicts the distribution of fit residuals for 'integer' timing. The standard deviation is  $0.42$  FADC bins, showing that the assumption is acceptable.

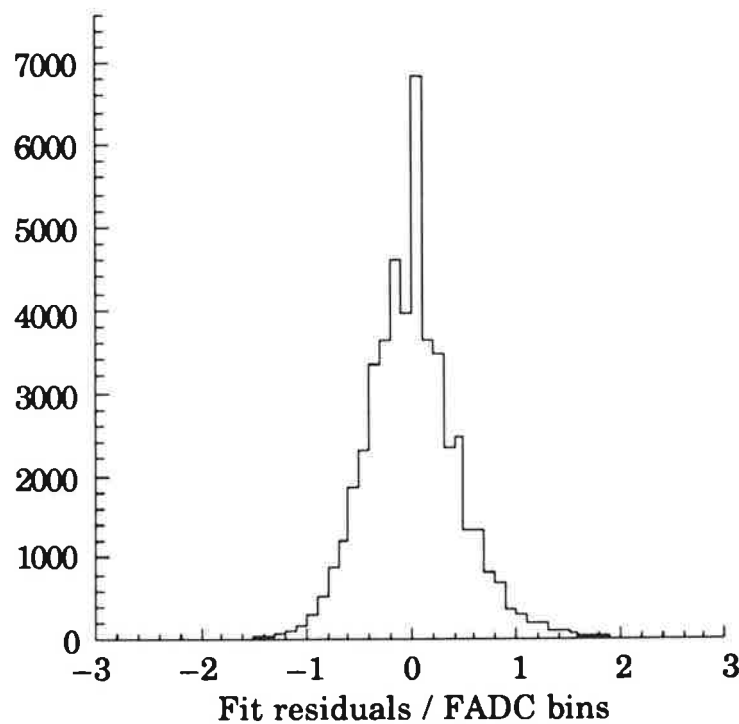


Figure 6.7.1 Histogram of drift time residuals for 'integer' timing, using 8 bit 100 MHz FADCs and Ar/C<sub>2</sub>H<sub>6</sub> 50/50.

However the distributions of the timing correction for the various algorithms never correspond perfectly to this 'top hat' shape. With the additional assumption that the correction with a particular algorithm is a monotonic function of the true time, one may improve the correction by applying a transformation to it such that the resultant correction distribution does have the desired 'top hat' shape. The required transformation is readily derived from the histogram of the original correction distribution.

First consider the raw distribution, here using the raw first electron technique (figure 6.7.2).

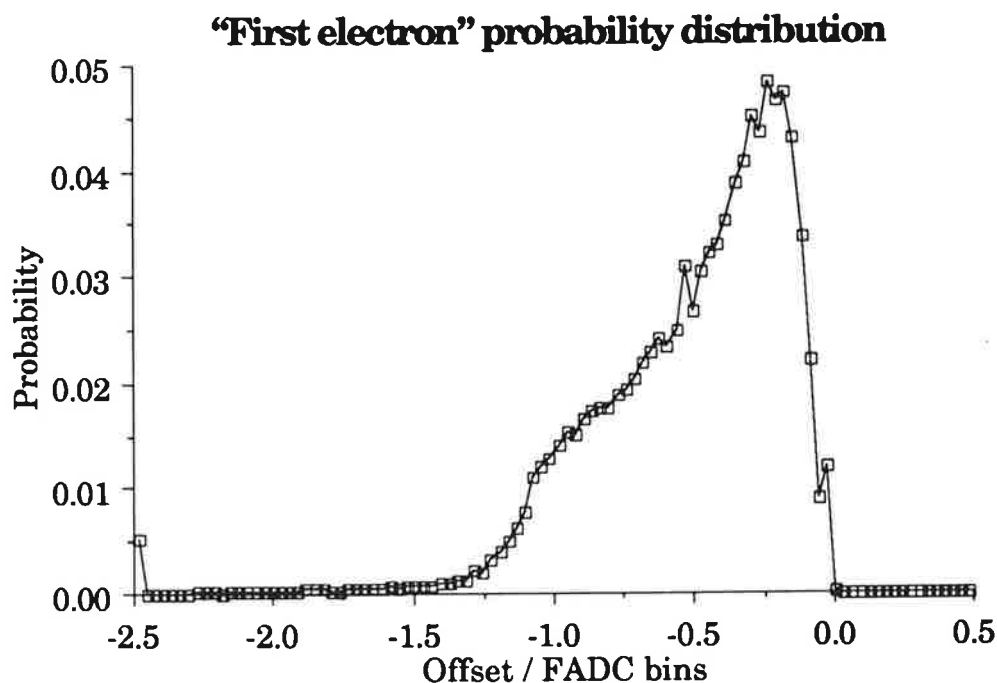


Figure 6.7.2 Distribution of leading edge intercept with the base line relative to the bin of maximum DOS.

The cumulative probability distribution for obtaining a value of the correction less than or equal to that obtained in any particular event is easily derived from this distribution by simply summing the channel contents up to and including the required bin and then normalising by di-

viding through by the total integrated contents. This results in the distribution illustrated in figure 6.7.3.

Also illustrated in figure 6.7.3 is the cumulative probability distribution for the desired 'top hat' correction. The mapping between any two arbitrary correction distributions is defined by the assumption that both are monotonic functions of the 'true' correction. The transformation from the first distribution to the second is obtained by taking the cumulative probability value corresponding to a particular value in the first distribution and using this to read off the equivalent value in the second distribution. As the 'top hat' correction distribution is a linear function of the cumulative probability, the transformation is particularly simple.

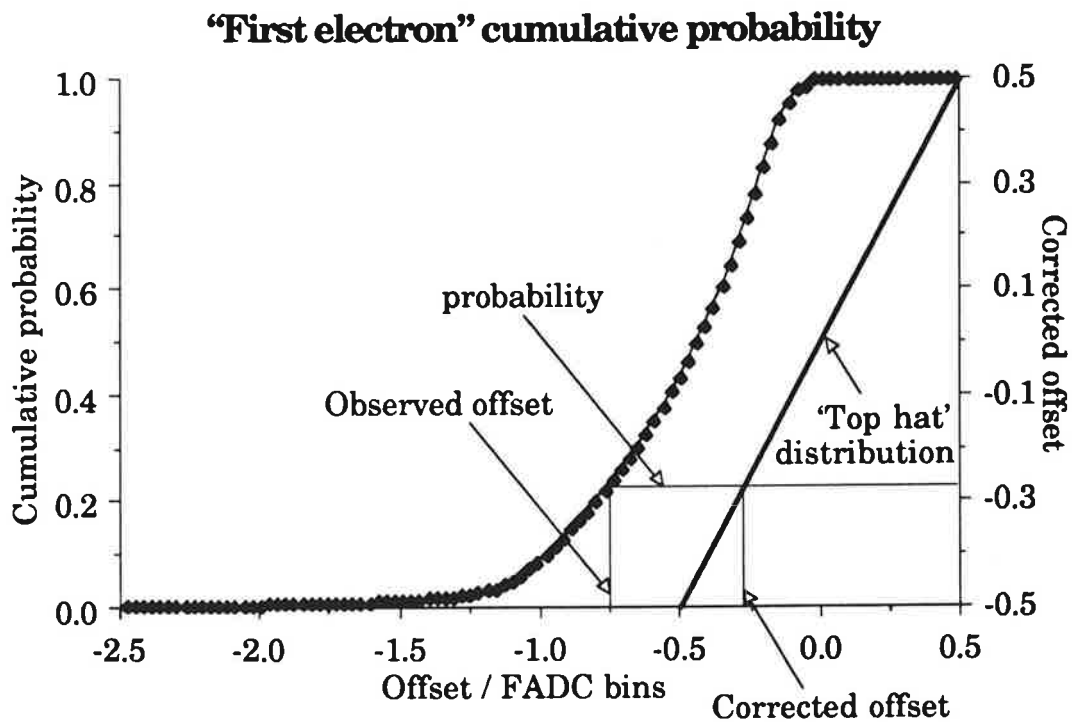


Figure 6.7.3 Cumulative probability distributions for the first electron timing algorithm and the desired 'top hat' function.



The resultant timing correction distribution after calibration with the above algorithm is illustrated in figure 6.7.4. The improvement on using this technique with each algorithm has already been detailed above.

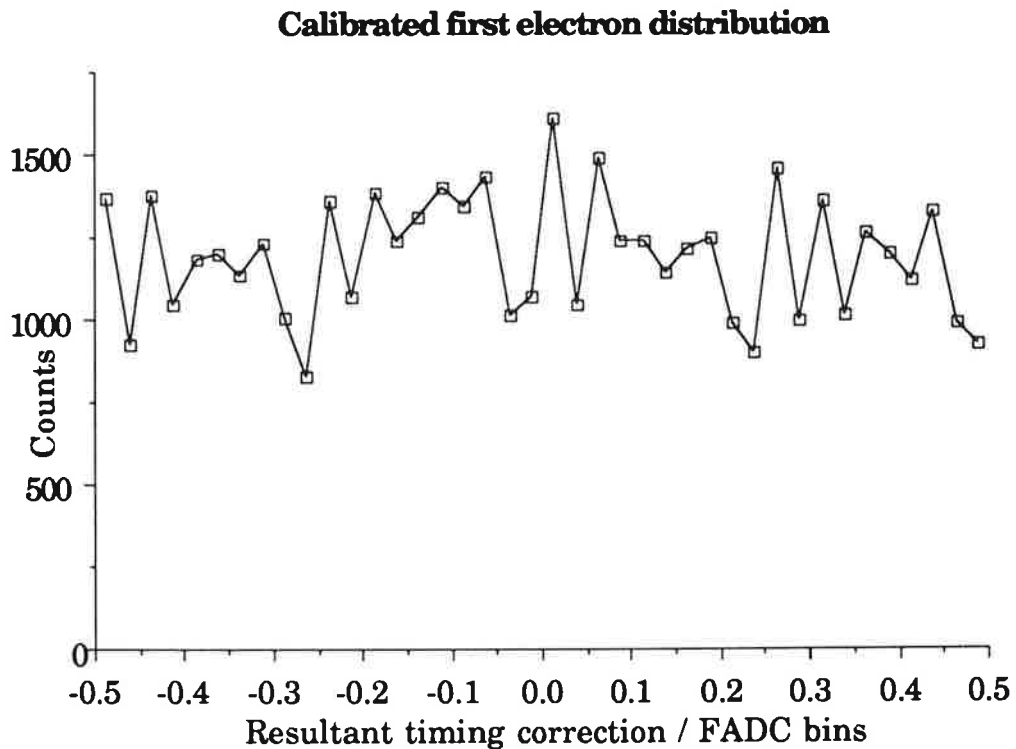


Figure 6.7.4 Timing correction distribution after calibration for the first electron method.

## 6.8 Track Fitting

As a prototype pattern recognition program for the FTD was already extant<sup>5</sup> when the first test beam data were taken, and this pattern recognition is based on the track segments found in the radial chambers, it was not necessary to write a pattern recognition program for track segments within a radial wedge. Instead an interface to the existing pattern recognition program was written<sup>6</sup>. This returns the hit numbers corresponding to the fitted tracks, and also the assumed stagger for each of

these hits. The hit information is then used for a second fit to the best track candidate.

For those events where the track does not cross the sense wire plane the drift time for each wire,  $t_k$ , can be fitted by:

$$t_k = a z_k + b + \frac{s_k}{v} \quad [6.8.1]$$

with 3 free parameters ( $a$ ,  $b$  and  $\frac{1}{v}$ ) using the known wire staggers  $s_k$ , and wire positions  $z_k$ . The sign of the fitted drift velocity,  $v$ , resolves the left/right ambiguity.

The comparison between this calculated drift velocity, depending as it does only on the near/far timing difference arising from the sense wire stagger and the *a priori* known drift velocity for the gas provides a powerful probe into systematic effects in the electron drift in the chamber. For example the cross-talk compensation discussed in chapter 5 changes this measured drift velocity by 10%. The RMS spread in values of the fitted velocity from event to event moreover gives a direct measure of how well the left/right ambiguity is resolved. This is depicted in figure 6.8.1 for two sets of Ar/C<sub>2</sub>H<sub>6</sub> data, 6 bit FADC and 200  $\mu$ m stagger, and 8 bit FADC and 300  $\mu$ m stagger. With the 6 bit FADC data all the tracks are on the one side of the wire plane.

Although useful as a consistency check, this obviously does not provide an accurate method of measuring the electron drift velocity in the chamber.

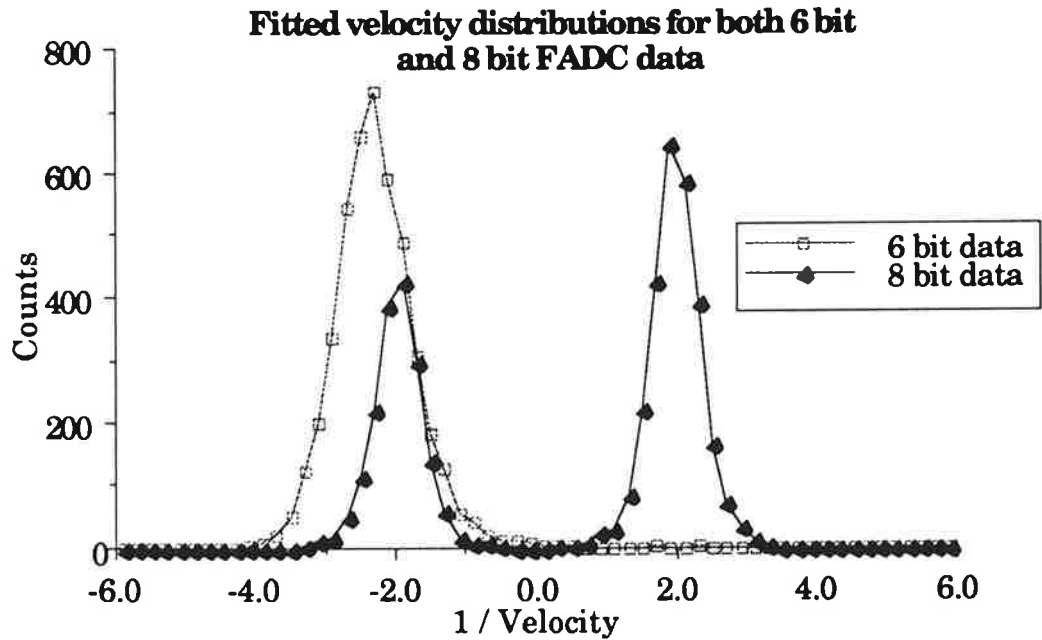


Figure 6.8.1 Fitted drift velocity distributions.

An accurate determination of the electron drift velocity is possible by making use of the location of the beam spot passing through the chamber when this is known. The variation of the centroid of the drift time distribution with chamber location is portrayed in figure 6.8.2, for the same data as used in the above analysis. The large beam spot size of about 1 cm results in the centroid at small drift times being shifted, as tracks may be on either side of the wire plane, as evidenced by the reduction in the time difference between the data for the two wires shown. Apart from this, the effect of the wire stagger is clearly visible in the other data points. Using the three most negative values of chamber location ( $U/D$ ) gives a measured drift velocity of  $54 \pm 0.5 \mu\text{m ns}^{-1}$ , in excellent agreement with more rigorous measurements in  $\text{Ar}/\text{C}_2\text{H}_6$  50/50 with a drift field of  $1.2 \text{ kV cm}^{-1}$  at atmospheric pressure<sup>7</sup>. The errors quoted include only the statistical contribution. Unfortunately the lack of agreement in the literature would tend to suggest that systematic effects are more important. Taking the most positive  $U/D$  data point and assuming a linear time distance relationship then gives the offset between the

FADC start and when the track passed through the chamber as 10.4 FADC bins, at  $U/D = -0.73$  cm. This fit is also shown in figure 6.8.2.

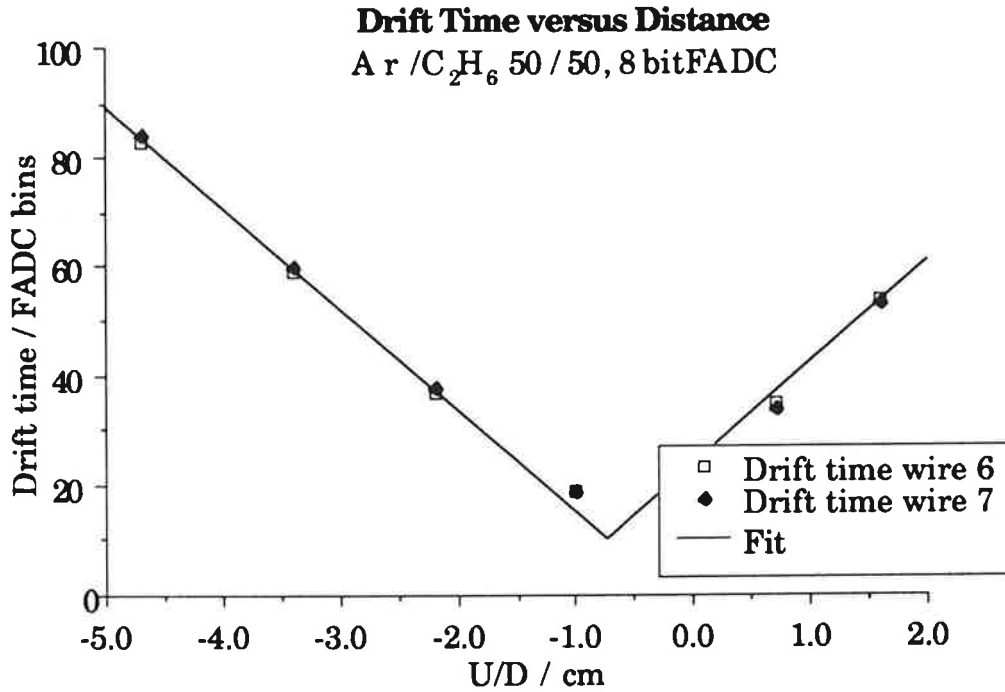


Figure 6.8.2 Fitted drift time centroid versus chamber location ( $U/D$ ).

For tracks which cross the wire plane, one may further subdivide the class into two groups: angled tracks which cross the wire plane once, and tracks which cross more than once. Those tracks which crossed the wire plane once, between wire planes  $k'$  and  $k' + 1$ , can be fitted to:

$$t_k = t_0 + a z_k + f_k \left( b + \frac{s_k}{v} \right) \quad [6.8.2]$$

$t_0$  now corresponds directly to the time offset between the track passing through the chamber and the start of the FADCs and  $f_k$  is given by:

$$f_k = \begin{cases} 1.0 & k \leq k' \\ -1.0 & k > k' \end{cases} \quad [6.8.3]$$

The resultant  $t_0$  distribution from the above analysis for data from the second prototype where the chamber has been tilted by  $7^\circ$  is shown in

figure 6.8.3. The effect of the chamber tilt on each event is illustrated in figure 6.8.4, where the track is seen to move toward the wire plane on the first 6 wires and then away again on the last 6 wires. This effect is also visible as the separation between the drift times for each wire in figure 6.8.5, which also summarises the results of the same analysis as for figure 6.8.2. The mean of the  $t_0$  distribution in figure 6.8.3 is  $t_0 = 9.0$  FADC bins, whereas the data for wires 10 and 11 in figure 6.8.5 give a value of  $t_0 = 9.7$  FADC bins along with a drift velocity of  $32 \mu\text{m ns}^{-1}$ . The data were taken with a Xe/He/C<sub>2</sub>H<sub>6</sub> 20/50/30 mixture at a drift field of  $1.0 \text{ kV cm}^{-1}$ .

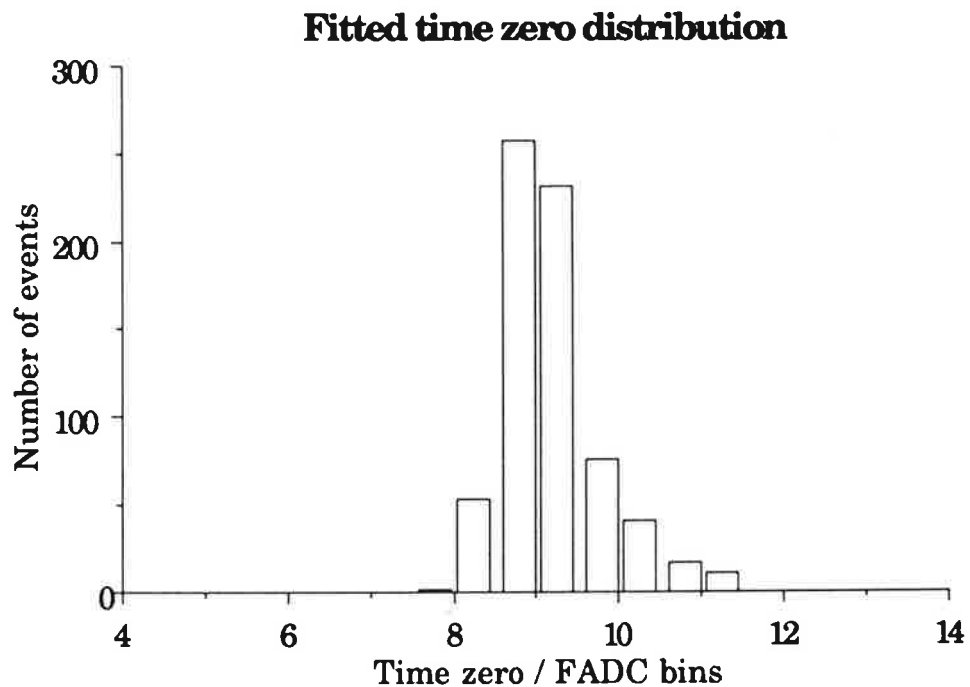


Figure 6.8.3 Fitted  $t_0$  distribution from sample of tilted tracks.

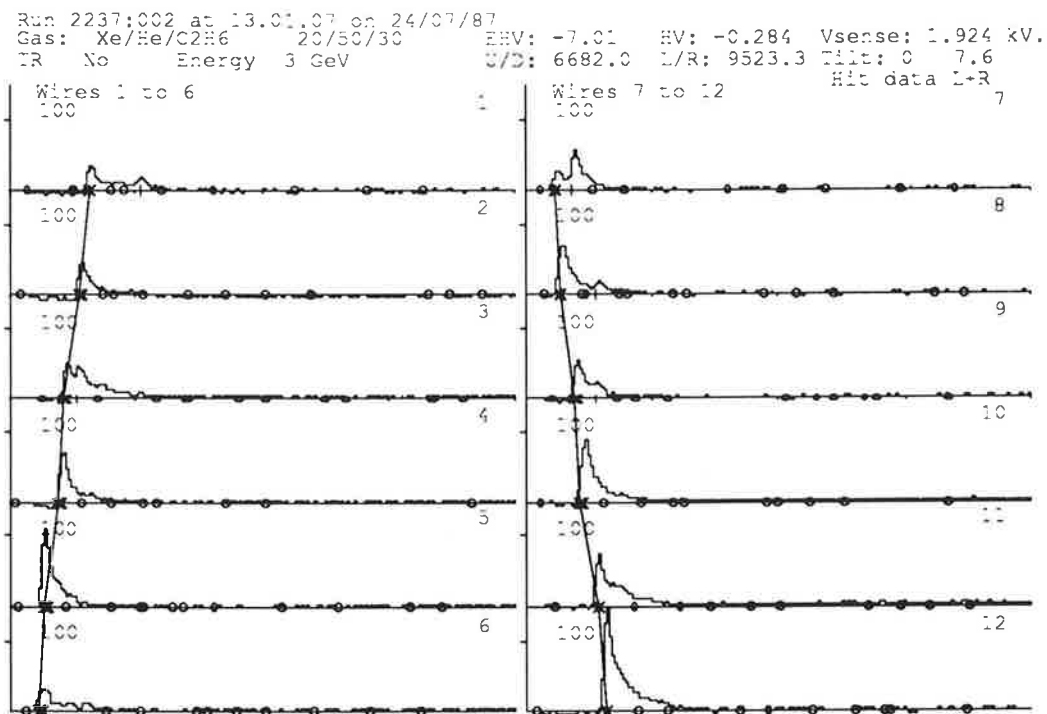


Figure 6.8.4 Event display of one of the tilted tracks. The track crosses the wire plane between wires 6 and 7.

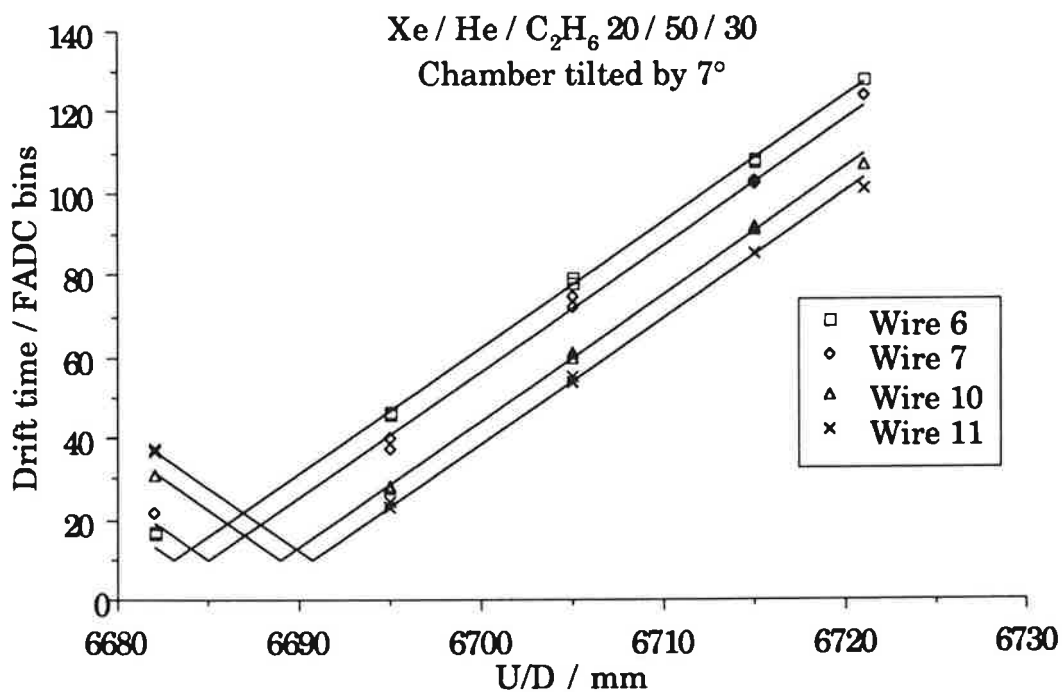


Figure 6.8.5 Fitted drift time centroid versus position for the sample of tilted tracks.

## 6.9 Conclusions

From the above, for a prototype H1 radial chamber wedge in the absence of any magnetic field, the favoured timing algorithm for isolated pulses is the “first electron” method. For overlapping pulses it would appear that the weighted average of DOS method will produce the best results, although some systematic evaluation of the weights used should be attempted. With Ar/C<sub>2</sub>H<sub>6</sub> 50/50 at atmospheric pressure and a drift field of 1.2 kV cm<sup>-1</sup> the desired single track performance may be achieved over almost all the drift region. The effects of the magnetic field and of using different gas mixtures are considered in chapter 9.

All these algorithms depend critically on the shape of the leading edge of the pulse. The choice of which algorithm to use and what parameters to use with that algorithm must be re-evaluated whenever any changes liable to influence the pulse shape are undertaken. For example the effect of using 6 bit FADCs instead of 8 bit FADCs is illustrated in figure 6.9.1.

The final choice of the algorithms to be used in H1 is therefore only likely to be made once initial real data is available from the installed system within the H1 solenoid. Indeed the choice of whether to evaluate separate times for each end of the wire or a single time based on the summed signal may also only be decided on the basis of real data.

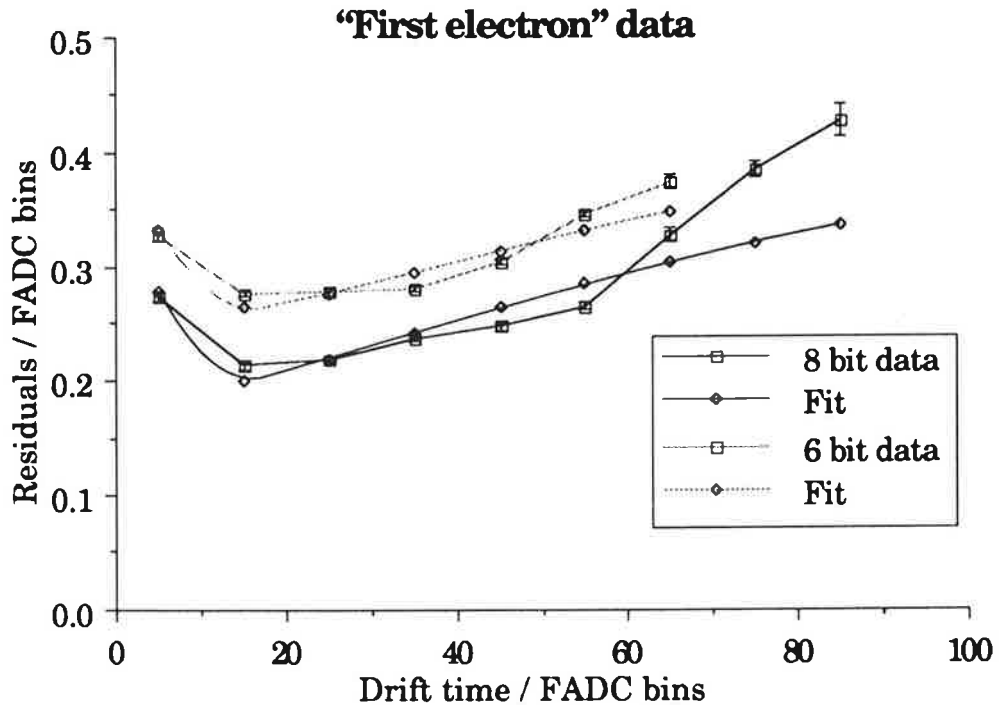


Figure 6.9.1 Point precision using “first electron” timing with 6 bit FADC and 8 bit FADC data.

- 
- 1 S M Tkaczyk *et al*, NIM A270(1988) 373
  - 2 F Sauli, Principles of operation of multiwire proportional and drift chambers, CERN 77-09 (1977), and P Bock *et al*, NIM A242 (1986) 237
  - 3 P Bock *et al*, NIM A242 (1986) 237
  - 4 D Schaile, O Schaile and J Schwarz, NIM A242 (1986) 247
  - 5 pattern recognition written by I O Skillicorn
  - 6 courtesy of S J Maxfield
  - 7 A Peisert and F Sauli, Drift and diffusion of electrons in gases: a compilation, CERN 84-08 (1984)



# Chapter 7:

## Charge Integration

### 7.1 Introduction

In addition to good drift distance precision and good point resolution the radial chambers will also have to provide the hit position along the radial wire. This will be achieved by using resistive anode wires and reconstructing the coordinate by division of the charge collected at each end of the wire.

Charge division lends itself to use in the radial chambers because it only depends on the ratio of the resistances to either side of the impact point and is independent of the resistance, capacitance and inductance distribution along the anode<sup>1</sup>. Therefore the wedge shape of the drift cell and the presence of the hub connection do not affect the intrinsic linearity and precision of the measurement. Reconstructing the coordinate by measuring the timing difference between each wire end, on the other hand, depends on the RC distribution along the anode.

The sense wire diameter is specified by the simultaneous requirement for  $\frac{dE}{dx}$  measurements and total ionisation collection, as outlined in chapter 3. A large anode resistance is desirable for accurate charge division measurements in order to reduce thermal noise<sup>2</sup> and to achieve “critical damping” of the time development of the charge division signal<sup>1</sup>. The total anode resistance may then be maximised by using the most resistive wire available. For 50  $\mu\text{m}$  diameter wire Stablohm 800<sup>3</sup> has a specific resistance of  $7 \Omega \text{ cm}^{-1}$ , compared to  $5.3 \Omega \text{ cm}^{-1}$  for Ni/Cr<sup>4</sup>. This gives a to-

tal wire resistance of  $900 \Omega$  for a connected pair of wires (the reasons for inter-connecting sense wires are described in the next section).

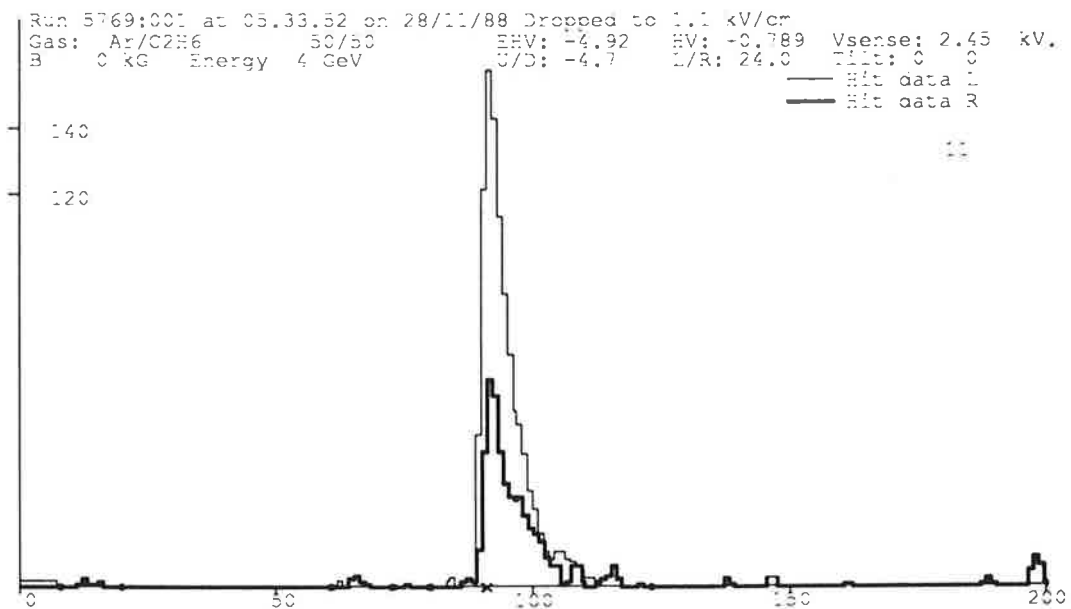


Figure 7.1.1 Example of pulse where the beam spot is at wide end of the chamber.

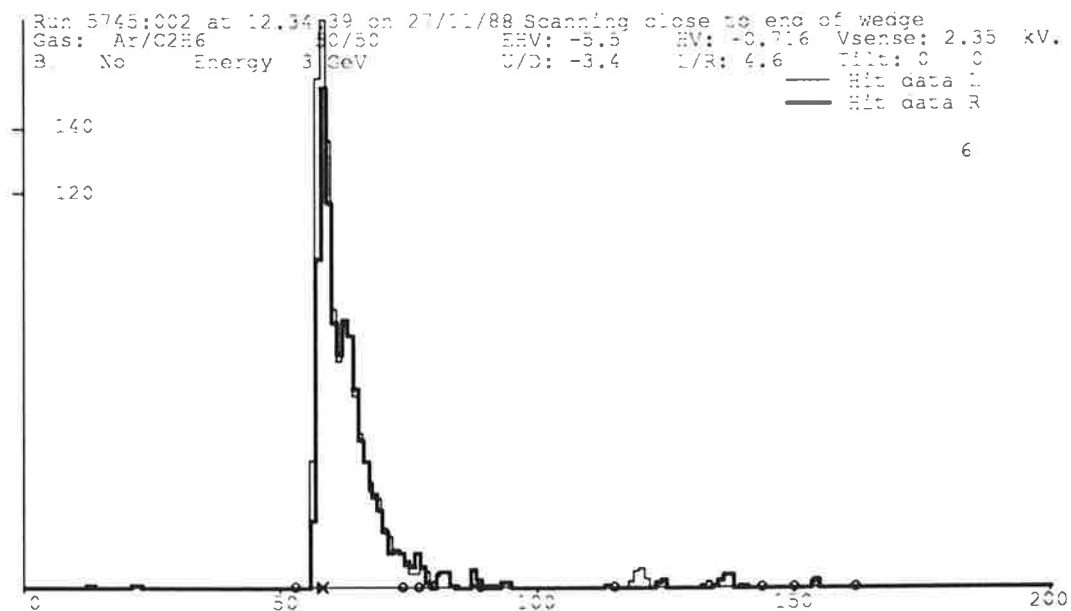


Figure 7.1.2 Example of pulse where the beam spot is near the narrow end of the chamber.

The effect of the resistive wires on the pulse height at each end of the wire for data taken with the third prototype can be seen in the comparison between figures 7.1.1 and 7.1.2. In the former the beam spot is 22.7 cm from the narrow end of the chamber, whereas in the latter the beam spot is only 4.5 cm from the inner radius (right hand end). Here the sense wire is made from 50  $\mu\text{m}$  diameter Stablohm 800, giving a total wire resistance of 390  $\Omega$ , with preamplifiers of 200  $\Omega$  input resistance.

## 7.2 Hub Connection

In order to obviate the need for extensive cabling and electronics around the beam pipe, whilst still allowing the second coordinate determination, it is necessary to inter-connect cells around the beam pipe. Inter-connecting neighbouring cells would allow both halves of a cell pair to contain tracks from the same jet. This would destroy the charge division measurement, because it depends critically on the ability to resolve accurately the charge due to each track (poor resolution within a jet in one cell is tolerable because all the tracks are at the same radius). Transverse momentum balance between jets and leptons means that a 90° connection is desirable in order to minimise the likelihood of overlapping tracks at different positions along the wire pair.

The inter-connection scheme is moreover alternately to the the left and to the right with increasing azimuthal angle  $\phi$  in order to present the most uniform distribution of material around the hub to any particle passing through the FTD. The initial plan for a 90° connection is ruled out because no uniform symmetric 90° connection scheme is possible when the number of inter-connected cells is a multiple of 4; a left-hand end must always be even and a right-hand end odd, or *vice versa*, for the

scheme to be uniform and the cells  $90^\circ$  apart are even-even or odd-odd. The simplest alternative would be either  $90^\circ + 1$  cell or  $90^\circ - 1$  cell. However, as it has already been decided to power the cells in pairs, the chosen connection scheme is  $90^\circ + 1$  cell-pair, or  $105^\circ$ , as illustrated in figure 7.2.1. On considering 'typical' event topologies, this separation means that connected cells are unlikely to be populated with tracks arising from the same interaction.

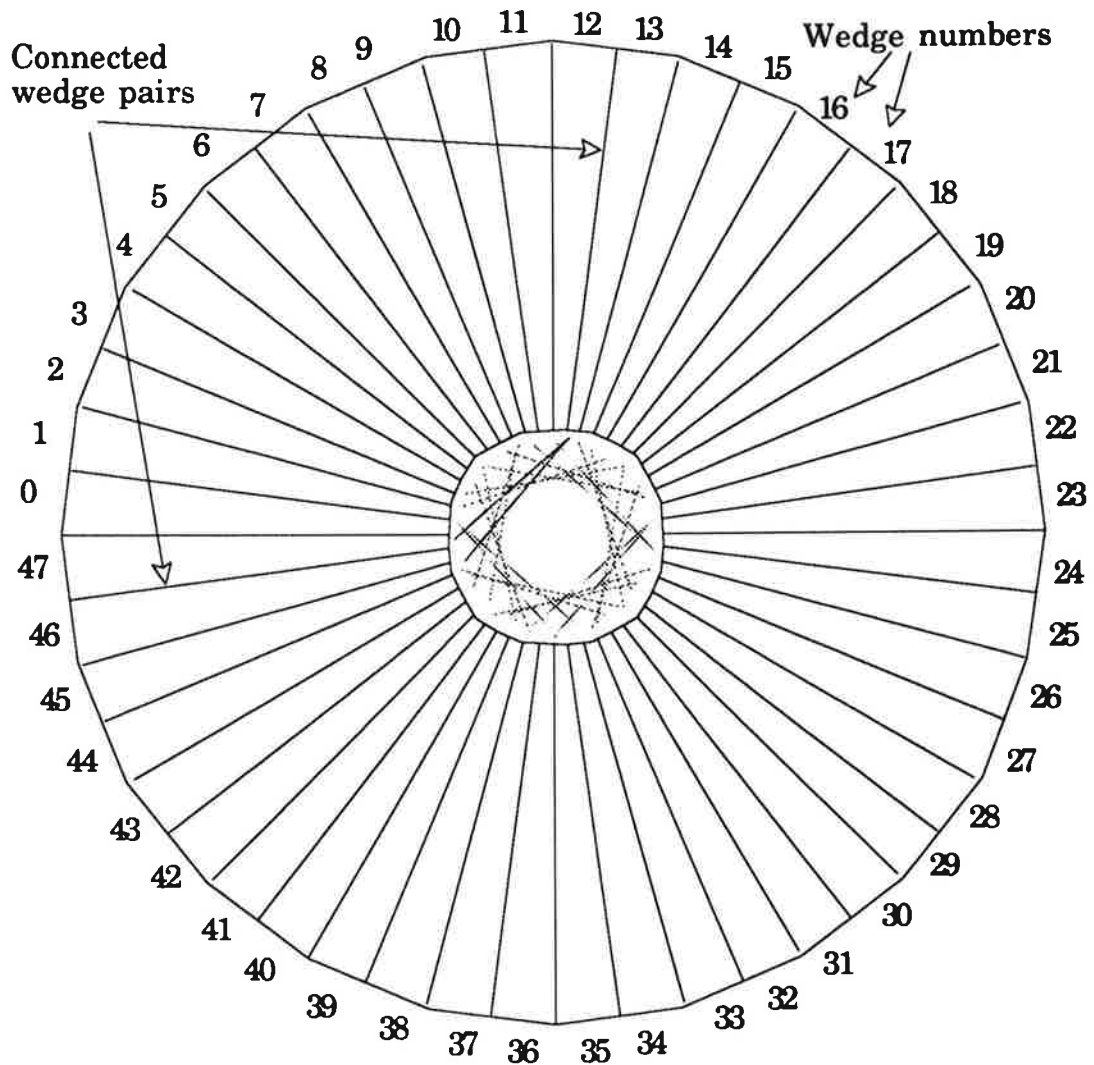


Figure 7.2.1 Layout of the cell inter-connection around hub. The pair of wedges 12 and 13 are connected to wedges 46 and 47. Wedges 2 and 3 are connected to wedges 16 and 17.

Due to the internal geometry of the feedthrough pin and the nature of the pin crimp, there will be about 4 cm of shielded resistive wire between the connected cells, corresponding to a separating resistance of about  $27 \Omega$ . This should be enough to enable the correct identification of which wedge a hit was in, even for tracks very close to the beam pipe, without the need for an additional 'spacer' resistor.

### 7.3 Preamplifier Input Resistance

The sense wires have preamplifiers connected at each end in order to amplify the signal. The magnitude of the input resistance of these preamplifiers modifies the intrinsic accuracy of the charge division measurement, and to some extent the pulse shape seen at each end of the wire. The factors considered relevant for the charge division measurement are outlined below.

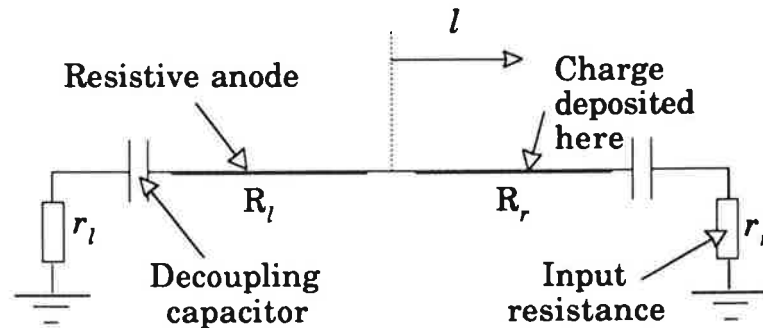


Figure 7.3.1 Diagram of the resistive wire circuit.

If the charges on the left and right ends of the two connected wires of resistance  $R_l$  and  $R_r$  respectively, both with uniform resistance per unit length,  $\rho$ , are  $q_l$  and  $q_r$ , read out through terminating (preamplifier input) resistances  $r_l$  and  $r_r$ , shown schematically in figure 7.3.1, then the distance from the connector between the wires is given by:

$$l_k = \frac{1}{\rho} \left( \frac{q_r (R_r + r_r) - q_l (R_l + r_l)}{q_r + q_l} \right) \quad [7.3.1]$$

Ignoring any difference in resistance between the two wires or the two preamplifiers at each wire end, equation [7.3.1] may be rewritten as:

$$l_k = \frac{R_{total}}{2\rho} \frac{q_r - q_l}{q_r + q_l} \quad [7.3.2]$$

where  $R_{total}$  is the sum of the wire and preamplifier input resistances. To investigate the effect of the preamplifier input resistances on the charge division precision, first consider the derivative of  $l_k$  with respect to  $q_r$ :

$$\frac{dl_k}{dq_r} = \frac{R_{total}}{\rho} \frac{q_l}{(q_r + q_l)^2} \quad [7.3.3]$$

This derivative may be minimised by setting  $r_l$  and  $r_r$  as low as possible. On the other hand, although increasing the input resistance of the preamplifiers reduces the relative variation in pulse height at the end of the wire, this does permit the use of a slightly higher overall gas gain; the gas gain may be increased such that the pulse height at the near end of the wire for a pulse at that end of the wire corresponds to the same level as with the lower input resistance preamplifiers but the total pulse integral is larger. The resultant increase in signal to noise ratio on the smaller pulse along with no degradation in signal to noise on the larger pulse must be offset against having increased the effective "length" of the

wire. Not increasing the gas gain would keep the total pulse integral the same, with the reduction of the larger pulse balancing the increase of the smaller pulse.

Plotted in figure 7.3.2 are the variations in the derivatives  $\frac{dl_k}{dq_r}$  and  $\frac{dl_k}{dq_l}$  for the pulses measured at each end of the wire as a function of where along the wire the initial charge was deposited, evaluated for a wedge wire resistance of  $400 \Omega$  and normalised to a maximum charge at either wire end of one unit. The wires correspond to  $-1 \leq l \leq 0$  and  $0 \leq l \leq 1$ . The main effect of increasing the terminating resistance is to increase the sensitivity of the coordinate measurement to the near (large) pulse, with the sensitivity to the far pulse increasing only slightly with terminating resistance.

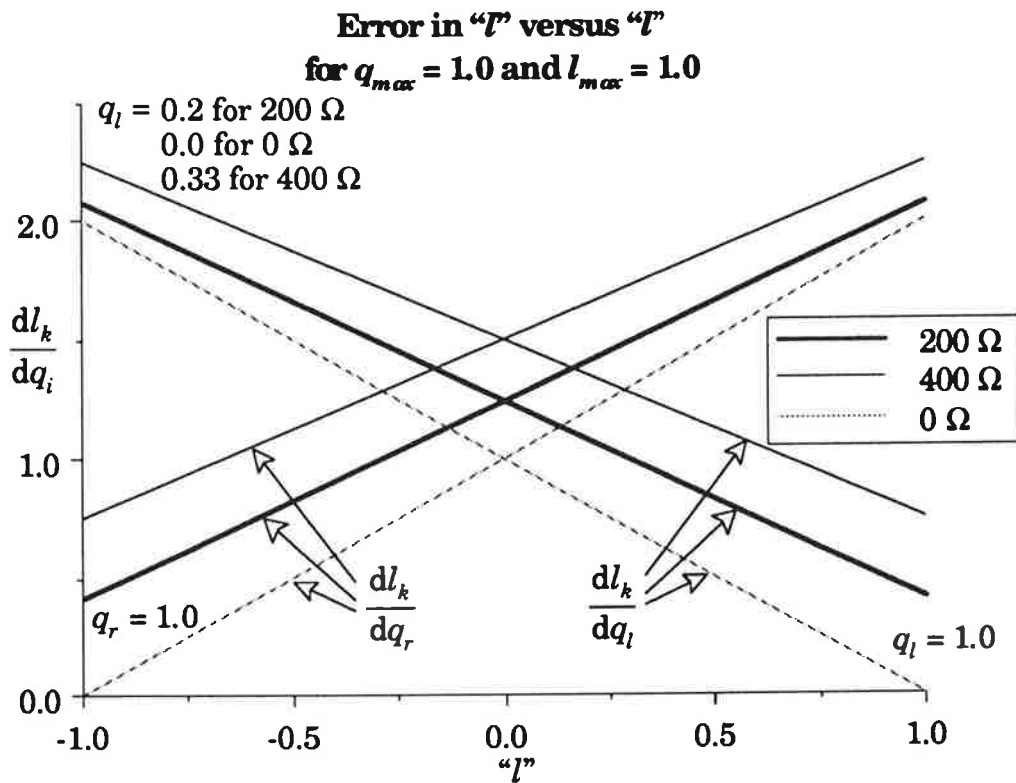


Figure 7.3.2  $\frac{dl_k}{dq}$  versus  $l$  for various preamplifier input resistances.

In figures 7.3.3 and 7.3.4 are shown the mean pulse shapes obtained using 200  $\Omega$  and 390  $\Omega$  input resistance preamplifiers on the first production chamber, for tracks which went through the cell at large radius. The preamplifiers on wires 6 and 7 have 390  $\Omega$  input resistance, those on wires 9 and 10 have 200  $\Omega$ . The slightly slower rising edge and cleaner trailing edge of the “far” pulses for the former are a result of the larger total resistance with the 390  $\Omega$  preamplifiers. The effect of the increased terminating resistance can also be seen in the relative pulse sizes.

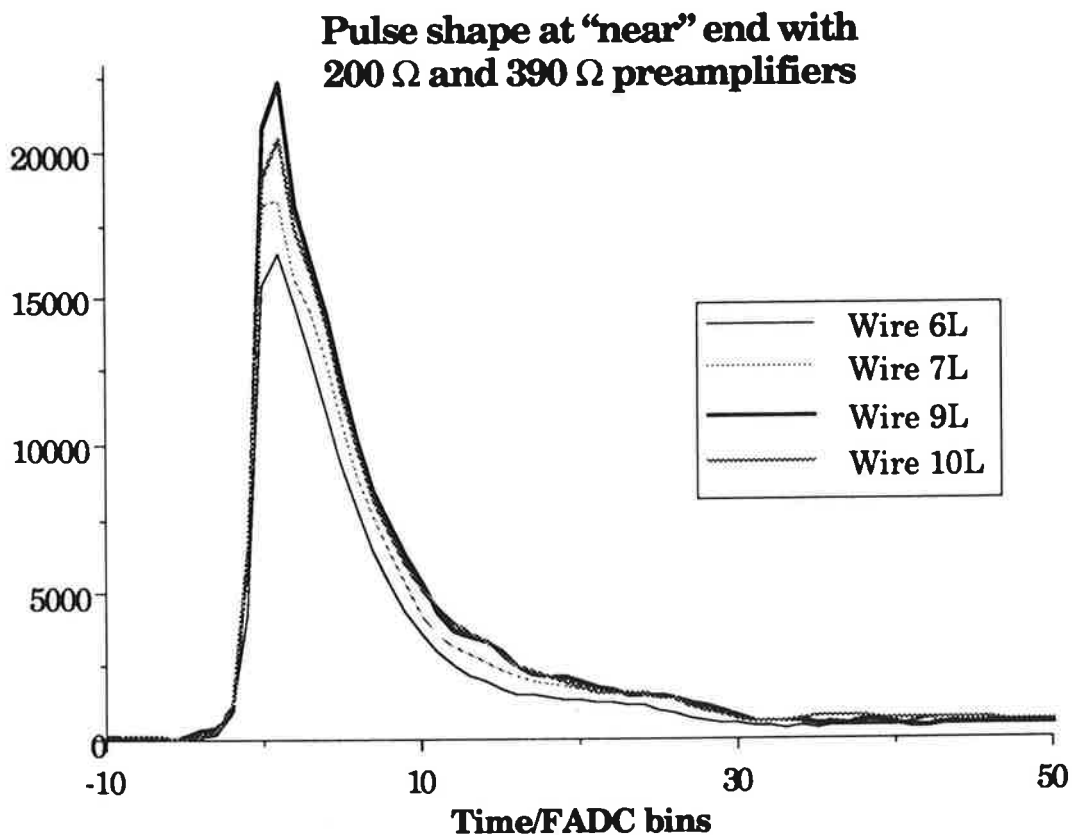


Figure 7.3.3 Mean pulse shapes for the “near” pulse obtained using 200  $\Omega$  and 390  $\Omega$  preamplifiers on the first production chamber.



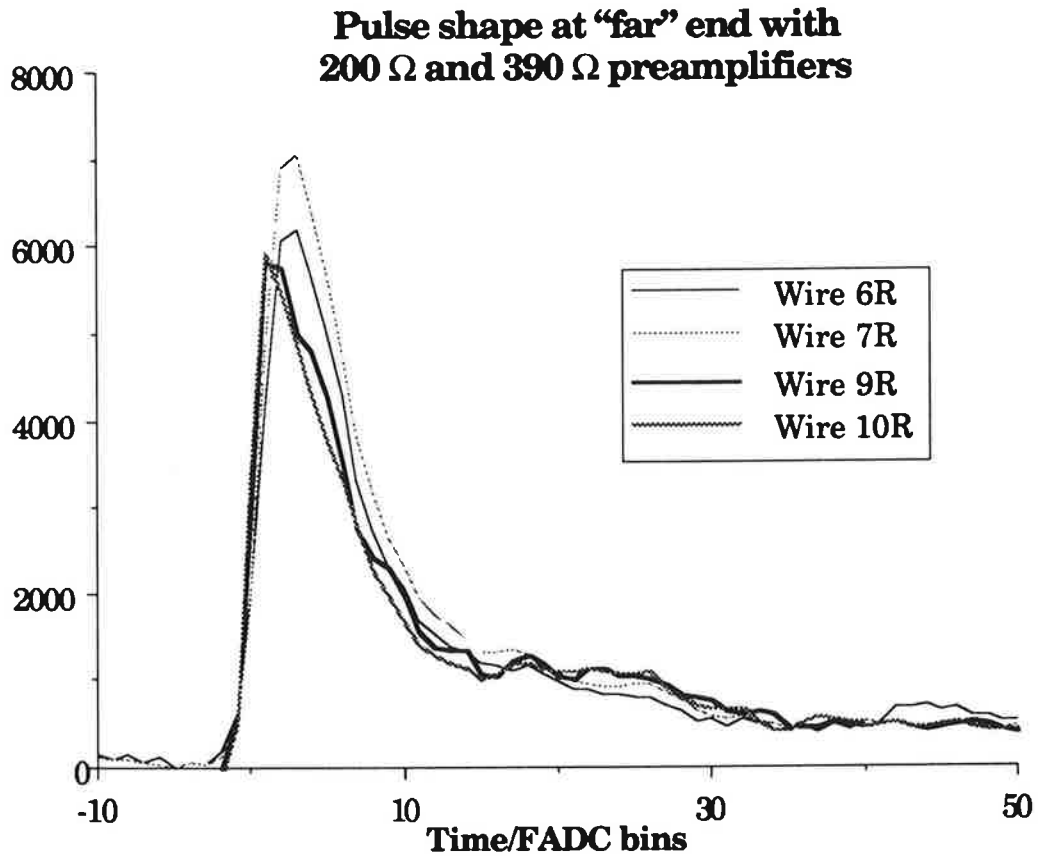


Figure 7.3.4 Mean pulse shapes for the “far” pulse obtained using 200 Ω and 390 Ω preamplifiers on the first production chamber.

Matching the preamplifier to the chamber impedance in order to eliminate signal bounce is unnecessary because of the small spatial extent of the detector in relation to any frequency of interest; even a frequency as high as 50 MHz corresponds to a wavelength of 6 m in free space. Although the “rule of thumb” for charge division<sup>1</sup> gives the following relationship between the optimum total wire resistance,  $R_{total}$ , and the impedance of the anode,  $Z_0$ ,

$$R_{total} = 2\pi Z_0 \quad [7.3.4]$$

the same references also state that the preamplifier input resistance should be as small as possible. Previous results with FADC read-out also suggest that although the precision as a fraction of the total resis-

tance may be improved by increasing the terminating resistor, the precision as a fraction of the wire length is degraded<sup>5</sup>. Results from the original test cell and the first production chamber bear this out.

The final constraint on the minimum total resistance arises from the effect of the pulse shape on the two track resolution; if the total resistance is too low, such that the rise time of the wire is fast, then the effect of signal reflection at each end of the wire may be visible. For the first prototype the wire resistance is about 1510  $\Omega$ , and no bounce is discernible. With the second prototype the total resistance is 1160  $\Omega$ , although the wire resistances are only about 384  $\Omega$ . Again no evidence for reflections are seen. However with the third prototype the total resistance is only 788  $\Omega$ . Here there are in general small secondary peaks in the pulse shape after the main peak, which are detected by the hit finding algorithm. The average DOS pulse shape for data taken 22.7 cm from the inner radius of the chamber likewise shows a noticeable blip on the trailing edge of the pulse profile, as illustrated in figure 7.3.5, with the chamber length of the prototype being 24 cm. This effect would need to be investigated before choosing very low input impedance preamplifiers for the full-scale chambers, as the total wire resistance is about 900  $\Omega$ .

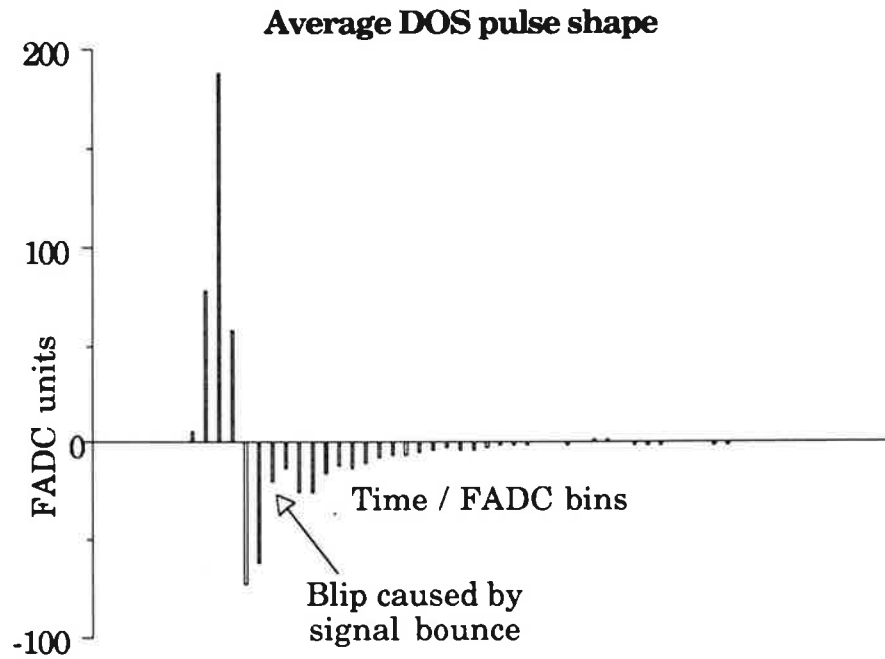
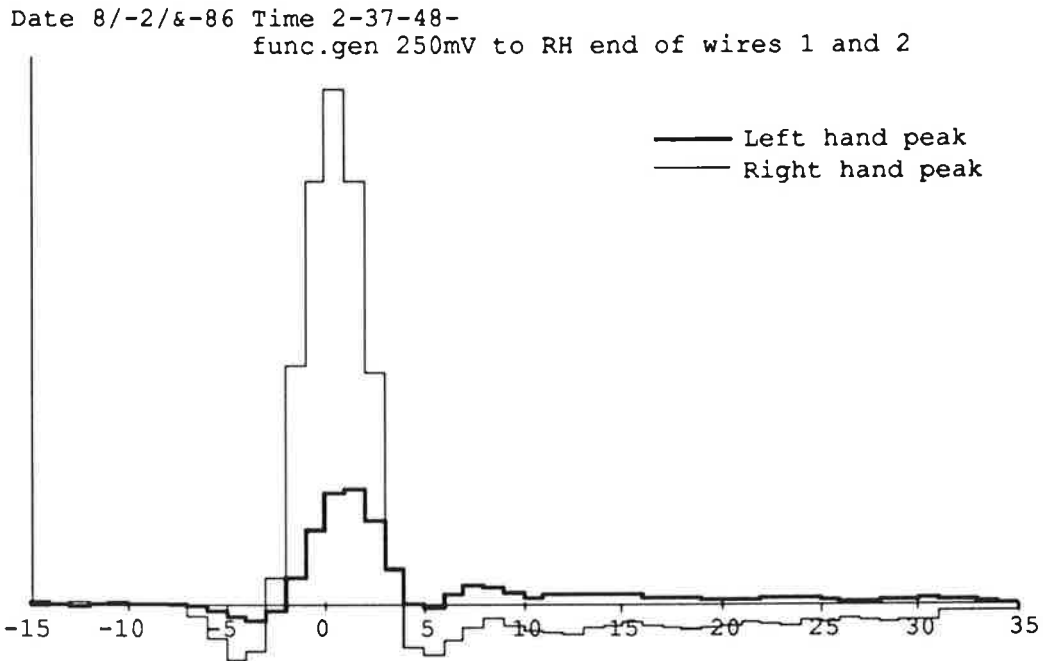


Figure 7.3.5 Average DOS pulse shape for data taken 22.7 cm from inner radius of prototype 3.

## 7.4 Pre-amplifier De-coupling Capacitors

The size of the de-coupling capacitors used to isolate the preamplifiers from the sense wire high voltage supply is also seen to have a significant effect on the observed pulse shape.

With the first prototype, the initial data were characterised by significant signal undershoot on the trailing edge of the larger pulse, when the sense wires were de-coupled from the preamplifiers by 330 pF capacitors. This is illustrated in figure 7.4.1 for test pulses injected at one end of the wire.



**Figure 7.4.1** Mean pulse shape for test pulses injected at one end of the sense wire of the first prototype, when the de-coupling capacitors were 330 pF.

Analysis of a simple theoretical model, which considers only the wire resistance, the terminating resistances and the de-coupling capacitance at each end of the wire and approximates the chamber capacitance by a lumped capacitance to earth localised at the point of charge deposition, predicts two current eigenstates:

- a rapidly decaying 'charge division' current which flows from the injection point, dividing according to the resistance ratio, with a time constant dominated by the wire capacitance;
- a slowly decaying 'loop' current flowing round the wire from the 'near' end toward the 'far' end, with a time constant dominated by the de-coupling capacitances.

These are readily understood in that eventually the charge on the wire must be divided equally between the two de-coupling capacitors. The fast

current is the charge division signal, and the slow current gives rise to the long term equalisation of charge on the de-coupling capacitors. Increasing the capacitors not only reduces the instantaneous “loop” current, by virtue of the increased decay time, but also increases the fraction of charge initially in the “charge division” eigenstate on injection of the charge. This is in good agreement with the observed pulse shapes. More detailed analysis has shown that the ‘error’ in the charge division measurement is proportional to  $\frac{\tau_F}{C_b R_{total}}$ <sup>6</sup>, where  $C_b$  is the de-coupling capacitor and  $\tau_F$  is the charge integration time.

The above arguments lead to the conclusion that the de-coupling capacitance should be large in comparison to the chamber capacitance. Shown in figure 7.4.2 are test pulses taken under the same conditions as for figure 7.4.1, only with the de-coupling capacitance at each wire end increased to 10 nF.

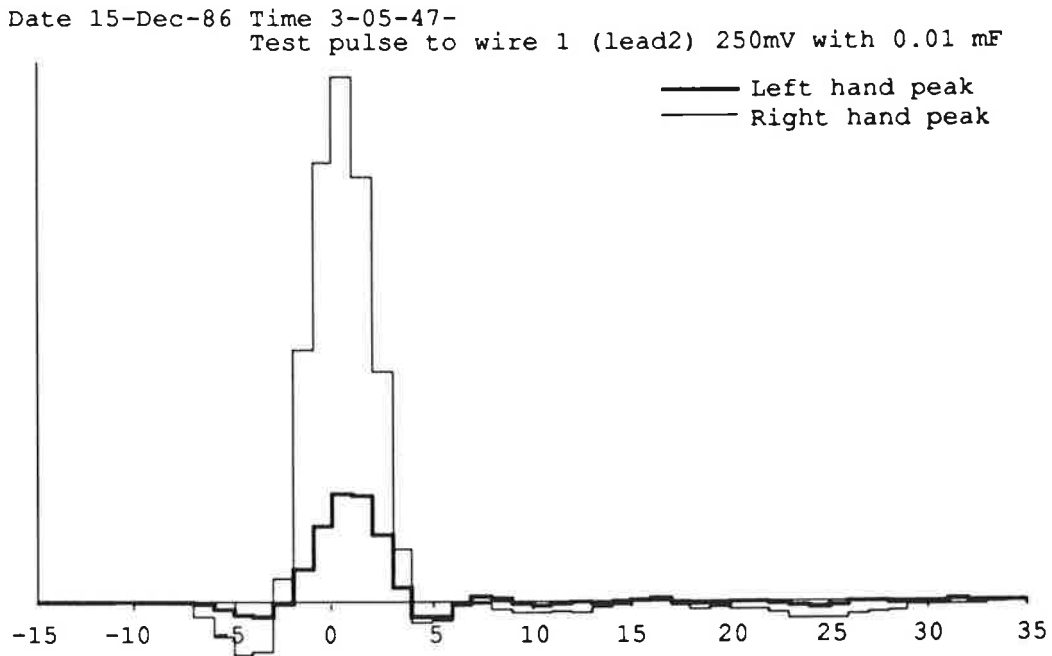


Figure 7.4.2 Mean pulse shape for test pulses injected at one end of the sense wire of the first prototype, when the de-coupling capacitors were 10 nF.

Previous results from measurements in a 4 m streamer tube<sup>7</sup> have moreover shown that a precision of better than 0.1% can be achieved with 5.6 nF capacitors and that there is only marginal improvement on increasing the capacitance above 5 nF, for similar charge integration times and wire resistances to those used in the radial chambers. Space limitations on the preamplifier card and the required breakdown voltage have resulted in the choice of 4.7 nF capacitors rated at 3 kV. However it should be borne in mind that these capacitors will de-rate significantly at the operating sense wire voltage of around 2.3 kV, resulting in a capacitance of around 2 nF.

## 7.5 Region Of Pulse Used To Evaluate The Pulse Integral

For speed the same pulse integral will be exploited for both the  $\frac{dE}{dx}$  measurements and the charge division measurements. Each pulse is integrated for a fixed number of bins, rather than between two threshold values, in order that the integral response remains linear for large pulses. Were the integration interval allowed to vary, then pulses which have a particularly long or high trailing edge would result in an overly large pulse integral.

This integration is performed relative to the integer time bin as defined in chapter 6, starting a fixed number of bins from the bin of maximum DOS in the combined data and integrating the left and right hand read-outs for a fixed number of bins. For the  $\frac{dE}{dx}$  measurements these two integrals are combined after calibration.

With 12 measurements of the radial position at the 12 different  $z$  values of the sense wires a two parameter fit to  $l_k = az_k + b$  can be performed. The residuals from this fit provide a statistically reliable estimator for the radial precision, after correcting for the systematic bias of  $\sqrt{\frac{10}{12}}$ .

The effect of varying the integration interval on the charge division precision is summarised in tables 7.5.1 to 7.5.3 for DL3000 data taken with the third prototype, quoting the results of a bin by bin summation of the pulse.  $\sigma_{\text{mean}}$  is the mean residual of all wires from the above fit, without any wire to wire calibration,  $\sigma_{\text{min}}$  is for the best wire. Three different radial positions are considered, 22.7 - 19.4 cm, 12.1 cm and 4.5 cm from the inner radius. The results with 6 bit FADCs are not detailed here because with the second prototype which was used for the 6 bit FADC measurements the chamber corresponds to only the central  $\frac{1}{3}$  of the total resistance. With the third prototype the chamber corresponds to the central  $\frac{1}{2}$  of the total resistance.

Start bin	Number of bins	$\sigma_{\text{mean}} / \text{cm}$	$\sigma_{\text{min}} / \text{cm}$
-1	7	1.38	0.89
-1	8	1.31	0.83
-1	9	1.29	0.78
-1	10	1.27	0.76
-1	11	1.25	0.75
-1	12	1.15	0.68
-1	13	1.17	0.69
-1	14	1.19	0.69
-1	15	1.28	0.74
-1	16	1.31	0.76

**Table 7.5.1** Charge division precision for various integration ranges for data between 22.7 and 19.4 cm from the inner radius.

Start bin	Number of bins	$\sigma_{\text{mean}} / \text{cm}$	$\sigma_{\text{min}} / \text{cm}$
-1	8	1.32	0.79
-1	9	1.30	0.73
-1	10	1.27	0.71
-1	11	1.23	0.71
-1	12	1.26	0.72
-1	13	1.30	0.73
-1	14	1.31	0.69
-1	15	1.30	0.67
-1	16	1.29	0.66

**Table 7.5.2** Charge division precision for various integration ranges for data 12.1 cm from the inner radius.



Start bin	Number of bins	$\sigma_{\text{mean}} / \text{cm}$	$\sigma_{\text{min}} / \text{cm}$
-1	8	1.10	0.71
-1	9	1.03	0.66
-1	10	1.01	0.65
-1	11	1.04	0.68
-1	12	1.06	0.71
-1	13	1.06	0.71
-1	14	1.05	0.68
-1	15	1.03	0.65
-1	16	1.03	0.66

**Table 7.5.3** Charge division precision for various integration ranges for data 4.6 cm from the inner radius.

The above data show a general improvement in charge division precision as the integration interval is increased, particularly for the data towards the inner radius of the chamber, which corresponds the centre of the wire pair. Notwithstanding this there also tends to be a minimum for an integration interval of around 12 FADC bins. Varying the start of the integration interval relative to the integer time of the pulse produces the results in tables 7.5.4 to 7.5.6.

Start bin	Number of bins	$\sigma_{\text{mean}} / \text{cm}$	$\sigma_{\text{min}} / \text{cm}$
0	12	1.41	0.88
-1	12	1.15	0.68
-2	11	1.15	0.65
-2	12	1.14	0.66
-2	13	1.16	0.65
-3	12	1.15	0.66

**Table 7.5.4** Variation of charge division precision on varying the start of the integration range for data between 22.7 and 19.4 cm from the inner radius.

Start bin	Number of bins	$\sigma_{\text{mean}} / \text{cm}$	$\sigma_{\text{min}} / \text{cm}$
0	12	1.56	0.80
-1	12	1.26	0.72
-2	11	1.11	0.61
-2	12	1.09	0.59
-2	13	1.12	0.59
-3	12	1.11	0.60

**Table 7.5.5** Variation of charge division precision on varying the start of the integration range for data 12.1 cm from the inner radius.

Start bin	Number of bins	$\sigma_{\text{mean}} / \text{cm}$	$\sigma_{\text{min}} / \text{cm}$
0	12	1.24	0.90
-1	12	1.06	0.71
-2	11	0.90	0.59
-2	12	0.92	0.61
-2	13	0.94	0.64
-3	12	0.89	0.59

Table 7.5.6 Variation of charge division precision on varying the start of the integration range for data 4.6 cm from the inner radius.

For data with this chamber the optimum interval is to start 2 bins before the bin corresponding to the integer time of the bin and then continue for 12 FADC bins. The residuals for various radii using this integration interval are summarised in figure 7.5.1.  $\sigma_{\text{mean}}$  is the mean residual of all wires from the fit, without any wire to wire calibration,  $\sigma_{\text{min}}$  is the mean residual for the best wire. The statistical error on each of the data points is  $\sim 0.01$  cm.

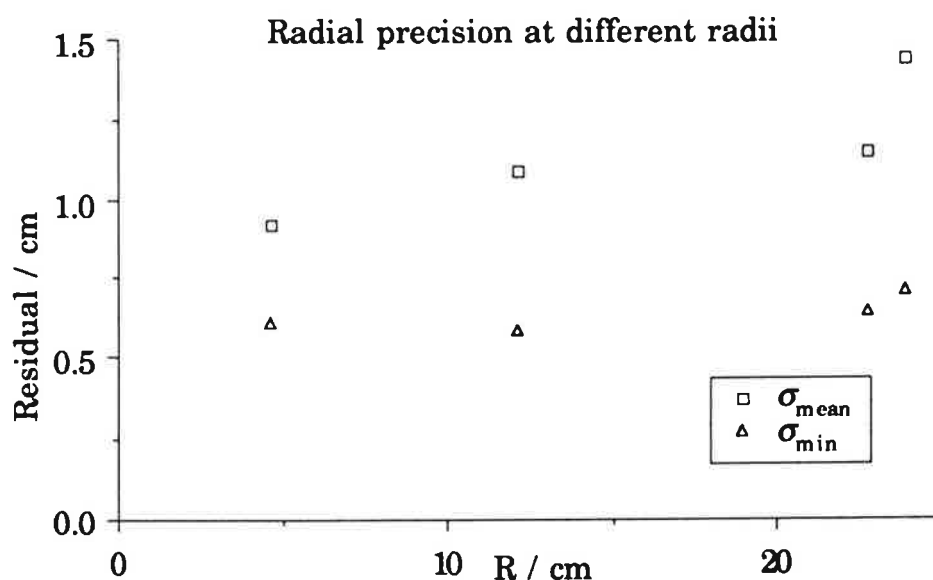


Figure 7.5.1 Radial residuals for various radii.

The residuals for the best wire are flat from the inner radius out to right next to the outer field former, whereas the mean residual tends to increase with radius. These results include no calibration of the individual preamplifier gains or input resistances other than a correction for a defective channel on one of the preamplifiers. The effect of these calibrations would be expected to be greatest at large radius, and indeed this is consistent with the trend in the mean residuals.

## **7.6 Methods Used To Evaluate The Pulse Integral**

For accurate charge division measurements not only must the FADC pulse integral be well defined, but also the estimate of the underlying pedestal must be accurate. The pedestal is estimated for the DL300 data by taking the average of all bins preceding the region of the first pulse on that wire. The effects discussed in sections 7.3 and 7.4 above result in the base line after the pulse being shifted. Therefore no reference is made to data in this region. For the DL3000 data the pedestal is assumed to be zero, instead relying on the inductive de-coupling.

In all, four different pulse integration algorithms have been implemented; bin by bin summation, trapezium rule integration, Simpson's rule integration and pulse shape fitting to either the combined left and right hand read-outs or to a standard pulse, using the drift time correction to calculate an interpolated pulse shape. Each method is out-lined below, along with the resulting precision for the same DL3000 data as above.

### 7.6.1 Bin By Bin Summation

The pulse integral is simply taken to be the summation of the bins in the specified region, giving the integral shown shaded in figure 7.6.1. The results using this method are summarised in tables 7.5.1 to 7.5.6 above.

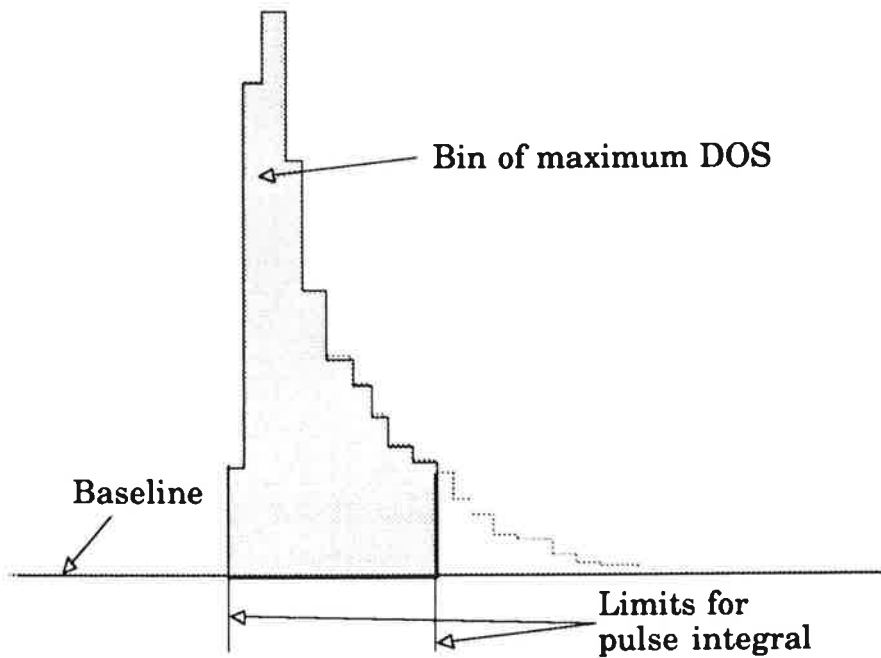


Figure 7.6.1 Illustration of bin by bin summation.

### 7.6.2 Trapezium Rule Integration

Various algorithms exist for producing a better estimate of an integral where the values of the function are known at equi-distant points. The simplest of these is the trapezium rule, which gives the integral shown shaded in figure 7.6.2. The results are summarised in table 7.6.1.

Radius	Start bin	Number of bins	$\sigma_{\text{mean}} / \text{cm}$	$\sigma_{\text{min}} / \text{cm}$
22.7	-1	12	1.29	0.76
12.1	-1	12	1.31	0.71
4.6	-1	12	1.10	0.71
22.7	-2	12	1.18	0.69
12.1	-2	12	1.15	0.64
4.6	-2	12	0.94	0.61

Table 7.6.1 Charge division precision for various integration ranges using trapezium rule integration.

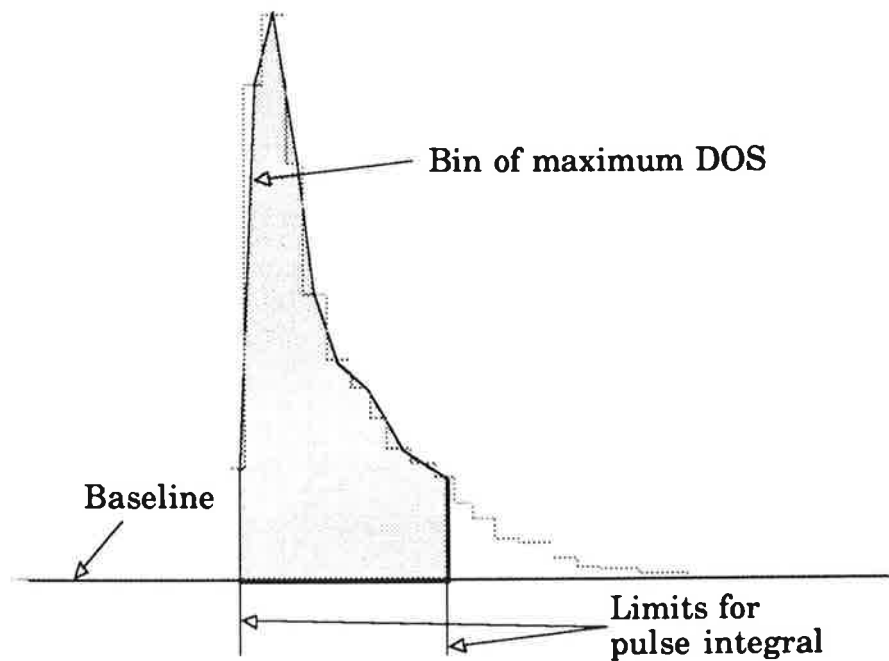


Figure 7.6.2 Description of trapezium rule integration

### 7.6.3 Simpson's Rule Integration

A second alternative, for an even integration interval, uses Simpson's rule based on quadratic interpolation. The results are summarised in table 7.6.2.

Radius	Start bin	Number of bins	$\sigma_{\text{mean}} / \text{cm}$	$\sigma_{\text{min}} / \text{cm}$
22.7	-1	12	1.35	0.84
12.1	-1	12	1.41	0.78
4.6	-1	12	1.16	0.76
22.7	-2	12	1.18	0.68
12.1	-2	12	1.14	0.65
4.6	-2	12	0.97	0.65

Table 7.6.2 Charge division precision for various integration ranges using Simpson's rule integration.

#### 7.6.4 Pulse Shape Fitting

The fourth technique adopted performs a least squares fit of the observed pulse shape at each wire end to either the sum of the individual pulses or to a standard pulse. The standard pulse was created on an event by event basis by linearly interpolating the average pulse shape from a number of runs, making use of the timing correction to the integer time from chapter 6. The results from fitting the individual pulses to the sum and to the standard pulse are summarised in table 7.6.3 and table 7.6.4 respectively.

Radius	Start bin	Number of bins	$\sigma_{\text{mean}} / \text{cm}$	$\sigma_{\text{min}} / \text{cm}$
22.7	-1	12	1.19	0.70
12.1	-1	12	1.28	0.72
4.6	-1	12	1.21	0.79
22.7	-2	12	1.16	0.69
12.1	-2	12	1.24	0.69
4.6	-2	12	1.18	0.78

Table 7.6.3 Charge division precision for various integration ranges fitting to summed pulse.

Radius	Start bin	Number of bins	$\sigma_{\text{mean}} / \text{cm}$	$\sigma_{\text{min}} / \text{cm}$
22.7	-1	12	1.32	0.80
12.1	-1	12	1.44	0.78
4.6	-1	12	1.22	0.74
22.7	-2	12	1.31	0.79
12.1	-2	12	1.42	0.77
4.6	-2	12	1.20	0.73

Table 7.6.3 Charge division precision for various integration ranges fitting to standard pulse.

## 7.7 Conclusions

Although various techniques have been tried which in principle should result in improved integration of the chamber pulses, it transpires that the best precision is obtained with the simplest method adopted. With a simple bin by bin summation, a minimum radial precision of about 0.7 cm is achievable over the full length of the test cell, using 8 bit FADCs. The total length of the wires of the connected cells is 57.9 cm, with a combined wire resistance of 388  $\Omega$  and preamplifiers with 200  $\Omega$



input impedance. This gives the minimum charge division precision as 0.6% of the total resistance of 788  $\Omega$ . With the 450  $\Omega$  resistance wires in the full size chambers and the same 200  $\Omega$  preamplifiers this corresponds to a minimum radial precision of 1.2 cm. The results with 6 bit FADCs are slightly worse, corresponding to a charge division precision of just over 0.7% of the total resistance of 1160  $\Omega$ .

---

- 1** V Radeka and P Rehak, IEEE Trans. Nuc. Sci. NS-26 (1979) 225
- 2** V Radeka, IEEE Trans. Nuc. Sci. NS-21 (1974) 51
- 3** California Fine Wire Company, Grover City, Ca., USA
- 4** Goodfellow Metals Ltd, Cambridge, UK
- 5** M Zimmer, Messung der Signalladung und der Ladungsteilung an langen Zähldrähten mit FADC-Auslese, Diplomarbeit, Heidelberg (1985)
- 6** J L Alberi and V Radeka, IEEE Trans. Nuc. Sci. NS-23 (1976) 251
- 7** S F Biagi and P S L Booth, NIM A252 (1986) 586

# Chapter 8:

## Energy Loss Measurements And Particle Identification.

### 8.1 Introduction

For each track passing through the FTD, the radial chambers will measure the primary particle's specific energy loss  $\left(\frac{dE}{dx}\right)$  along with any transition radiation (TR) emitted in passing through the stacks of TR foils. The planar chambers will also measure the primary particle's  $\frac{dE}{dx}$ . This information will be used to complement the particle identification provided by the calorimetric measurements. Tracks which pass through the whole forward tracker ( $7^\circ \leq \theta < 17^\circ$ ) provide up to 72  $\frac{dE}{dx}$  measurements, 36 measurements in the radials and 36 in the planars.

Although the separate contributions from  $\frac{dE}{dx}$  and TR will not in general be resolved in the radial chambers, it makes sense to treat the two effects separately. The techniques used to interpret and analyse the  $\frac{dE}{dx}$  measurements will be discussed first, then their application to the TR data.

### 8.2 $\frac{dE}{dx}$ Measurements

#### 8.2.1 Introduction

The primary particle's specific energy loss forms the basis of the  $\frac{dE}{dx}$  measurements for the particle identification in the FTD and the major source of background for the transition radiation detection. Below 60 GeV the only particles to produce significant TR will be electrons, and in any case the mean number of TR photons absorbed in each radial

chamber for an incident electron will be just greater than one per track. Thus even with a radiating particle the major part of the measured signal arises from the  $\frac{dE}{dx}$ .

## 8.2.2 Overview Of Energy Loss Measurements

When a charged particle passes through matter it loses energy by the interaction of its electromagnetic field with the electrons in the medium. The resultant incoherent Coulomb scattering causes excitation and ionisation of the medium. The small number of discrete primary interactions, typically around 30 primary ionisations in 1 cm of argon at atmospheric pressure, means that the energy loss is statistics dominated. This results in a very broad energy loss distribution, consisting of an asymmetric peak followed by a long high energy tail. The long tail in the distribution is essentially only sensitive to the particle velocity, so for relativistic particles the identification is derived mainly from the most probable value. The integrated charge distribution obtained for 5 GeV electrons using 1 cm of a xenon based gas is illustrated in figure 8.2.1, this being the dependent quantity that can be measured. It is customary to parametrise this with a Landau curve<sup>1</sup>, shown fitted in the figure, although the base assumptions in the Landau theory do not hold in particular for 1 cm samples of a gaseous detector<sup>2</sup>. The theory in general predicts a narrower distribution than the fit shown.

The result of the interaction between the incoming charged particle and the atomic electrons is that the 'struck' atom or molecule is left in an electronically excited state. If, however, sufficient energy is transferred then the atom may be ionised. For thin gas samples the atomic binding of the electrons has a significant effect on the energy loss distribution. In general the mode of the energy loss distribution is dominated by the

'soft' low energy excitations. These primary ionisations result in sufficiently energetic electrons for further secondary ionisation to occur. In argon at atmospheric pressure this results in a total of about 90 electrons in 1 cm of gas for a minimum ionising particle. It is the amplified signal derived from this total ionisation that is measured, rather than the initial primary ionisation.

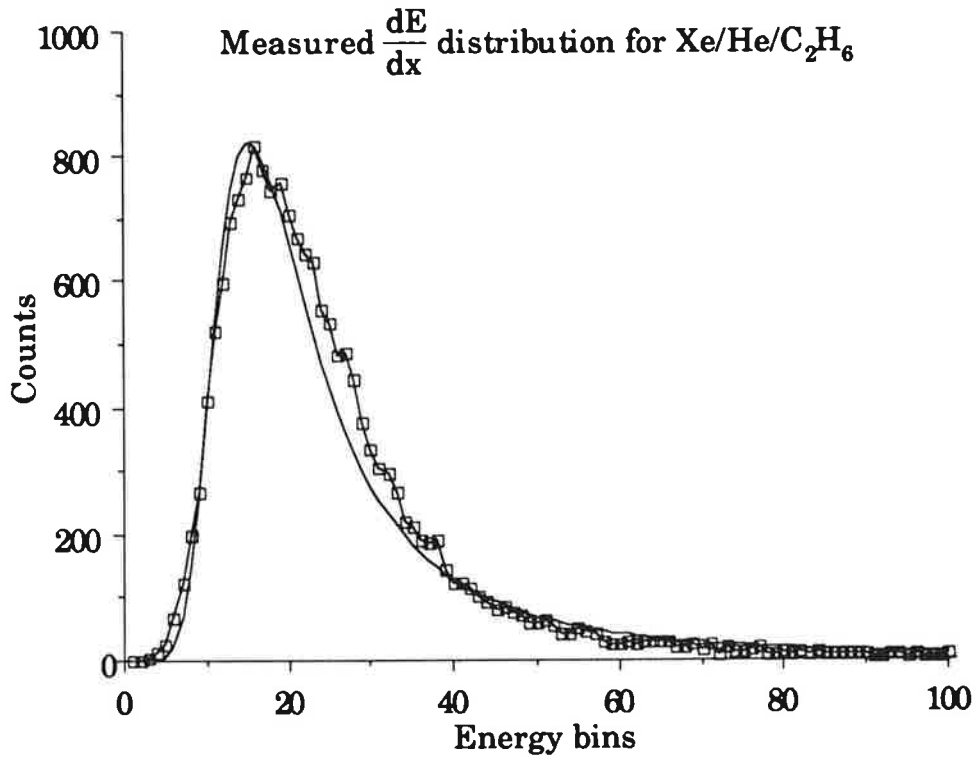


Figure 8.2.1 Measured total charge distribution on a single wire for Xe/He/C<sub>2</sub>H<sub>6</sub> 30/40/30.

For a heavy charged particle the restricted mean energy loss per unit length of medium is given within the framework of relativistic quantum mechanics by the Bethe-Bloch formula<sup>3</sup>:

$$\left(\frac{dE}{dx}\right)_{\leq E_m} = \frac{1}{8\pi\epsilon_0^2} \frac{Z_i^2 e^4}{m c^2 \beta^2} \frac{N_A \rho Z}{A} \left\{ \ln \left( \frac{2m c^2 \beta^2 \gamma^2 E_m'}{I^2} \right) - 2\beta^2 - \delta \right\} \quad [8.2.1]$$

where  $N_A$  is the Avogadro number,  $\rho$  the density,  $Z$  and  $A$  the atomic number and atomic weight of the material,  $m$  the electron mass,  $Z_i e$  is

the incident particle charge and  $\beta c$  is its velocity. The term  $\delta$  represents a 'density correction'<sup>4</sup>, taking into account the polarisation of the medium.  $I$  is the mean excitation potential of the medium and  $E'_m$  is the maximum energy loss in a single collision to contribute to the mean. The form of the mean energy loss as a function of  $\frac{P}{\mu c} = \beta\gamma$  of the incident particle is shown in figure 8.2.2 for argon and in figure 8.2.3 for xenon.

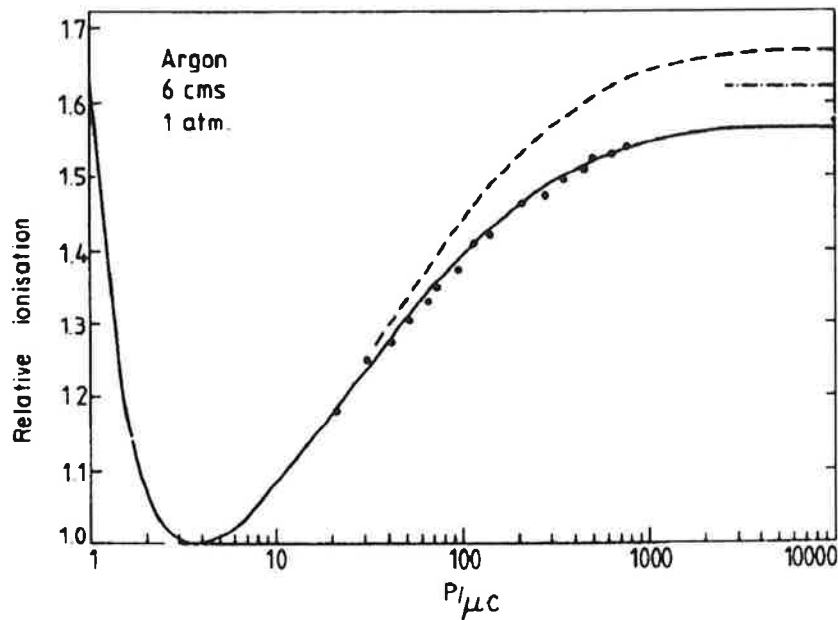


Figure 8.2.2 Mean  $\frac{dE}{dx}$  as a function of  $\beta\gamma$  for argon. The solid curve was calculated using the PAI model described in the reference, the dashed and dot-dashed curves using earlier models<sup>5</sup>.

At low values of  $\beta\gamma$  the  $\frac{1}{\beta^2}$  factor dominates, leading to a rapid decrease until the minimum is reached around  $\beta\gamma = 4$ ; hence the term "minimum ionising particle". Above this value the logarithmic term leads to a slow increase, known as the region of relativistic rise. In dense media the dielectric polarisation of the medium alters the electromagnetic fields due to the particle from their free space values toward those characteristic of macroscopic fields in the medium. These polarisation effects cause saturation at extreme values of  $\beta\gamma$ , resulting in a plateau above  $\beta\gamma = 1000$ ,

known as the Fermi plateau. Of the particles passing through the FTD, pions will be in the region of relativistic rise whereas electrons will be on the plateau.

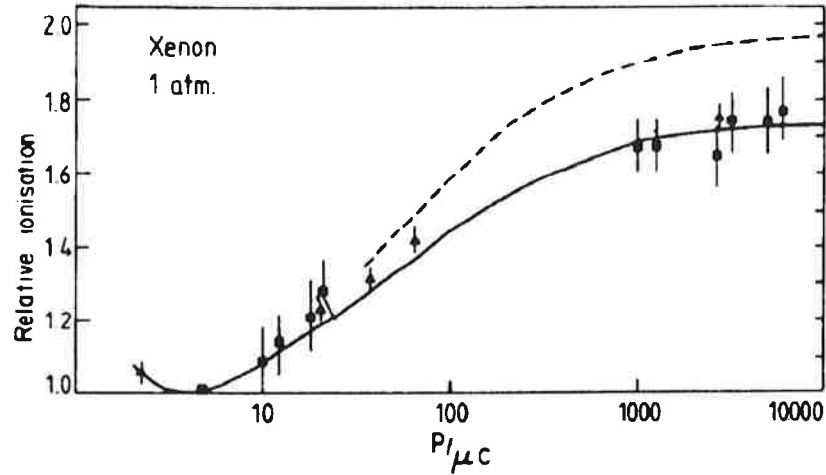


Figure 8.2.3 Mean  $\frac{dE}{dx}$  as a function of  $\beta\gamma$  for xenon<sup>5</sup>.

The long tail at high specific energy loss in the energy loss distribution arises from the finite probability of the incident particle undergoing a 'hard' collision with an atomic electron, resulting in significant energy transfer to the struck electron, namely the production of a  $\delta$  ray. This is adequately described for energy transfers greater than the binding energy of the atoms by the Rutherford cross-section for elastic scattering;

$$\frac{d\sigma}{dE'} = \frac{1}{8\pi\epsilon_0^2} \frac{Z_i^2 e^4}{m c^2 \beta^2} \frac{1}{E'^2} \quad [8.2.2]$$

where  $E'$  is the energy transfer. The dependence solely on velocity of the incident particle, as  $\frac{1}{\beta^2}$ , illustrates the relative insensitivity of  $\delta$  ray production to the incident relativistic particle.

### 8.2.3 Factors Influencing The $\frac{dE}{dx}$ Measurements

The effect of the  $\pm 200 \mu\text{m}$  staggering of the sense wires can be seen in the analysis of test data from the second prototype where the beam traversed the chamber on one side of the wire plane (figure 8.2.4). The mean pulse

height alternates from wire to wire as qualitatively predicted by the simulation; the wires staggered towards the particle track collect ionisation from a 12% longer section of track than those staggered away from the track. This effect is more pronounced in the third prototype, where the sense wire stagger is 300  $\mu\text{m}$  and data is available on both sides of the wire plane (figure 8.2.5).

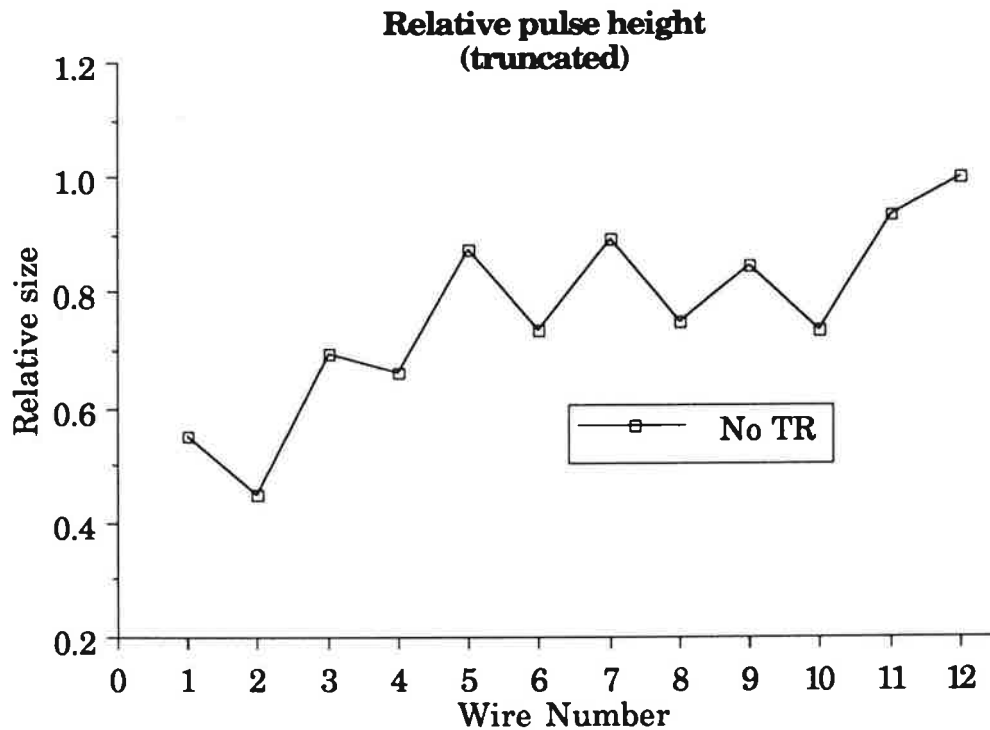


Figure 8.2.4 Plot of mean truncated pulse integral versus wire number, with 200  $\mu\text{m}$  wire stagger.

This odd even asymmetry stresses the importance of the length of particle track contributing to the  $\frac{dE}{dx}$  measurement; the increased track length for tilted tracks will need to be explicitly taken into account for the particle identification. In general this may be achieved by multiplying the measured charge by  $\cos\theta \times \cos\phi$  where  $\theta$  is the angle of the track relative to the  $z$  axis and  $\phi$  is the angle of the track relative to the wire plane.

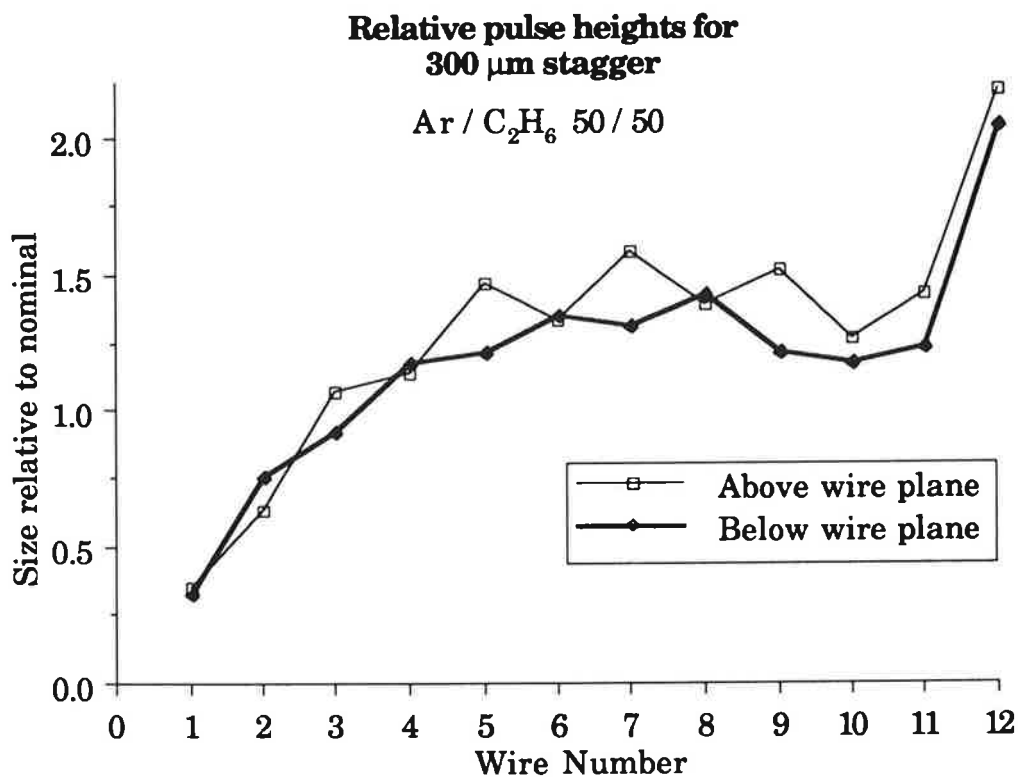


Figure 8.2.5 Plot of mean truncated pulse integral versus wire number for data on either side of the wire plane, with 300  $\mu\text{m}$  wire stagger.

The individual wire gain variation from the front to the back of the cell is however larger than the effects introduced by the sense wire stagger, and is therefore a large source of systematic error. Figure 8.2.6 shows the mean truncated pulse integral versus wire number for four different sets of data taken with the second prototype, for sets of runs with and without a TR radiator in front of the chamber. Fortunately although the wire to wire variation is large, it is stable.



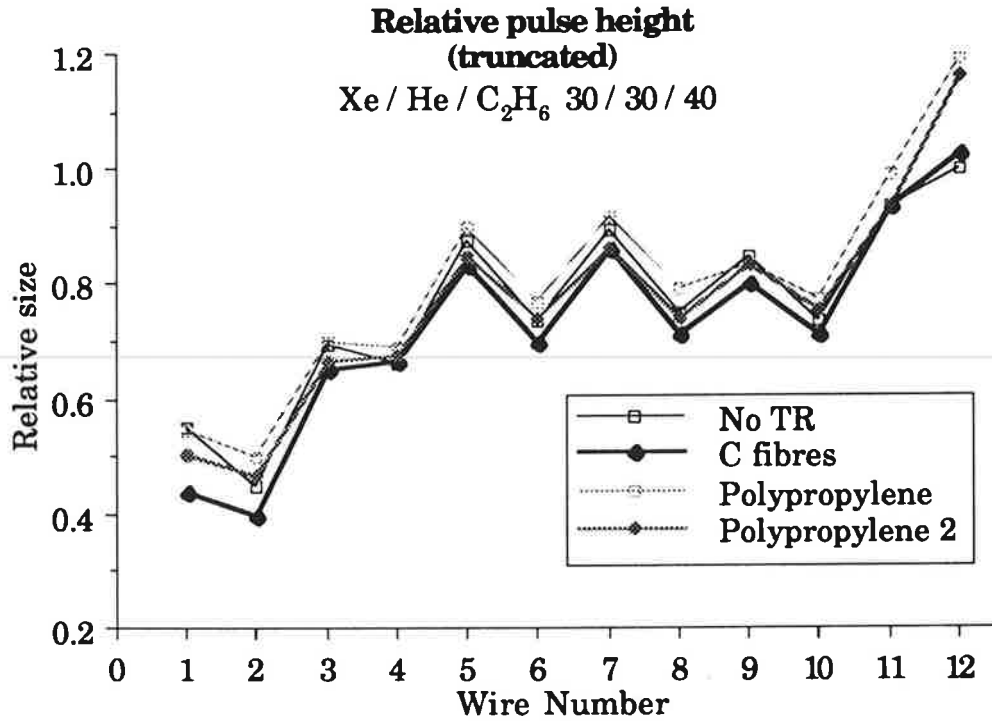


Figure 8.2.6 Xe/He/C<sub>2</sub>H<sub>6</sub> wire to wire gain variation.

More serious is the variation of gain with pressure and temperature; the gain variation with pressure is given by<sup>6</sup>:

$$\frac{\ln(G)}{K} = \Psi\left(\frac{E_a}{P}\right) \quad [8.2.3]$$

where  $G$  is the gain,  $K$  is a constant of proportionality and  $\Psi$  is a function of  $\frac{E_a}{P}$  where  $E_a$  is the electric field at the surface of the anode and  $P$  is the pressure. For small variations in gain this may be approximated by:

$$\frac{\Delta G}{G} = -\alpha \frac{\Delta P}{P} \quad [8.2.4]$$

The observed gain variation for a set of 25 consecutive runs taken without altering any of the chamber settings over a period of 100 minutes is shown in figure 8.2.7. Atmospheric pressure was monitored during these runs, and is also indicated on this graph. These give a value of  $\alpha$  of  $\alpha = 12.5$ .

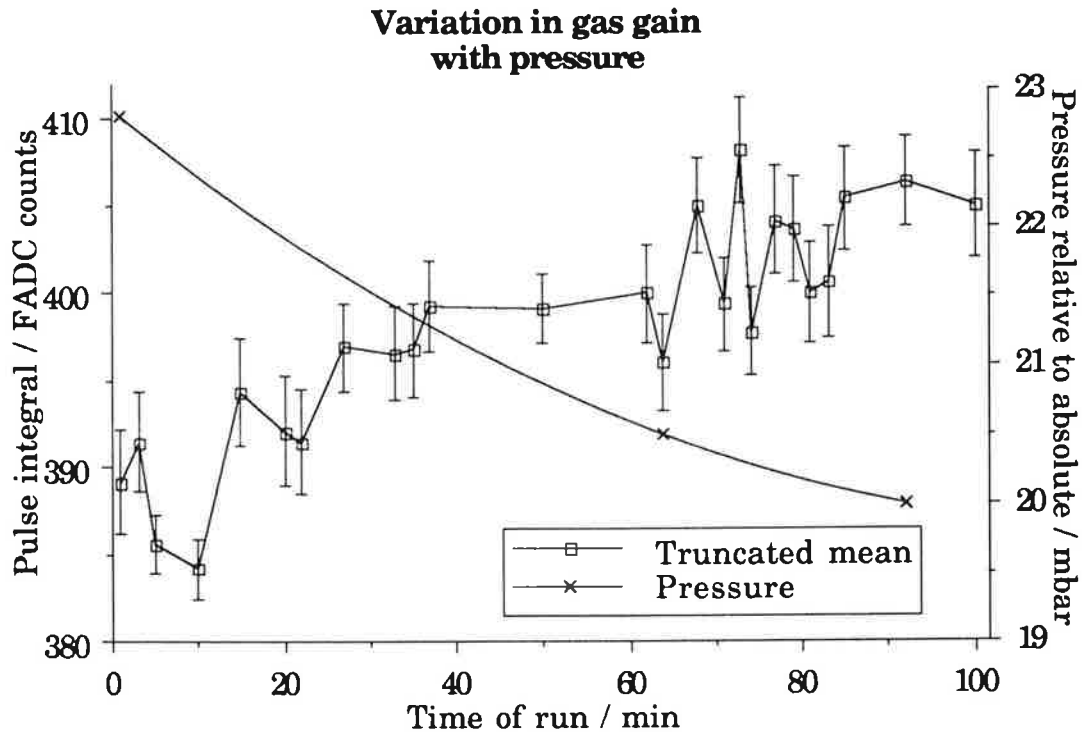


Figure 8.2.7 Gain variation with pressure.

As the FTD in H1 will follow atmospheric pressure, this effect will cause gross variations in gas gain. Assuming the validity of equation 8.2.4 will allow the recovery of the  $\frac{dE}{dx}$  measurements, although the residual systematic effects will probably severely compromise the particle resolution. The reason the chambers follow atmospheric pressure is to easily permit the maintenance of the very small ( $\sim 50 \mu\text{bar}$ ) pressure difference between each individual element of the FTD; if the chambers were operated at an absolute pressure then these very small relative over-pressures would be extremely difficult to achieve.

## 8.2.4 Calibration

The intention is not to measure X-ray photons accurately, but rather to measure ionising tracks. The most direct way of calibrating the gain for tracks is to investigate samples of ionising particles. X-rays, whose absorption is localised, are not affected by the variation in cell width and

therefore do not form a suitable basis for calibration. This of course has irreducible consequences for the X-ray detection algorithms, as the X-ray energy deposition does not depend on the wire stagger, whereas the  $\frac{dE}{dx}$  energy deposition does. However the residual effect of the wire stagger after calibration for the wire to wire variation is at most  $\pm 20\%$  and the X-ray algorithms aim to detect the presence of a TR photon, rather than its magnitude. As the calibration method forms an integral part of the  $\frac{dE}{dx}$  measurement it is detailed in the following section.

### **8.2.5 Analysis Technique Adopted: The Truncated Mean Boot Strap**

The aim of the  $\frac{dE}{dx}$  analysis is primarily to define a stable method which produces consistent results irrespective of whether there were any TR photons. With the test beam data all the data are electrons on the Fermi plateau, simplifying the task of identifying a stable algorithm. The nature of the TR photon spectrum and their absorption cross-section particularly with an argon based gas means that although the photons are predominantly absorbed toward the front of the chamber there is still a sizeable probability of X-ray absorption even on the rearmost wire. As the energy of any absorbed X-ray is large compared to the typical specific energy loss and the large specific energy losses are anyhow relatively insensitive to the particle  $\beta\gamma$ , investigating the smallest observed pulses in each event not only concentrates on those specific energy losses containing the most information, but also filters out the effect of the TR, leading to an independent particle discriminant.

Precise calibration forms a central part of the  $\frac{dE}{dx}$  analysis. The technique implemented relies on multiple passes through the data in order to self-calibrate the track data. For each event in a single radial cham-

ber, the observed calibrated pulse integrals, corrected for track angle and pressure variation as above, are sorted by size. Having excluded the largest 5 pulses out of a maximum 12, the mean of the remainder is taken to give a truncated mean  $\frac{dE}{dx}$ ; alternatively for a maximum likelihood analysis the remainder could be histogrammed with respect to their sorted order. Each of these remaining small pulses is also histogrammed on a wire by wire basis, with separate histograms depending on the resolved left/right ambiguity, to form the basis for updating the calibration. Due to the degree of truncation all these histograms are Gaussian in shape, by central limit, and the mean of a Gaussian fit to each pulse integral is used to update the existing calibration for each wire, with a separate parameter for tracks on each side of the wire plane for each wire. The observed spectrum for a single wire and for the truncated mean over all wires is shown in figure 8.2.8, along with Gaussian fits. These calibration parameters are calculated by starting with initial values of the 24 parameters and then iterating the above procedure using the measured means to update the calibration parameters.

The stability of these calibration parameters and the distribution of wires contributing to the  $\frac{dE}{dx}$  measurements are good indicators of the uniformity of operation of the chamber; the implicit assumption made is that the spectra for the individual wires only differ by a constant of proportionality. If this is not the case then the calibration parameter for the affected wire will tend to be unstable and the frequency of contribution to the truncated mean will also differ from the other wires. Depicted in figure 8.2.9 is the frequency distribution for each wire to have contributed to the  $\frac{dE}{dx}$  measurement. This is reasonably flat.

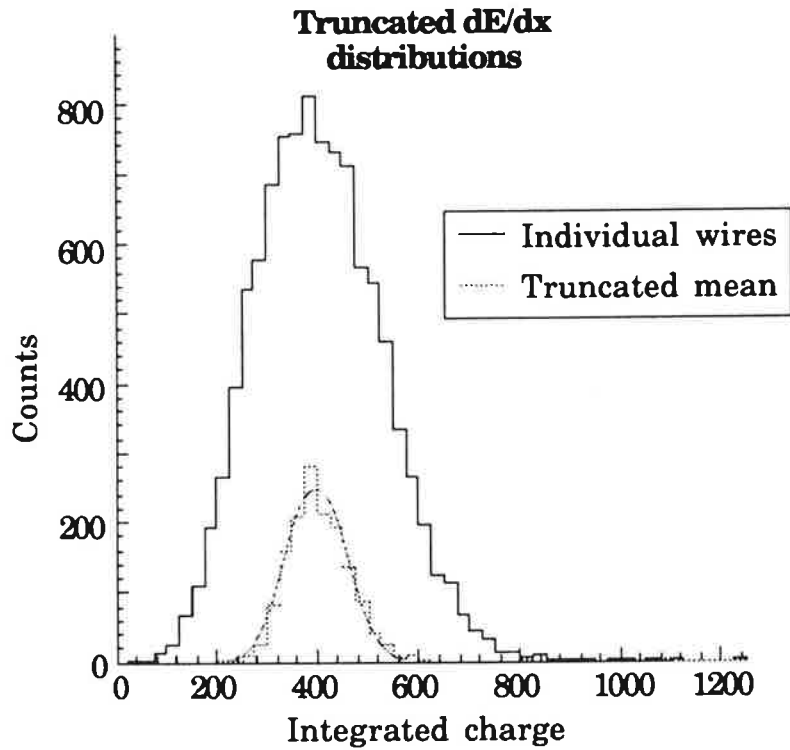


Figure 8.2.8 Truncated pulse integral spectrum for an individual wire and truncated mean spectrum of all wires.

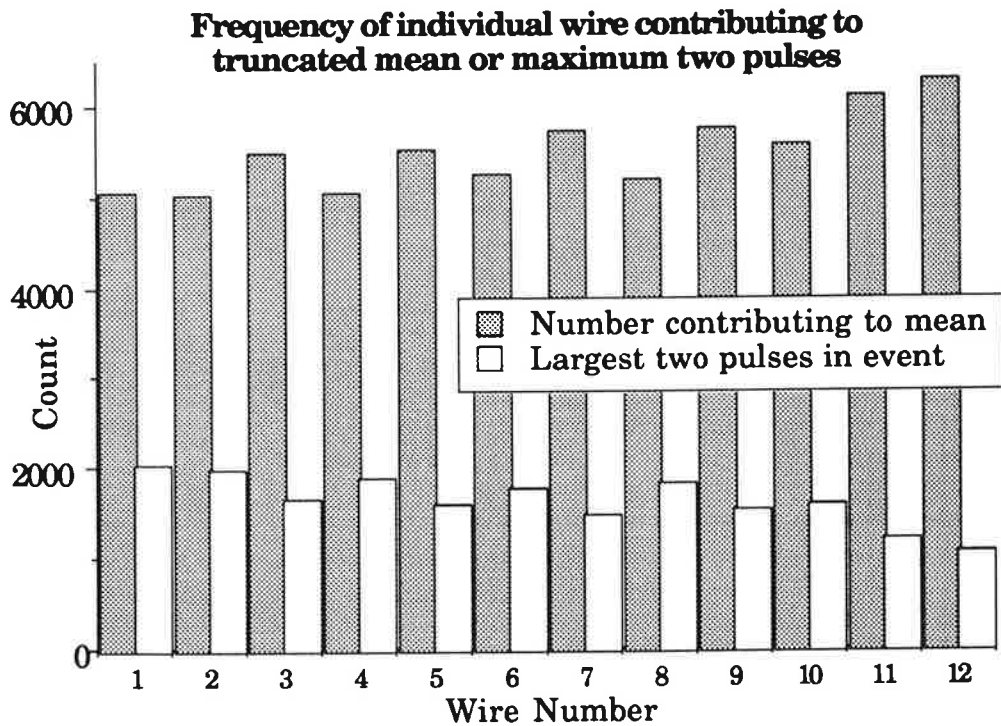


Figure 8.2.9 Distribution of wires contributing to truncated mean.

The relatively large degree of truncation involved in excluding the largest 5 pulses in each event reduces the sensitivity to TR photons. The success of this is evident in figure 8.2.6 above, where there is minimal difference between the data with and without the radiator present, and also in figure 8.2.10, which shows the observed pulse spectra for the 5<sup>th</sup> and 6<sup>th</sup> largest pulses in an event for data with and without a carbon fibre radiator in front.

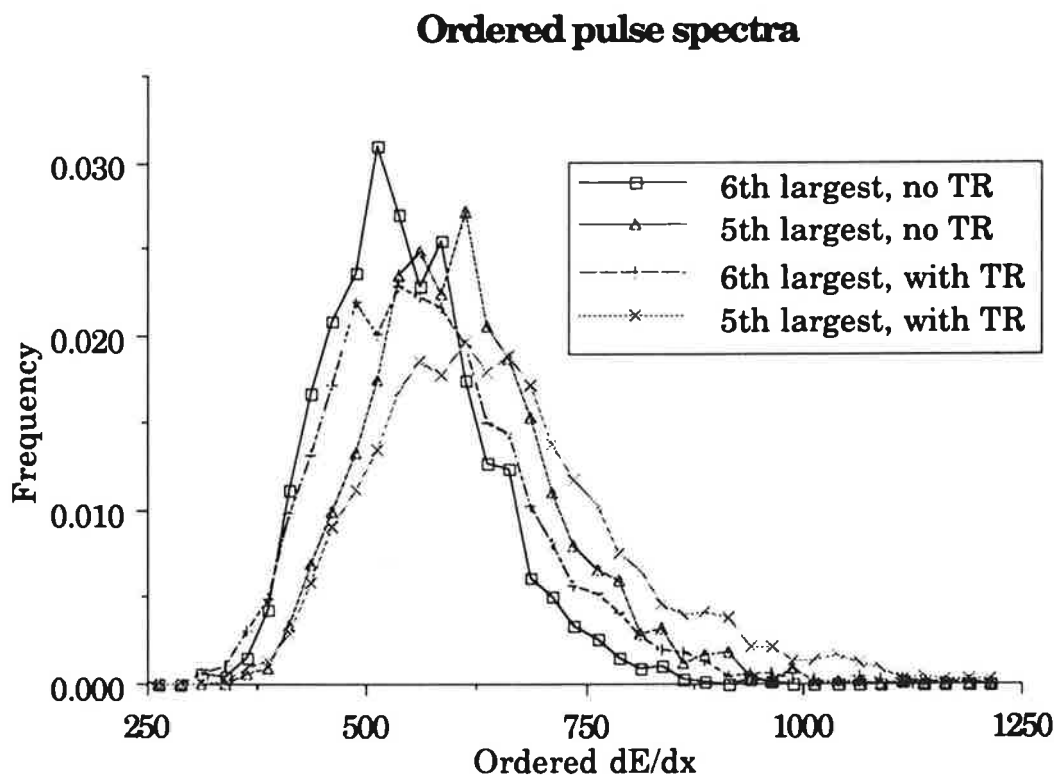


Figure 8.2.10 Observed pulse spectra for the 5<sup>th</sup> and 6<sup>th</sup> largest pulses in an event for data with and without a carbon fibre radiator in front.

## 8.2.6 Results

As data were only taken in an electron beam, there is no possibility of calculating the particle identification resolution. Moreover all the data is on the Fermi plateau, as the electrons are all extreme relativistic with

a lowest energy of  $E_{\text{beam}} = 1.2$  GeV. Therefore the effect of the amount of truncation on the dependence on  $\beta\gamma$  of the truncated mean cannot be investigated.

Table 8.2.1 contains the results of a Gaussian fit to the overall truncated mean distribution and to the distribution for the individual wires contributing to the truncated mean. The results for a track through the complete forward tracker have been simulated by combining the calibrated energies from 3 separate events within the same run, excluding the largest 10 pulses. The standard deviation of the fit is quoted as a fraction of the mean in order to remove the effect of the increased pulse height possible with the DL3000. In any case the integrals are normalised to 400 counts for the DL300 data and to 900 counts for the DL3000 data. The results are for the xenon based gas used in the TR analysis below, for the set of 25 argon runs described above and for the argon data referenced in chapters 6 and 7.

Gas mixture used	FADC used	TR	Standard deviation	Single event	3 events
Xe/He/C <sub>2</sub> H <sub>6</sub> 30/30/40	DL300	No	0.30	0.14	0.08
Xe/He/C <sub>2</sub> H <sub>6</sub> 30/30/40	DL300	C	0.34	0.16	0.10
Xe/He/C <sub>2</sub> H <sub>6</sub> 30/30/40	DL300	Poly	0.32	0.17	0.10
Ar/C <sub>2</sub> H <sub>6</sub> 50/50	DL300	No	0.26	0.14	0.08
Ar/C <sub>2</sub> H <sub>6</sub> 50/50	DL3000	No	0.26	0.15	0.10
Ar/C <sub>2</sub> H <sub>6</sub> 50/50	DL3000	No	0.25	0.14	0.10
Ar/C <sub>2</sub> H <sub>6</sub> 50/50	DL3000	No	0.28	0.18	0.11

Table 8.2.1 Truncated mean distributions for various data.

For the xenon data there is minimal increase in the width of the distribution when the transition radiator is inserted in front of the chamber. For the DL3000 data the front wire of the chamber was effectively dead, resulting in the average number of wires contributing to the truncated mean being 6 instead of 7, leading to an expected broadening of the distribution by a factor  $\sqrt{\frac{7}{6}}$ . In table 8.2.2 is the variation in mean  $\frac{dE}{dx}$  for Ar/C<sub>2</sub>H<sub>6</sub> 50/50, calculated using the GEANT 3.13 package<sup>7</sup>. Comparing this variation with the simulated resolution for tracks passing through all three radial chambers shows that separation between  $e$  and  $\pi$  should just be possible. However the rise in the measured truncated mean will be less than in the mean  $\frac{dE}{dx}$  quoted here and a full 36 measurements will only be possible in the angular range  $7^\circ \leq \theta < 17^\circ$ .

Particle energy / GeV	$e^- \frac{dE}{dx} / \text{keV cm}^{-1}$	$\pi^- \frac{dE}{dx} / \text{keV cm}^{-1}$
1	9.67	6.0
5	10.03	5.78
10	10.23	6.26
20	10.46	6.84
30	10.60	7.20
40	10.69	7.46
50	10.76	7.66
60	10.80	7.82

Table 8.2.2 Calculated variation in mean  $\frac{dE}{dx}$  for Ar/C<sub>2</sub>H<sub>6</sub> 50/50.



## 8.3 TR Measurements

### 8.3.1 Introduction

As is evidenced above, the 36 wires in the radial chambers are only just sufficient to distinguish between electrons and pions. The major discriminant will be the transition radiation produced by electrons for those particles whose momentum is below the threshold for the pions to radiate. With the radiators used this threshold is in the region of 100 GeV.

After a brief introduction to transition radiation production and absorption, the TR detection techniques which have been studied will be described. Although the  $\frac{dE}{dx}$  measurements above will probably not be useful in their own right as a method of particle discrimination, it will be seen that they play a pivotal role in the TR detection.

Data were taken during the 1987 test beam work with both a carbon fibre transition radiator and a polypropylene fibre radiator. In the H1 detector the radiator used will consist of polypropylene foils; these will give a slightly higher yield of TR photons than either of the radiators tested. The distributions obtained with both the above radiators are very similar, so only the polypropylene results will be described. The radiator used for these tests consists of a 10 cm long tube filled with brushed 20  $\mu\text{m}$   $\emptyset$  polypropylene fibres. The density of the fibres is 0.92 g cm<sup>-1</sup>, with the packing density being 0.067 g cm<sup>-1</sup>.

### 8.3.2 Overview Of Transition Radiation Production

Electromagnetic radiation is produced when a moving charged particle traverses the interface between two media which have different dielec-

tric properties. In each medium the particle is 'dressed' in an electromagnetic field, which depends on the particle velocity, and on the dielectric constant of the medium. At the interface this field changes, due to the change in the dielectric constant, and a portion of this field is radiated off. This radiation is necessary in order to ensure that the tangential component of the  $\mathbf{E}$  field and the normal component of the  $\mathbf{D}$  field are continuous across the interface. It is known as transition radiation, and was first predicted by Ginzburg and Frank<sup>8</sup>. It may be divided into two classes: optical TR, emitted in the backward direction, and X-ray TR, emitted in the forward direction. The latter is that which is used for particle identification.

This forward X-ray radiation produced by an ultra-relativistic particle was first predicted by Garibian<sup>9</sup>. The intensity is very strongly dependent on the Lorentz factor  $\gamma$ , and it is closely confined to the particle trajectory. It arises from the above boundary conditions on the transverse components of the EM field. The field due to the relativistic particle strongly resembles forward-moving EM radiation, and some of this is shaken off at the interface.

Assuming the following approximations<sup>2</sup>:

- $\gamma \gg 1$ : only consider extreme relativistic particles (a 5 GeV electron has a value of  $\gamma$  of 10000)
- $\omega \gg \omega_p$ , where  $\omega$  is the angular frequency of the TR photon ( $E = \hbar\omega$ ) and  $\omega_p$  is the plasma frequency of the radiator (for low Z solids  $\hbar\omega_p \approx 30$  eV): only consider the X-ray region, so the dielectric constant may additionally be given by:

$$\varepsilon(\omega) = 1 - \frac{\omega_p^2}{\omega^2} \quad [8.3.1]$$

then, for a singly-charged particle passing through one vacuum-dielectric interface:

- the total energy,  $S$ , in the spectrum, is proportional to the Lorentz factor of the particle:

$$S = \gamma \frac{\alpha}{3} \hbar \omega_p \quad [8.3.2]$$

- the bulk of the transition radiation lies in the soft X-ray region:

$$dn = \alpha \frac{2}{\pi \hbar \omega} \ln\left(\frac{\gamma \omega_p}{\omega}\right) d\hbar \omega \quad [8.3.3]$$

- the angular distribution is extremely forward peaked:

$$\langle \theta \rangle \approx \sqrt{\left(\frac{1}{\gamma^2} + \frac{\omega_p^2}{\omega^2}\right)} \quad [8.3.4]$$

If the particle passes through a single vanishingly thin foil then obviously no TR would be produced; it would be suppressed by destructive interference from the front and back surfaces of the foil. The minimum distance that the particle must travel in the medium for the Fourier component of its electric field with angular frequency  $\omega$ ,  $E(\omega)$ , to estab-

lish characteristics consistent with the dielectric properties of the medium is known as the formation zone,  $Z_f$ . With the above approximations this is given by:

$$t \geq Z_f \approx \frac{2c}{\omega} \left( \frac{1}{\gamma^2} + \theta^2 + \frac{\omega_p^2}{\omega^2} \right)^{-1} \quad [8.3.5]$$

On taking the coherence between the two interfaces into account, equation [8.2.3] becomes:

$$\begin{aligned} dn = \alpha \frac{2}{\pi \hbar \omega} \int \left[ \left( \frac{1}{\gamma^2} + \theta^2 \right)^{-1} - \left( \frac{1}{\gamma^2} + \theta^2 + \frac{\omega_p^2}{\omega^2} \right)^{-1} \right]^2 \theta^3 \\ \times 4 \sin^2 \left( \frac{t\omega}{4\beta c} \left( \frac{1}{\gamma^2} + \theta^2 + \frac{\omega_p^2}{\omega^2} \right) \right) d\theta d\hbar \omega \quad [8.3.6] \end{aligned}$$

where  $t$  is the thickness of the foil. The argument of the  $\sin^2$  term represents the relative phases of photons emitted at the two interfaces, with a phase shift of  $\pi$  to ensure destructive interference as the thickness of the foil tends to zero. Coherence effects between many foils may be described by the inclusion of the  $N$  slit diffraction grating coefficient into the above equation.

### 8.3.3 Overview Of Transition Radiation Absorption

The mechanism by which soft X-rays are predominantly absorbed in gaseous detectors is photo-electric absorption; this results in the emission of a high energy photo-electron, leaving the “struck” ionised atom in an excited state. The highest absorption occurs in the region of the atomic electron shell edges (figure 8.3.1).

There are two main methods for this atom to de-excite; by emission of a second, Auger, electron, which is the dominant process in argon, or by fluorescence, in which the ionised atom de-excites by emission of a sec-

ondary photon produced by the internal electron rearrangement. This photon will be characteristic of the detector gas, having an energy just below that corresponding to the atomic shell which had contained the original photo-electron. As it has an energy just below the shell edge it has a relatively long 'mean free path' in the gas, and often travels some distance before absorption. In argon in particular the likelihood of escape is high, leading to the characteristic 'escape peak' in X-spectra measured in an argon based detector.

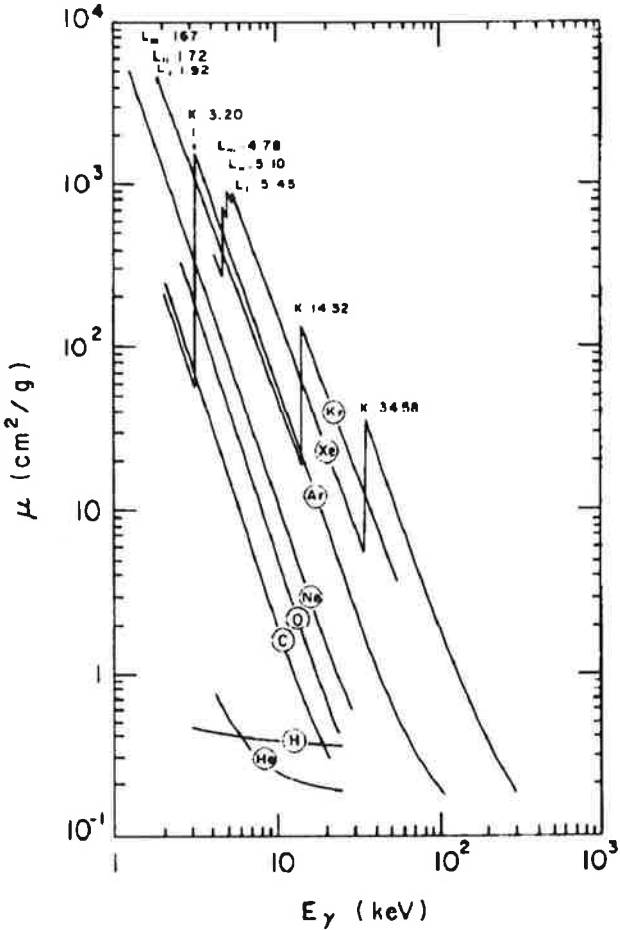


Figure 8.3.1 X-ray absorption coefficients versus photon energy for several gases<sup>10</sup>.

### 8.3.4 Total Charge Method

The mean of the calibrated pulses for the front six wires of the chamber might be expected to be a good  $e/\pi$  discriminant. The rationale behind this is that the front six wires of the chamber, amounting to a depth of 6 cm of dilute xenon based gas, corresponds to the “rule of thumb” thickness of 1.6 to 2 cm of xenon favoured for conventional TR detectors<sup>11</sup>. This is an implementation of the total charge or “Q” method of TR detection<sup>12</sup>. The effect of averaging over more than 1 wire is however to dilute the TR signal accordingly, as it is in general only present on 1 wire.

By comparing such mean pulse height distributions for data with and without a radiator, acceptance / contamination values for radiating and non-radiating ultra-relativistic particles can be determined by making various threshold cuts in this distribution. Unfortunately the lack of any real pion data for comparison renders the task of producing an accurate electron pion discrimination extremely difficult. Furthermore the data without radiator includes the TR contribution from the 5 mm rohacell supports for the front field formers, as already mentioned in chapter 2, although this only amounts to an average of  $\frac{1}{20}$  of a TR photon per event. Notwithstanding this the results for three cells can be simulated by histogramming the mean of the pulse integrals for the front 6 wires of three consecutive events, and applying a threshold cut to evaluate the radiating / non-radiating response. Figure 8.3.2 shows the measured electron spectra, and figure 8.3.3 the resultant radiator / no-radiator acceptance / contamination.

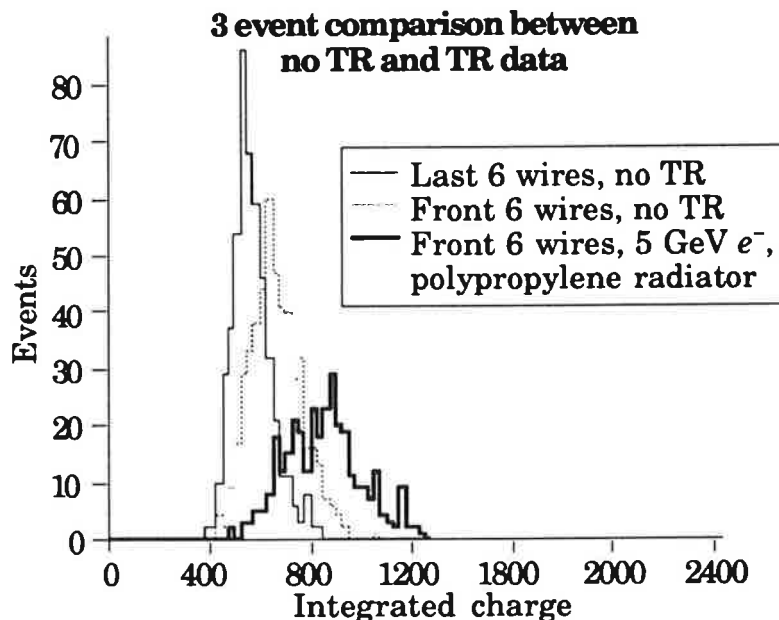


Figure 8.3.2 Observed mean pulse height spectra for the front 6 wires of 3 consecutive events for data with and without a polypropylene radiator in front of the chamber. The mean pulse height spectrum for the back 6 wires without radiator is also shown.

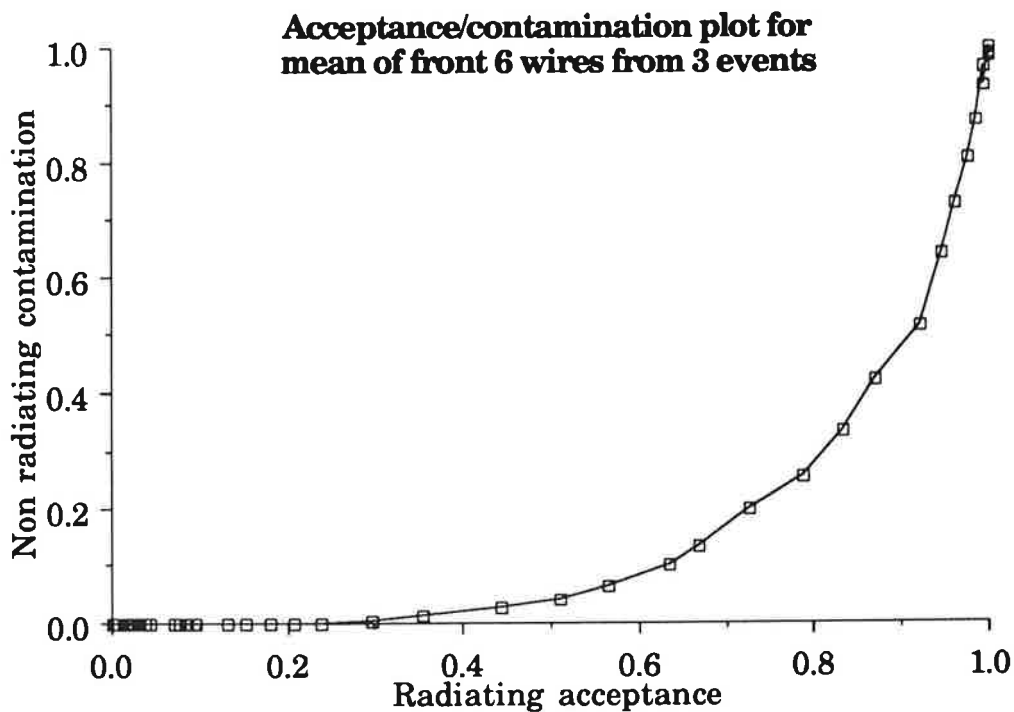


Figure 8.3.3 The resultant radiating/non-radiating particle acceptance / contamination.

Also shown in figure 8.3.2 is the distribution for the mean of the rear-most 6 wires in the chamber, again averaged over 3 events. Although the normalisation of the truncated distributions for each wire appears satisfactory, the width of the individual total distributions is seen to vary. This is illustrated in figure 8.3.4 for the worst case of wires 2 and 12; the relative normalisation by means of a single scale factor may not be sufficient and a two parameter normalisation of a scale factor and an offset may be necessary.

The origin of this difference in integrated charge distribution is not clear, although wire 2 has the lowest gas gain and wire 12 the highest; it may arise from saturation of the electronics or the onset of limited proportional gas gain in the chamber, or alternatively it may be caused by the TR from the 5 mm rohacell supports for the front field formers.

The lack of evidence for the effect in later DL3000 data suggests that it may be an artifact of the limited dynamic range with the DL300 FADCs. The TR from the rohacell would not be expected to have such a significant effect because the thickness of the rohacell is  $\frac{1}{20}$  of that of the radiators used and as these produce on average just over 1 TR photon per event this only amounts to residual TR contamination of only  $\frac{1}{20}$  of a TR photon per event. The result in any case is the appreciable difference between the distributions for the mean of the front 6 wires and the mean of the back 6 wires.



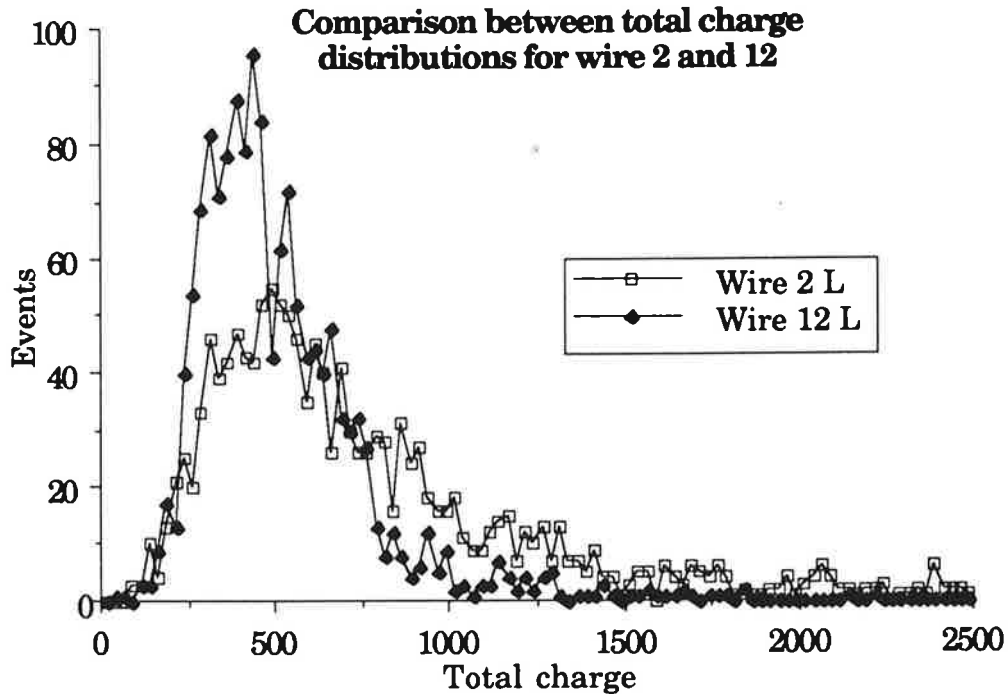


Figure 8.3.4 Total  $\frac{dE}{dx}$  distributions for wires 2 and 12, no radiator, after calibration.

The first attempt at analysis of these data to produce an  $e/\pi$  discrimination<sup>13</sup> (hereafter referred to as STS) compares the front 6 wires with the radiator to the back 6 wires without the radiator in order to circumvent the broader distributions on the front wires. The pion response at different energies is simulated by scaling the electron response, a technique exploited in earlier TR detector tests<sup>14</sup>. However not only are there no  $\frac{dE}{dx}$  measurements for the gas mixture on which to base the scaling parameters but this scaling also has the side-effect of similarly reducing the  $\delta$ -ray production. As evidenced by equation 8.2.2, this is not the case in the real data. As this is the dominant source of residual  $\pi$  contamination, the results quoted from this analysis have to be treated with considerable caution. The pion scaling factors which are used are in fact derived from data for the gas mixture Xe/CH<sub>4</sub>/C<sub>3</sub>H<sub>8</sub> 87.5/7.5/5.0 at atmospheric pressure<sup>15</sup> rather than the gas mixture used, namely Xe/He/C<sub>2</sub>H<sub>6</sub> 30/30/40. Repeating this analysis determining the total

charge according to the procedure of chapter 7 and incorporating the same pion scaling factors gives the results listed in table 8.3.1, along with the previous results. The STS analysis treats the read-out from each end of the wire separately, hence the 2 columns. The threshold error quoted is the change in the pion contamination on varying the threshold bin in the histogram by 1 bin, where the bin width corresponds to 6% of the truncated mean charge.

“Pion energy” / GeV	Scale factor	Pion contamination	Pion threshold error	STS left-hand read-out	STS right-hand read-out
5	0.74	0%	0%	0.5%	0.6%
10	0.82	0.8%	0.8%	1.8%	2.6%
20	0.86	1.5%	1%	2.4%	5.0%
40	0.91	4%	1.5%	4.8%	10.5%
60	0.95	7%	3.5%	9.2%	16.0%

**Table 8.3.1** Results for 90% electron acceptance from comparing mean of front 6 wires over 3 events with radiator to back 6 wires without radiator.

The results for a “pion energy” of 5 GeV in particular show the shortcomings of scaling the electron distribution; for electron acceptances of 95% or less such a procedure gives no pion contamination at all. Repeating the analysis but comparing the front 6 wires with radiator to the front 6 wires without radiator leads to the results in table 8.3.2.

“Pion energy” / GeV	Scale factor	Pion contamination	Pion threshold error
5	0.74	2%	2%
10	0.82	9%	3.5%
20	0.86	15%	7%
40	0.91	26%	8%
60	0.95	36%	10%

Table 8.3.2 Results for 90% electron acceptance from comparing mean of front 6 wires over 3 events with radiator to front 6 wires without radiator.

As these results are derived by comparing the same class of data for electrons and “pions”, this table probably forms a somewhat more reliable estimate of the particle resolution obtainable with this method.

### 8.3.6 Ordered $\frac{dE}{dx}$ Distributions

The TR analysis technique outlined above effectively concentrates on using the relativistic rise in  $\frac{dE}{dx}$  energy deposition as the discriminant and only exploits the TR photon information as an enhancement of this effect. The outcome of this is the markedly different momentum dependence at momenta below 40 GeV between the above results and those from conventional TR detectors. This difference may also be correlated with scaling the measured electron spectrum to produce the pion spectrum.

In order to investigate alternative X-ray detection algorithms a simple Monte Carlo has been written. This uses the  $\frac{dE}{dx}$  simulation routines extracted from GEANT 3.13<sup>16</sup> and the TR photon simulation routines extracted from the H1 detector simulation implemented using GEANT

3.11<sup>17</sup>.  $\delta$ -rays are not explicitly treated, other than by the improvements for gaseous detectors introduced in GEANT 3.12 and updated in GEANT 3.13. From this simulation of the  $\frac{dE}{dx}$  and TR absorption in the chamber it is apparent that the size of the measured energy deposition is in general a better indicator than location for the TR photon; pulses including a TR photon are more likely to be the largest pulse than to be a pulse on one of the front wires in the chamber. This is particularly true with argon, where the photon range is large.

In order to exploit this information the calibrated pulse heights are histogrammed versus the pulse height order for each event. This permits the construction of sets of pulse height distributions for each ordered pulse, irrespective of the pulse's location in the chamber. Although the Monte Carlo predicts little more than one photon per track, these pulse height distributions reveal that there is almost as much information contained in the second largest pulse in an event as in the largest. This is particularly true for simulated 3 event data; the exclusion of the largest pulses is very effective at suppressing the  $\delta$ -ray background. This is a refinement for multiple sampled data of the truncated mean "Q" method of TR detection<sup>14</sup>, allowing suppression of the  $\delta$ -ray background even for a single detector. Alternatively these distributions may form the basis for a maximum likelihood analysis, again possibly ignoring the largest pulses and also incorporating weighting by wire number to exploit the observed mean TR photon range in the chamber. Such an analysis has not yet been attempted on this data.

The results of applying a simple threshold cut in the distributions of the largest pulse, the second largest and the third largest pulse are shown in figure 8.3.5. The concentration of the  $\delta$ -ray contamination in the dis-

tribution for the largest pulse is particularly apparent. The results from the second largest pulse alone are seen to be better than the results from the mean of the front 6 wires in each chamber.

The lack of any pion data for comparison renders the task of producing an electron pion discrimination extremely difficult. The radiating non-radiating electron discrimination almost certainly overestimates the contamination by overestimating the residual  $\frac{dE}{dx}$  distribution, whereas scaling the “pion” response underestimates the contamination by underestimating the  $\delta$ -ray distribution. Nevertheless the results of scaling the non-radiating distributions are listed in table 8.3.3 for completeness.

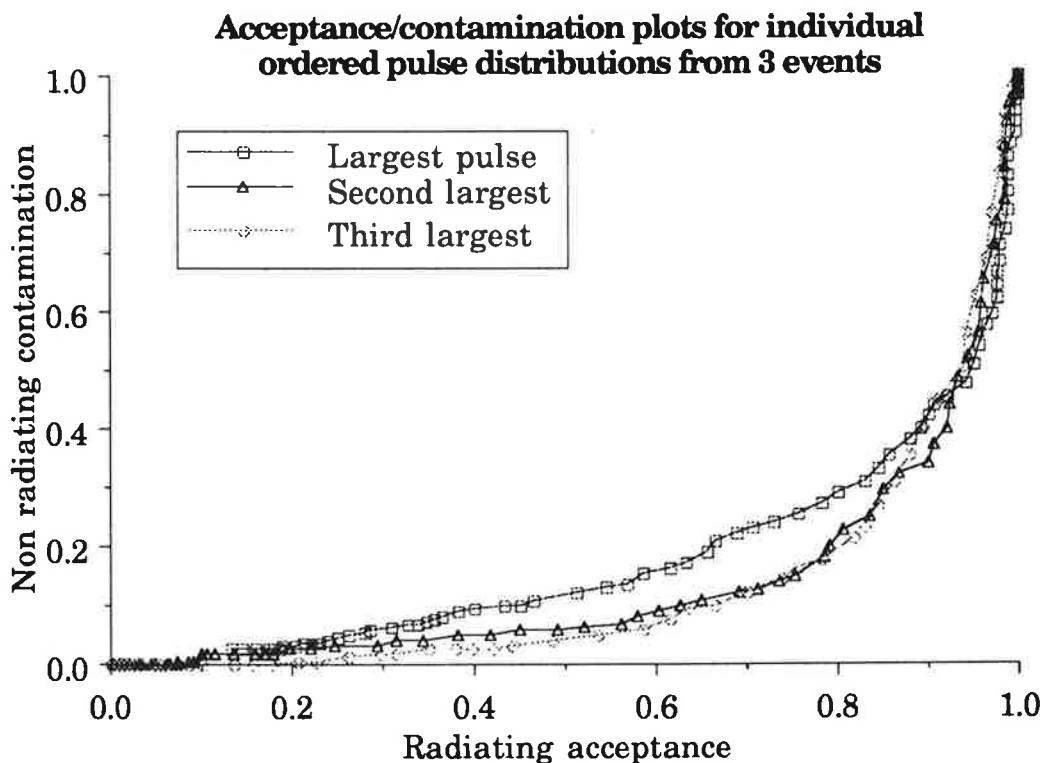


Figure 8.3.5 Radiating/non-radiating particle discrimination by threshold cut in observed pulse height spectra.

“Pion energy” / GeV	Scale factor	Pion contamination	Pion threshold error
5	0.74	7.6%	1.3%
10	0.82	12.7%	1.4%
20	0.86	16.6%	2%
40	0.91	22.5%	3%
60	0.95	29%	3.5%

Table 8.3.3 Results for 90% electron acceptance from comparing the second largest pulse over 3 events with radiator to the same without radiator.

## 8.4 Conclusions

The detection of the transition radiation signal in a multiple sampling tracking detector provides a slightly different TR signal from previous dedicated TR detectors. In order to optimally exploit this signal it is necessary to merge the existing algorithms for TR detection and  $\frac{dE}{dx}$  measurements to address the new data. The multiple sampling provides the opportunity to suppress further the  $\delta$ -ray contamination not already excluded by the track resolution, over and above that possible with previous TRDs. The same analysis techniques may be employed to extract the best particle discrimination from both the  $\frac{dE}{dx}$  measurements and the TR detection, simply by addressing different subsets of the ordered data. Indeed the major source of contamination in the particle identification which is feasible with both subsets of data is the effects of the  $\delta$ -rays in the tail of the Landau  $\frac{dE}{dx}$  distribution.

The actual particle discrimination possible is very difficult to quantify in the absence of data for anything other than electrons. Notwithstanding this, the  $e/\pi$  discrimination is likely to give 90% electron acceptance with

in the region of 10% pion contamination over the momentum range necessary in H1. Improvements in the H1 radial chambers over the prototype cell used for these tests include greater dynamic range FADCs, a substantially thinner front window of only 75  $\mu\text{m}$  total thickness excluding the rohacell foam compared to the 175  $\mu\text{m}$  thick window on the prototype and polypropylene foil radiators rather than the polypropylene fibres used above, all of which will improve the X-ray detection efficiency.

- 
- 1** L Landau, J. Phys. USSR 8 (1944) 201
  - 2** J H Cobb, A Study of some electromagnetic interactions of high velocity particles with matter, D Phil thesis, University of Oxford (1975)
  - 3** U Fano, Ann. Rev. Nucl. Sci. 13 (1963) 1
  - 4** A Crispin & G N Fowler, Rev. Mod. Phys. 42 (1970) 290
  - 5** taken from W W M Allison and J H Cobb, Ann. Rev. Nucl. Part. Sci. 30 (1980) 253
  - 6** see for example S P Beingessner, R K Carnegie and C K Hargrove, NIM A260 (1987) 210
  - 7** R Brun, F Bruyant, M Maire, A C McPherson and P Zancarini, GEANT3 user guide CERN DD/EE/84-1, 1987
  - 8** I M Ginzburg and L M Frank, Sov. Phys. JETP 16 (1946) 15
  - 9** G M Garibian, Sov. Phys. JETP 6 (1958) 1079
  - 10** taken from F Sauli, Principles of operation of multiwire proportional and drift chambers, CERN 77-09 (1977)

- 
- 11 see for example R D Appuhn *et al*, NIM A263 (1988) 309 or Y Watase *et al*, NIM A248 (1986) 379
- 12 see for example B Dolgoshein, NIM A252 (1986) 137
- 13 S T Schulte, Elektronidentifikation mittels Übergangsstrahlung in einem Testsegment der radialen H1-Driftkammer, Diplomarbeit, RWTH Aachen, PITHA 89/04 (1989), and H Grässler *et al*, NIM A283 (1989) 626
- 14 see for example R D Appuhn *et al*, NIM A263 (1988) 309
- 15 A H Walenta *et al*, NIM A161 (1979) 45
- 16 R Brun, F Bruyant, M Maire, A C McPherson and P Zanarini, GEANT3 user guide CERN DD/EE/84-1, 1987
- 17 Uli Braun, private communication



# Chapter 9: Summary

## 9.1 Introduction

The previous four chapters have outlined the procedures adopted in the analysis of the FADC data, but have not presented the results obtained with all the test beam data that were taken. As the details of the results are dependent on the pulse shape observed and as this is influenced by specific parameters of the chamber under investigation such as the total resistance of the sense wires, there is little point in so doing. Nevertheless there are a few general questions concerning the eventual performance of the H1 radial chambers which can be answered on the basis of data from the prototypes.

By combining data from both test beam periods the drift precision over the entire active volume of the wedge may be investigated; 8 bit FADC data is available for the outer third of the wedge out to the maximum radius and 6 bit data is available for the remainder of the chamber, including down to the innermost radius. These are presented in section 9.2.

The coordinate measurement along the wire cannot be investigated further than as summarised in figure 7.5.1, subject to the discussion in section 7.7. The same considerations preclude investigation of the  $\frac{dE}{dx}$  measurements and TR detection over the entire active volume of the chamber. However there is little reason to expect the performance to be degraded compared to the results already presented.

Hints are possible concerning the performance of the detector in the H1 solenoidal magnetic field, but these show little more than the effect of the large Lorentz angle when using Ar/C<sub>2</sub>H<sub>6</sub> 50/50 at atmospheric pressure and a drift field of 1.2 kV cm<sup>-1</sup>. Nonetheless the results obtained are discussed in section 9.3.

The major open question is the performance of the chamber when using the preferred xenon based gas mixtures. Again data is available from the 1987 prototype with some xenon based gases, but no attempt was made at the time to optimise the drift precision. The results obtained and the directions for further investigation are outlined in section 9.4.

## **9.2 Drift Precision Over The Entire Active Volume**

The results for the drift precision described in chapter 6 are for data taken 3 cm from the outer radius of the detector; what effect the electrode structure of the outer radius wall or of the cathode planes has on the precision is not mentioned. In figure 9.2.1 is the point precision as a function of drift distance calculated in the same manner as for figure 6.3.2, using the first electron timing algorithm, for all the radial positions at which data were taken using the third prototype. Comparison between the different radial positions shows that the drift precision is maintained out to the maximum possible drift distance, even for tracks immediately adjacent to the outer radius field shaping electrodes.

The most significant effect is the degradation by ~50 μm (0.1 FADC bins) in the last 5 mm (10 FADC bins) drift distance before reaching the cathode plane. This is without doubt associated with the non-linearities in

the drift field discussed in section 3.3 introduced by the 6 mm strip, 1 mm gap structure of the cathode planes. That the outer electrode structure has minimal effect is also supported by the good agreement between the RMS residuals for each wire; for the data 3 cm from the wide end the RMS residuals for each wire have an overall mean value of 0.25 FADC bins and a standard deviation of 0.02 FADC bins. The RMS residual for the rearmost wire next to the field formers on the inner back surface of the chamber is 0.26 FADC bins.

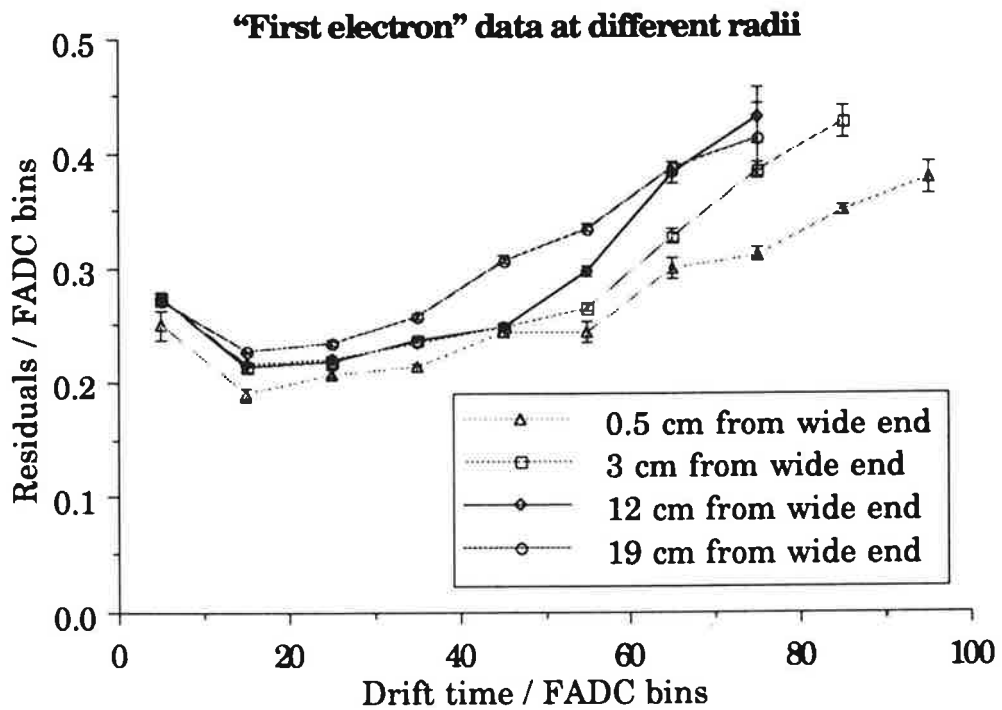


Figure 9.2.1 Point precision versus drift time using first electron method for all the radial positions at which data were taken with the third prototype.

Similar results from the 1987 test beam are shown in figure 9.2.2, where data near the inner radius of the chamber are plotted, where the drift cell dimensions are smallest. In making direct comparison between figures 9.2.1 and 9.2.2 it should be borne in mind that the data in figure 9.2.2 were taken using 6 bit FADCs, resulting in worse overall preci-

sion, as is shown in figure 6.9.1. Moreover the 6 mm/4 mm strip/gap ratio of the cathode planes results in a significantly greater distortion of the electric field in the neighbourhood of the cathode planes.

These results show that chamber performs satisfactorily over the entire active volume, with only minor degradation of the timing precision in the immediate vicinity of the cathode planes and the wire plane.

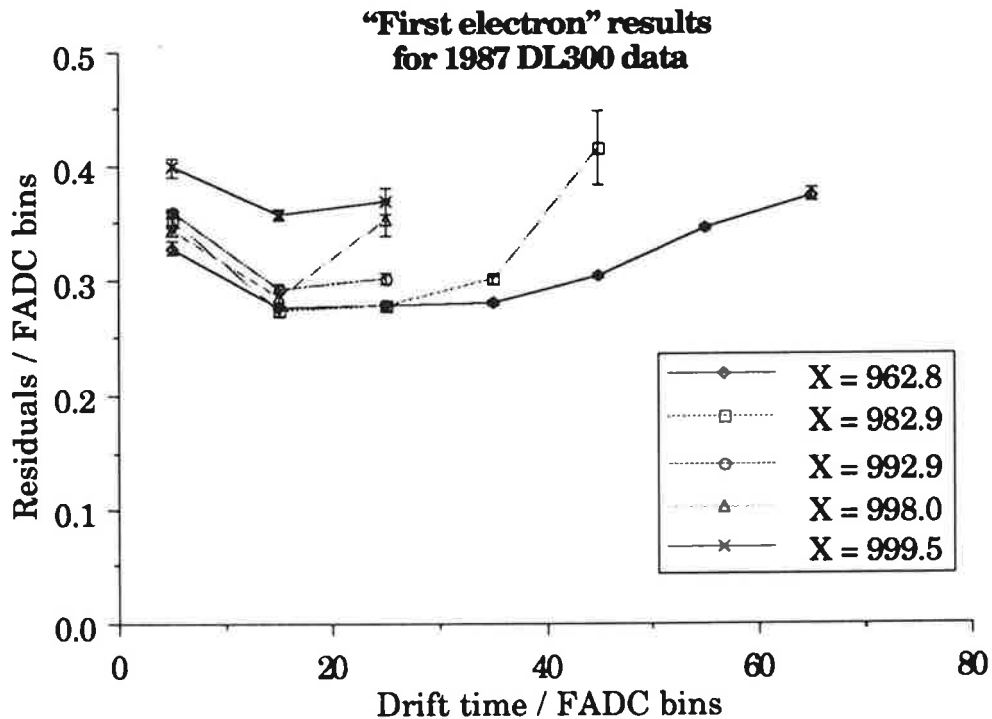


Figure 9.2.2 Point precision versus drift time using first electron method for various radial positions at which data were taken with the second prototype. The inner radius corresponds to  $X = 1000.0$  cm.

### 9.3 Drift Precision Of The Chamber In A Magnetic Field

During the 1988 test beam period data were taken with an axial magnetic field. Unfortunately operational difficulties with poor quality com-

ponents and the gas system led to data only being taken using Ar/C<sub>2</sub>H<sub>6</sub> 50/50 at a drift field of 1.2 kV cm<sup>-1</sup>, with the highest magnetic field data being taken immediately prior to the failure of the chamber. The results from these measurements are shown in figure 9.3.1. There is a slight degradation in the timing precision in the field of B = 0.4 T. The results at B = 0.87 T however show a marked deterioration.

The mean fitted drift velocity as calculated in section 6.8 is illustrated in figure 9.3.2. This corresponds to the component of the drift velocity perpendicular to the wire plane. Comparing the fitted velocity with magnetic field to that without magnetic field enables an estimate of the Lorentz angle to be made. This gives a Lorentz angle of 16° at B = 0.4 T and 42° at B = 0.87 T, in good agreement with the previously measured Lorentz angles of 15 - 20° at B = 0.5 T and about 40° at B = 1.0 T<sup>1</sup>.

One of the reasons for choosing a xenon based gas mixture is the reduced Lorentz angle. However as there are no extant measurements with the preferred mixture of Xe/He/C<sub>2</sub>H<sub>6</sub> 30/30/40 it remains to be seen how this gas behaves in the magnetic field. Computer simulations employing a full multi-term treatment of the Boltzman transport equations<sup>2</sup> predict that the Lorentz angle for Xe/He/C<sub>2</sub>H<sub>6</sub> 30/30/40 at a drift field of 1.4 kV cm<sup>-1</sup> in the full H1 solenoidal field of B = 1.2 T will be 23.5°, compared with between 40° and 50° for Ar/C<sub>2</sub>H<sub>6</sub> 50/50 at a drift field of 1.2 kV cm<sup>-1</sup>.

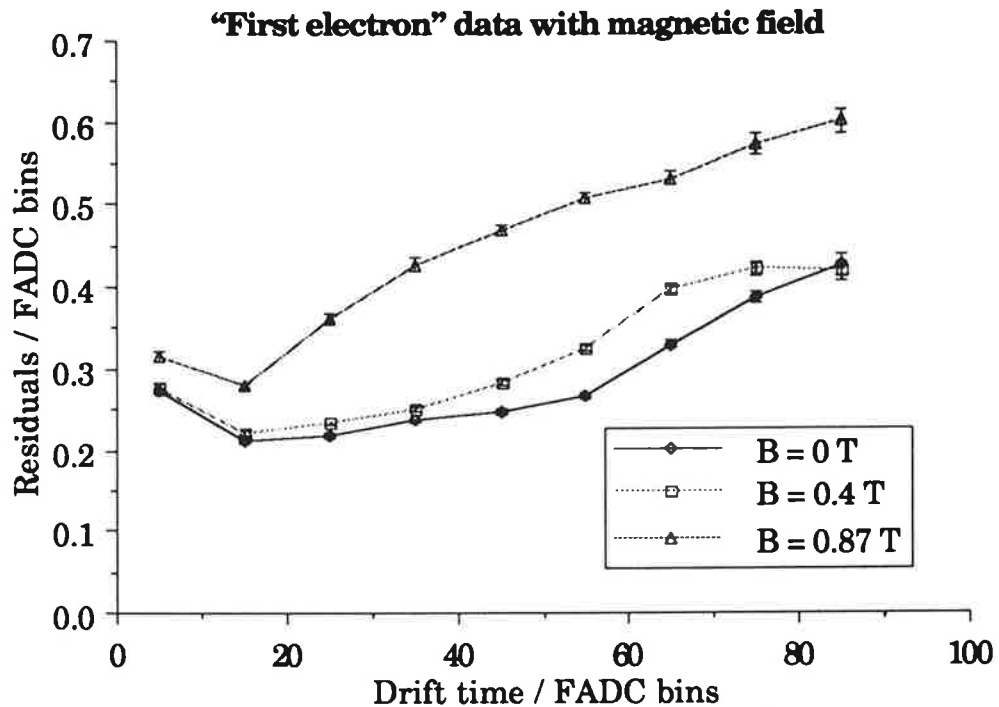


Figure 9.3.1 Point precision versus drift time using first electron method for data taken with the third prototype and various values of the magnetic field.

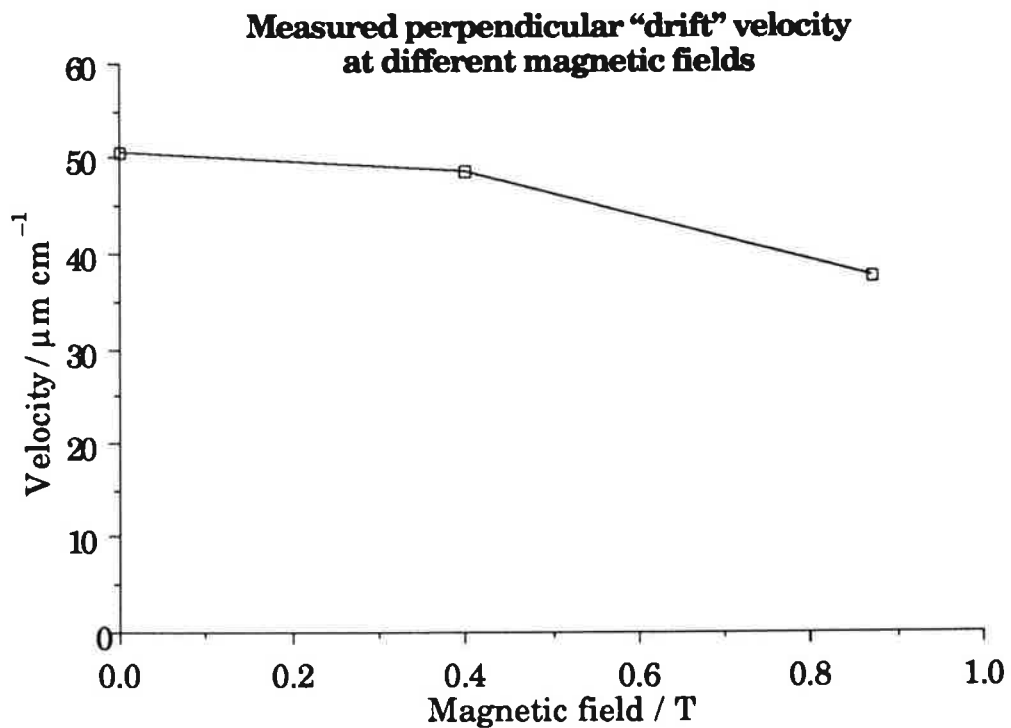


Figure 9.3.2 Perpendicular drift velocity versus magnetic field for data taken with the third prototype.

## 9.4 Drift Precision With A Xenon Based Gas

Unfortunately no measurements with 8 bit FADCs were possible with any of the xenon based gas mixtures considered. However data were taken with the second prototype using 6 bit FADCs. The performance with 8 bit FADCs may be expected to be an improvement over these results, as is the case with Ar/C<sub>2</sub>H<sub>6</sub> 50/50. In any case the point precision with the xenon based gas mixtures used benefits from the reduced electron drift velocity; the Xe/He/C<sub>2</sub>H<sub>6</sub> mixtures typically had a drift velocity of approximately 30 μm ns<sup>-1</sup>, compared to 54 μm ns<sup>-1</sup> with Ar/C<sub>2</sub>H<sub>6</sub> 50/50. The demands on the timing precision for a particular spatial precision are accordingly reduced. Xe/He/CH<sub>4</sub> mixtures were also investigated, but these have an even slower drift velocity of around 15 μm ns<sup>-1</sup>, which would necessitate more than the available 2.56 μs depth of FADC memory to record the largest drift distances in the radial chamber. The timing residuals obtained for a drift field of 1.0 kV cm<sup>-1</sup> are illustrated in figure 9.4.1 for the Xe/He/C<sub>2</sub>H<sub>6</sub> 30/30/40 mixture used in the TR detection analysis and the Xe/He/C<sub>2</sub>H<sub>6</sub> 20/50/30 mixture referenced in chapter 6. For the latter the mean point precision is 168 μm, with the fit described by equation 6.2.1 giving the constant precision as 117 μm and the diffusion term as 84 μm √cm<sup>-1</sup>, compared to 110 μm and 80 μm √cm<sup>-1</sup> for Ar/C<sub>2</sub>H<sub>6</sub> 50/50 measured with 6 bit FADCs.

The 1987 tests established the feasibility of combining efficient X-ray detection with high precision track detection. Little attempt was made at the time to optimise the gas mixture used or the operating point with that gas, other than diluting the mixture with helium in order to keep the density of the gas close to that of the surrounding atmosphere. That

the density is near atmospheric is particularly important for the full scale chambers where the delicate front window and the chamber height of 1.6 m require that there are minimal hydrostatic pressure differences between the chamber volume and the outside world. It is therefore extremely likely that the gas mixture which is finally used will not be one of the mixes already tested. Indeed it is envisaged that the gas will be bubbled through propan-2-ol in order to reduce wire aging, this alcohol having been found most suitable in previous investigations of wire aging with Stablohm 800 wires<sup>3</sup>.

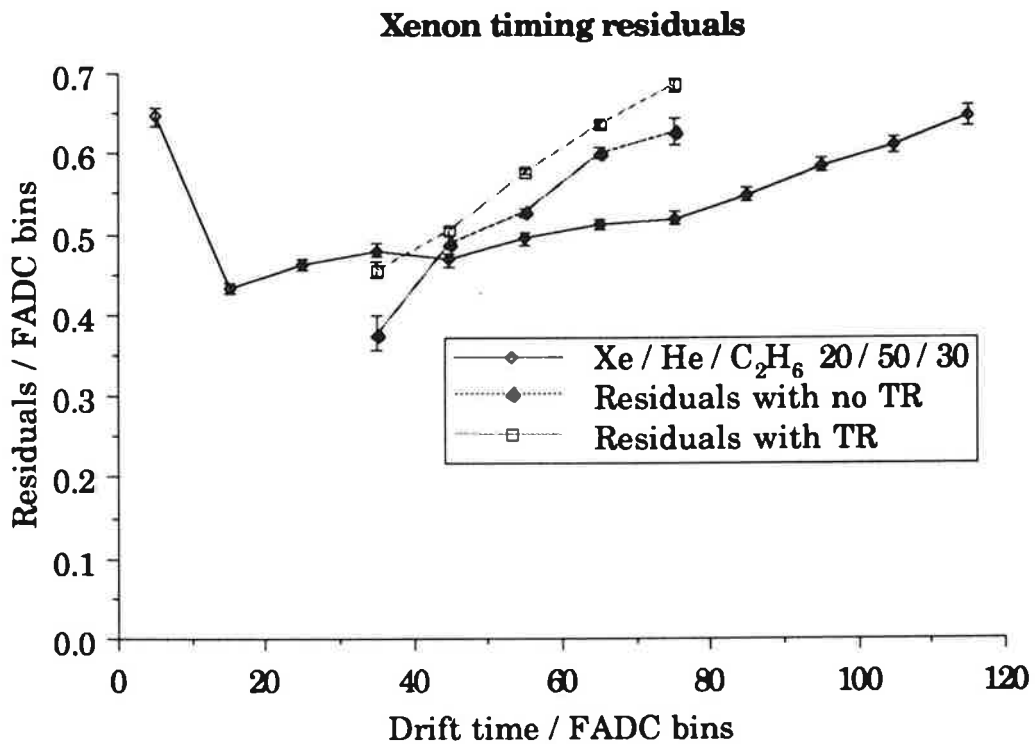


Figure 9.4.1 Point precision versus drift time using first electron method for some of the xenon data taken with the second prototype. The gas used is Xe/He/C<sub>2</sub>H<sub>6</sub> 30/30/40 except where stated.

Moreover for the mixture Xe/He/C<sub>2</sub>H<sub>6</sub> 30/30/40 the computer simulations show that the single electron longitudinal diffusion coefficient improves from  $172 \mu\text{m} \sqrt{\text{cm}^{-1}}$  at  $1.0 \text{ kV cm}^{-1}$  to  $154 \mu\text{m} \sqrt{\text{cm}^{-1}}$  at  $1.4 \text{ kV cm}^{-1}$  in



the full magnetic field (as any timing algorithm used samples more than one of the drifting electrons the variation in point precision with drift distance measured in the chamber is correspondingly reduced compared to the single electron values quoted here<sup>4</sup>). Although the chamber operating point for  $1.4 \text{ kV cm}^{-1}$  investigated with the second prototype indicated in figure 3.2.2 is just outside the allowed region for total ionisation collection, the experience with Ar/C<sub>2</sub>H<sub>6</sub> in the 1988 tests using 8 bit FADCs suggests that in fact the sense wire voltage which would be used will be higher and therefore in the allowed region.

## 9.5 Conclusions And Outlook For H1

Individually all elements of the design of the H1 radial wire chambers have been investigated. These tests have resulted in various design changes in the final detectors, influencing items such as the construction of the transition radiator material and the geometry and electrostatic configuration of the chambers. However the interplay between connected and adjacent cells will have effects which can not be investigated with single cell prototypes. Therefore there will be a continuing programme of tests with the full scale prototype, including tests at CERN which will permit measurements with a pion beam.

New analysis techniques have been evolved in order to best exploit the information made available with 100 MHz FADC digitisation of the drift chamber signals. These result in a point precision of  $\sim 150 \mu\text{m}$  in the drift coordinate when using a gas mixture of Ar/C<sub>2</sub>H<sub>6</sub> 50/50 at a drift field of  $1.2 \text{ kV cm}^{-1}$  at atmospheric pressure over the entire active volume of the chamber. The use of charge division of the measured charge observed at each wire end leads to a point precision of 0.6% of the total

wire resistance in the orthogonal coordinate along the sense wire for isolated tracks. Analysis of data taken with a gas mixture of Xe/He/C<sub>2</sub>H<sub>6</sub> 30/30/40 at a drift field of 1.0 kV cm<sup>-1</sup> at atmospheric pressure indicates that an electron pion discrimination of 90% electron acceptance with less than 10% pion contamination should be possible over the momentum range between 5 GeV and 60 GeV. The use of FADCs furthermore permits a two track resolution of 48 ns (5 FADC bins) to be readily achieved. This corresponds to 1.5 cm when using a xenon based gas.

In summary where suitable measurements have been possible with the prototypes, the resulting evidence suggests that the radial chambers will deliver the required performance as specified in chapters 1 and 2 and in the H1 technical proposal. Whether this actually turns out to be the case, only time will tell.

- 
- <sup>1</sup> A Peisert and F Sauli, Drift and diffusion of electrons in gases: a compilation, CERN 84-08 (1984)
  - <sup>2</sup> S F Biagi, private communications
  - <sup>3</sup> M Atac, Wire chamber aging and wire material, Fermilab FN-435 (1986)
  - <sup>4</sup> F Sauli, Principles of operation of multiwire proportional and drift chambers, CERN 77-09 (1977)